OUT OF EQUILIBRIUM PHENOMENA IN ULTRA-COLD GASES

A Dissertation

Presented to the Faculty of the Graduate School

of Cornell University

in Partial Fulfillment of the Requirements for the Degree of

Doctor of Philosophy

by

Stefan Subhash Natu

January 2013

OUT OF EQUILIBRIUM PHENOMENA IN ULTRA-COLD GASES

Stefan Subhash Natu, Ph.D.

Cornell University 2013

The study of out-of-equilibrium dynamics in ultra-cold gases is a new and exciting field, driven largely by the recent experimental advances in controlling and imaging cold clouds. The experimental and theoretical work thus far has been somewhat exploratory and largely numerical in nature, as the very paradigms for thinking about these systems are not well established. In this thesis I consider several different scenarios of ultra-cold bosonic and fermionic gases driven out of equilibrium and study their properties.

In Chapter 1, I provide an overview of the phenomenology of ultra-cold gases, highlighting the *timescales* governing these systems and how the experimentalist can tune them. I discuss how cold gases can be cooled and trapped and discuss the basic physics behind optical lattices. I also discuss experimental probes of these gases, in particular the new high resolution imaging techniques developed recently at Chicago, Munich and Harvard.

In Chapter 2, I discuss an early experiment (circa. 2008) which observed long lived spin dynamics in a *thermal* spin-1/2 Fermi gas. This experiment is an nice illustration of interesting physics resulting from the *separation of timescales* between spin and collisional dynamics. In my opinion, it is an excellent example of why cold gases are naturally suited to studying non-equilibrium dynamics. I simulate the experiment numerically using a collisionless Boltzmann equation and explain the observed spin dynamics both qualitatively and quantitively.

In Chapter 3, I continue the discussion of spin waves in thermal gases by

extending previous works on spin-1/2 gases to spin-1 Bose gases. In contrast to Chapter 2, the bulk of the work in this Chapter is analytic in nature. In particular, I find a spin wave instability in the thermal spin-1 Bose gas, which is the high temperature analog of the polar to ferromagnetic transition in a spin-1 Bose Einstein condensate.

In Chapter 3, I turn my attention to bosonic systems and briefly review the the Bogoliubov mean-field theory. I calculate the momentum distribution and density-density correlation function of an interacting Bose gas within the Bogoliubov framework. Then I consider bosons in an optical lattice, and introduce the Bose Hubbard model. I calculate the mean-field phase diagram of the Bose Hubbard model and then consider fluctuations about the mean field, and derive the excitation spectrum of the lattice gas in the superfluid and insulating regimes.

In Chapter 4, I ask what we learn by studying the dynamics of correlation functions following a sudden change in the interactions in a superfluid. Using the Bogoliubov theory developed in Chapter 3, I will show how the underlying excitation spectrum influences the long and short time behavior of the correlation functions. By considering a lattice dispersion, I study the analogous problem in a weak optical lattice and discuss how the lattice dispersion leads to additional features in the correlation functions. I will also discuss the timescale governing the revival of the condensate fraction in a quantum depleted gas.

In Chapter 5, I derive equations of motion governing the dynamics of one and two body correlation functions in the single-band Bose Hubbard model, applicable to bosons in deep lattices. I then consider a simple quench from a Mott insulating initial state to a weakly interacting final state and produce analytic expressions describing the dynamics of correlations following such a quench. I

discuss the timescale for the development of long range order following such a quench.

I study the problem of chapter 4 using an equations of motion approach. This approach complements the Bogoliubov approach of Chapter 4. First, I derive exact expressions for a quench to a non-interacting state. I then consider how interactions redistribute quasi-momentum to first order in perturbation theory in different dimensions.

In Chapter 6, I calculate the relevant timescales for *local* and *global* dynamics in *trapped* lattice Bose gases, a work done in collaboration with Dr. Kaden R. A Hazzard. Using a time-dependent Gutzwiller mean-field theory, I show that the timescale for *local* equilibration in these systems is fast in experimental terms. I then show that due to the spatial inhomogeneities inherent to cold gases, achieving global equilibrium can be quite complicated, sometimes taking longer than the lifetime of the experiment, an issue of practical importance to current day experiments.

I continue this discussion in Chapter 7 which is a collaborative work with experimentalists David McKay and Prof. Brian DeMarco from the University of Toronto and the University of Illinois, Urbana Champaign. Using experimental and numerical methods, we show that the rapid timescales for local dynamics in interacting systems invalidates a frequently used cold atom technique for mapping out the momentum distribution of atoms in an optical lattice.

BIOGRAPHICAL SKETCH

Stefan S. Natu was born to Indian parents on March 4 1985 in the town of Karlshruhe in Germany. Shortly thereafter he moved to the tiny island country of Bahrain, in the Middle East, where he completed his schooling. Following this, he moved to Delaware Ohio to obtain his undergraduate degree in Mathematics, with a minor in Physics at Ohio Wesleyan University. (He was not awarded the major for his failure to complete the "Advanced Lab" course.) After a brief stint at the Ohio State University, Stefan came to Cornell University to pursue a PhD in Physics, where he was promptly informed that he would have to take a lab course after all. Somewhere between Veit Elser's Quantum Mechanics class and the superfluid He-4 experiment in 510 Lab, he decided he wanted to be a theorist (a certain incident involving an equipment rack in Keith Schwab's lab might also be to blame) and study degenerate quantum gases. He continues to remain interested in this subject, largely due to the wide array of fascinating experiments driving this field forward. In the Fall of 2012, he spent 4 months at the Kavli Institute for Theoretical Physics as a Graduate Fellow. He is very excited to take up a postdoctoral position at the Joint Quantum Institute in Maryland.

To my parents

ACKNOWLEDGEMENTS

First and foremost, I would like to thank Erich Mueller, for being a constant source of ideas, and a wonderful advisor. I have a deep respect for his ability to throw "buzzwords" by the wayside and understand things for what they really are. His ability to develop intuitive pictures and write the simplest theory that retains all the relevant physics has left a deep impression on me. Equally impressive is his familiarity with the hairy details of experiments, and his wizard-like powers with Mathematica. I would like to thank him for supporting me as a Research Assistant for the past three years, and giving me the freedom to work on problems of my liking at my own pace. Over the years he paid for me to attend numerous conferences, workshops and summer schools where I learned a great deal. Finally I would like to thank him for giving me the wonderful opportunity to spend a semester at the Kavli Institute for Theoretical Physics.

I have learned a great deal through classes and discussions with the Cornell faculty. In particular, I would like to thank Viet Elser, Dan Ralph, Chris Henley, Jim Sethna, Piet Brouwer and Mukund Vengalattore for teaching wonderful courses. I would also like to thank Mukund for sharing his expertise on spinors with me and for teaching a great course on cold atoms. I can always count on him to ground me to the experimental realities while simultaneously encouraging me to "push the envelope". I thank Prof. Brian DeMarco from the University of Illinois for sharing his data with us and for the great collaboration that followed.

In addition to Physics faculty, I would like to thank Cecilia Lawless of the Romance Studies Department for introducing me to the world of Spanish literature. I would like to thank Pablo Cohen of the Ithaca College Music Faculty for his patience as I struggled with the classical guitar, and more recently Steve

Brown for sharing with me his love of jazz.

I would particularly like to thank a number of friends who have made these last 5 years so much fun. I have learned a great deal from my group mates: Dan Goldbaum, Sourish Basu, Kaden "K-Spaz" Hazzard, Stefan "B-Dub" Baur and Eliot Kapit. Kaden and Stefan deserve particular mention and I thank them for the unforgettable afternoons and evenings spent in various coffee shops around College town, talking about physics, women, and berating each another over meals well outside our budget.

Outside of the Mueller group I would like to thank Mark Fischer for numerous conversations on multi-band/muti-orbital materials, single malt whiskeys, unconventional superconductors, mixed martial arts and well, single malt whiskeys. I thank Naresh Kumar, Dan Wohns, Yoav Kallus, Josh Berger for being great housemates to spend three years with. I would like to thank Johannes Heinonen, Srivatsan Chakram, Ben Machta, Vikram Gadakar, Sumiran Pujari and Praveen Gowtham and many others for numerous discussions about physics and for their companionship during grad school. I would like to thank Pauli for that hilarious night in Portland and for encouraging me to take up Hebrew.

Over the years, I developed several friendships with the undergrads at Cornell, who always impressed me with their willingness to learn new things and take advantages of the many opportunities at Cornell. I would in particular like to thank KatieLee for being my closest friend over the years, for simultaneously being my supporter and my critic and challenging me in more ways than one.

I thank my family for their love and support throughout. In particular I thank my parents for always encouraging me to have a life outside of work.

Finally I would like to thank the National Science Foundation for supporting me over the years through Grant Nos. PHY-0456261, PHY-0758104 and 1066293 and PHY 1125915. I also thank the the Defense Advanced Research Project Agency (DARPA) for supporting me through the OLE Program. Part of the work discussed here was completed at the Aspen Center for Physics and the Kavli Institute for Theoretical Physics.

TABLE OF CONTENTS

LIST OF FIGURES

CHAPTER 1

INTRODUCTION TO ULTRA-COLD GASES

The field of ultra-cold atoms has been one of the most exciting and rapidly growing fields of physics of the past decade. Spurred on by rapid advances in imaging and cooling techniques, ultra-cold atoms are now capable of answering questions which were unheard of a few short years ago. The unprecedented control the experimentalist has on these ultra-cold atoms has allowed scientists working in the field to realize the dream of quantum emulation, whereby experimentalists can emulate properties of real materials in the pristine setting of ultra-cold gases by engineering a desired Hamiltonian and studying the phase diagram.

In this Chapter, I will overview some of the basic theory of ultra-cold gases. I will discuss some of the basic experimental techniques used to trap and cool atoms. Next I will discuss how atoms can be trapped in standing waves of light to create an optical lattice. I will then discuss how these trapped gases can be probed, in particular, I will focus on some of the newer probes that are shaping our understanding of these systems today.

1.0.1 Quantum Degenerate Gases

A non-interacting classical gas is described by a single length scale - the inter-particle spacing $l \sim 1/n^{-1/3}$ where n is the density. As the temperature is lowered, nothing happens. However as we know from our everyday experience, steam condenses to water at low temperatures which turns into ice in our freezers. The reason for this is that atoms are not "non-interacting", but rather they have weak

attractive interactions. At high temperature, the thermal kinetic energy of the atoms dominates over the attractive interaction and the system is in a gaesous phase. But when the temperature is lowered such that the attractive energy dominates over the kinetic energy, the atoms first condense into a liquid and eventually order into a solid, where the kinetic energy of the atoms is virtually frozen.

However this can be avoided in two ways: if the gas is extremely light then it is hard to pin down and will remain gaseous down to very low temperatures. A classic example of this is Helium, which turns liquid only at 4K or -268 Celsius. A second approach is to make the gas extremely dilute. Then the atoms are so far apart that they do not feel the attractive interactions that want them to order into a solid. It is this strategy that is used to make quantum degenerate gases in the laboratory. Indeed these cold gases are typically $8-10$ orders of magnitude less dense than air!

In order to understand what one can do with these ultra-dilute gases, one notes quantum mechanics introduces another length scale: the thermal de-Broglie wavelength

$$\Lambda_{th} = \frac{h}{\sqrt{2\pi m k_B T}} \tag{1.1}$$

where k_B is Boltzmann's constant and T is the temperature.

When this length scale becomes comparable to the inter-particle spacing, we expect quantum mechanics to dominate. From this we can estimate a temperature at which quantum effects should start to matter

$$T = \frac{h^2 n^{2/3}}{2\pi m k_B} \tag{1.2}$$

Plugging in the numbers for gaseous Helium with a density of $n \sim 10^{28}\mathrm{m}^{-3}$,

one finds that at $T \sim 5$K quantum mechanics becomes important in Helium. On the other hand, a typical quantum gas has a density of $n \sim 10^{18}\text{m}^{-3}$, one finds, $T \sim 500$nK. Therefore low densities imply that one has to go to extremely low temperature in order to observe quantum mechanical phenomena. This is one of the biggest challenges to cold gases and later in this chapter I will discuss some of the ingenious techniques developed by experimentalists to attain these temperatures.

First, lets understand what happens when a gas of neutral atoms is cooled down to these temperatures.

1.0.2 Bose-Einstein condensation

One of the most elegant phenomena in nature is that of Bose-Einstein condensation, whereby a gas of bosons cooled below a certain temperature occupies a single macroscopic eigenstate. A key feature of this transition is that it occurs for *non-interacting* particles, which means that the transition is driven purely bosonic statistics alone.

To see this, consider a gas of N particles confined in a box of dimensions L^3. At finite temperature, the number of particles can be expressed as

$$N = \sum_k n_k = \sum_k \frac{1}{e^{\beta\epsilon_k - \mu} - 1} \tag{1.3}$$

where $\beta = 1/k_B T$, and n_k is the Bose occupation factor for the kth orbital which has energy $\epsilon_k = \hbar^2 k^2/2m$, where $k = 2\pi n/K$ for integers n. We also introduce the chemical potential μ as a Lagrange multiplier which fixes the number of particles. In order to ensure that n_k is always positive, μ must be less than the

lowest single particle energy state, which in this case is $\epsilon_{k=0} = 0$, *i.e*, μ must be negative.

In the thermodynamic limit, one can convert the sum into an integral in the usual fashion $1/V \sum_k = \int d^3k$ where V is the volume, one finds that the density obeys

$$n = \frac{N}{L^3} = \int \frac{d^3k}{2\pi\hbar^3} \frac{1}{e^{\beta\epsilon_k - \mu} - 1} = \frac{m^{3/2}}{\sqrt{2}\pi^2\hbar^3} \int_0^\infty d\epsilon \frac{\sqrt{\epsilon}}{e^{\epsilon-\mu} - 1} \tag{1.4}$$

The integral on the right hand side is bounded by its vaue at $\mu = 0$ which is $\beta^{-3/2}\sqrt{\pi/2}\zeta(3/2)$ where ζ is the Riemann zeta function. As a result, if the number of particles exceeds a threshold number, the equality in Eq. 1.4 can no longer be satisfied. Alternatively, for a fixed density, when the temperature is lowered below a certain value

$$T_{BEC} = \frac{2\pi\hbar}{m}\Big(\frac{n}{\zeta(3/2)}\Big)^{3/2} \tag{1.5}$$

the equality is no longer satisfied.

When this occurs, the gas undergoes a phase transition where all the particles begin to cram into the lowest single particle state. For a bosonic gas, this is the $k = 0$ state and this phenomenon is called Bose Einstein condensation (BEC). As the temperature is lowered even further, more and more particles occupy the $k = 0$ state, until at zero temperature, all the particles are said to be "condensed". Bose-Einstein condensation of alkali atoms was achieved for the first time in 1995 by three groups [1, 2, 3].

I remark that He-4 was the first example of a Bose-Einstein condensate. However the interactions in helium are so strong that even at zero temperature, the fraction of condensed atoms is little over 10 percent. Hence it is widely regarded that alkali atoms furnished the first example of an ideal Bose Einstein

condensate.

1.1 Degenerate Fermi gases

Although this thesis is primarily concerned with bosonic atoms, I briefly remark on the exicting story of ultra-cold fermions. Unlike the case of bosons which occupy a single eigenstate at low temperatures, fermions are constrained by the Pauli exclusion principle, which forbids identical fermions from occupying the same quantum state. As a result, in three dimensions fermionic particles fill up states upto a fixed momentum called the Fermi momentum

$$k_F = 6\pi^2 n^{1/3} \tag{1.6}$$

which is only a function of the density. Therefore all the way down to $T = 0$, there is no phase transition in the non-interacting Fermi gas.

The story of fermions however becomes extremely rich as soon as interactions are included. In 1957 Bardeen, Cooper and Schriefer showed that *arbitrarily* weak attractive interactions render the Fermi surface unstable to the so-called "Cooper" instability: whereby fermions of opposite spins, living on opposite sides of the Fermi sphere pair up into Cooper pairs which behave as bosons and undergo Bose condensation [4].

A natural question to ask is what happens when this interaction is made so strong that quantum mechanics allows for a bound state to form. It turns out that making the interactions stronger leads to a smooth crossover between a BCS superfluid at weak interactions to a molecular condensate (BEC) for strong interactions. Although this was theoretically studied by Leggett, and Nozières

and Schmitt-Rink in the early 80s [5, 6], it wasn't until 2005 when experiments using ultra-cold ^{6}Li were able to use magnetic fields to tune the atomic interactions to enable studying this crossover quantitatively [7, 8, 9, 10]. Understanding of the BCS-BEC crossover is one of the major accomplishments of ultra-cold gases in recent years.

1.1.1 Energy scales in ultra-cold gases

In this section I will discuss how these dilute *neutral* ultra-cold atoms interact. Throughout this thesis I consider alkali atoms, atoms with a filled inner shells and a single electron occupying the outermost *s*-orbital. Since alkali atoms are basically just large hydrogen atoms, their atomic structure is easily understood. At the temperature of ultra-cold gases, the atoms are in their electronic ground state. Furthermore, since the electrons occupy the *s* orbital, there is no magnetic field arising from the electronic *orbital* angular momentum and one has to consider solely the hyperfine interaction between the spin or the electron with the nuclear magnetic moment.

For an atom with nuclear spin I and electronic spin $S = 1/2$, there are only two possible values for the total angular momentum $F = I + S = I \pm 1/2$. The energy scale corresponding to this interaction is on the order

$$E_{hf} \sim \frac{m_e}{m_p}\alpha \left[m\frac{e^4}{(4\pi\epsilon_0\hbar)^2}\right] \tag{1.7}$$

where $\alpha = e^2/(4\pi\epsilon_0\hbar c) = 1/137$ is the fine structure constant and the quantity in brackets is the Hartree $E_H = me^4/(4\pi\epsilon_0\hbar)^2 = 27$eV is twice the ground state energy of the hydrogen atom. Plugging in the fact that $m_e/mp \sim 10^{-3}$ and that $\alpha \sim 10^{-2}$ and that 1eV $\sim 10^4$K, one finds that the temperature scale correspond-

ing to the hyperfine structure is on the order $E_{hf} \sim 0.1$K. Understanding these energy scales will be crucial to understand the cooling and trapping of these atoms which we shall consider in a later section.

1.2 Atomic interactions

The atoms we are dealing with are neutral, therefore the dominant interaction between them is a weak dipole-dipole type van der Waals interaction which scales as r^{-6}. However once the atoms are so close that their electronic clouds begin to overlap, the Coulomb repulsion takes over, giving rise to a sharp repulsive barrier at short distances. Furthermore the two ground state atoms can either be in the singlet or triplet electronic state, giving rise to a single and a triplet potential. In the triplet state the spins are pointing in the same direction, giving rise to additional Pauli blocking, as a result the triplet potential is typically much shallower than the singlet potential. Furthermore, when two atoms come close to one another, scattering processes can cause transitions between the various *hyperfine* levels (channels), and as a result, the scattering of two atoms is in general a complicated multi-channel problem.

However these cold gases are *dilute* in the sense that the mean interatomic separation $l \sim n^{-1/3} \sim 1000 a_B$ where $a_B = 0.5$Å is the Bohr radius. Meanwhile the range of the van der Waals potential $r_0 \sim 10 a_B$. As a result, the atoms never get close enough to one another that they can explore the complex details of the scattering potential. As a result, one can integrate out these short range (high energy) degrees of freedom, and obtain an *effective* interaction which correctly reproduces the long range, low energy scattering properties. It is the aim of

this section to derive such an effective interaction for two atoms (bosonic or fermionic) of equal mass m. I will make use of Appendix A, which contains a brief review of scattering theory.

The relative wave-function describing the scattering of two particles takes the form:

$$\psi_{\mathbf{k}} = (2\pi)^3\delta(\mathbf{k}-\mathbf{k}^{'}) + \psi_{sc}(\mathbf{k}) \tag{1.8}$$

where ψ_{sc} is the scattered wave.

This wave-function obeys the Schrödinger equation:

$$\Big(\frac{\hbar^2k^2}{2m} - \frac{\hbar^2k^{'2}}{2m}\Big)\psi_{sc}(\mathbf{k}) = U(\mathbf{k},\mathbf{k}^{'}) + \frac{1}{V}\sum_{k^{''}} U(\mathbf{k},\mathbf{k}^{'})\psi_{sc}(\mathbf{k}^{''}) \tag{1.9}$$

where $E = \frac{\hbar^2k^2}{2m}$ is the energy and $U(\mathbf{k},\mathbf{k}^{'})$ is the Fourier transform of the bare atomic interaction, which is in general complicated.

The above equation can be formally solved to yield

$$\psi_{sc}(\mathbf{k}) = \Big(\frac{\hbar^2k^2}{2m} - \frac{\hbar^2k^{'2}}{2m} + i\delta\Big)^{-1}T(\mathbf{k}^{'},\mathbf{k};E) \tag{1.10}$$

$$T(\mathbf{k}^{'},\mathbf{k};E) = U(\mathbf{k},\mathbf{k}^{'}) + \frac{1}{V}\sum_{k^{''}} U(\mathbf{k},\mathbf{k}^{''})\Big(E - \frac{\hbar^2k^{''2}}{2m} + i\delta\Big)^{-1}T(\mathbf{k}^{''},\mathbf{k};E)$$

where we have introduced the T matrix, which contains all the details about the potential and satisfies the Lippmann-Schwinger equation.

Thus far we have made no approximations. But now we note that at large distances and low energies $E = k = 0$, the scattered wave can be calculated from Eq. 1.10 using

$$\frac{1}{4\pi r} = \int \frac{d\mathbf{k}^{'}}{(2\pi)^3}\frac{e^{i\mathbf{k}^{'}\cdot\mathbf{r}}}{k^{'2}} \tag{1.11}$$

to get

$$\psi_{sc}(\mathbf{r}) = -\frac{mT(0,0;0)}{4\pi\hbar^2 r} \tag{1.12}$$

As shown in Appendix A, the large distance properties of the scattered wave-function can be encapsulated in terms of a single parameter, the s-wave scattering length a, which is related to the T-matrix using Eq. A:

$$a = \frac{m}{4\pi\hbar^2} T(0,0;0) \tag{1.13}$$

Thus the scattering T-matrix $T = 4\pi\hbar^2 a/m$ can be regarded as the effective interaction as it properly captures all the long range scattering properties at low energies. Note that this interaction is simply a *contact* interaction, as it is independent of momentum and thus is a δ function in real space.

To summarize, to describe low energy dilute quantum gases one simply replaces the complicated two-body interaction potential U with the $T(0,0;0)$. I showed that the interactions between ultra-cold gases can be described by

$$\mathcal{H}_{int} = g \int d^3\mathbf{r} \psi^\dagger_\alpha(\mathbf{r}) \psi^\dagger_\beta(\mathbf{r}) \psi(\mathbf{r}) \psi(\mathbf{r}) \tag{1.14}$$

where the parameter g is in general a spin dependent *constant*. For spinless bosonic atoms of equal mass m, or fermions of two hyperfine levels: $g = 4\pi\hbar^2 a/m$.

What we have done above amounts to making the Born approximation for scattering. To understand the sense in which this is an approximation, we replace $U(\mathbf{k}, \mathbf{k}^{'})$with g and plug into the expression for the full T-matrix Eq. 1.10. We find that

$$T(\mathbf{k}^{'}, \mathbf{k}; E) = g + \frac{g}{V} \sum_{k^{''}} \Big(E - \frac{\hbar^2 k^{''2}}{2m} + i\delta \Big) T(\mathbf{k}^{''}, \mathbf{k}; E) \tag{1.15}$$

This equation can be integrated to yield

$$T(\mathbf{k}^{'}, \mathbf{k}; E) = \frac{g}{1 - \frac{g}{V} \sum_{k^{''}} \left(E - \frac{\hbar^2 k^{''2}}{2m} + i\delta \right)^{-1}} \tag{1.16}$$

Taking the zero energy limit as before one has that $T(\mathbf{k}^{'}, \mathbf{k}; E) = 4\pi\hbar^2 a/m$ and one finds that

$$\frac{4\pi\hbar^2 a}{m} = \frac{g}{1 - \frac{g}{V}\sum_{k''}\left(-\frac{\hbar^2 k''^2}{2m} + i\delta\right)^{-1}} \tag{1.17}$$

which can be integrated for a particular choice of cutoff Λ on the k-integral. The reason for this cutoff is that the delta potential is problematic in that the integral doesn't converge. (This can be readily checked by expanding Eq. 1.17 to second order. This is because the delta function potential does not fall off in momentum space, unlike a real potential should. This problem is circumvented by choosing an appropriately regularized pseudopotential or by introducting a momentum cutoff Λ.

It is precisely in this sense that we are making a "low energy approximation" *i.e* we are integrating out the high energy (short range) degrees of freedom. In the limit of $\Lambda \to \infty$, no approximations are being made, whereas the Born approximation amounts to setting $\Lambda = 0$. In the case of the van der Waals potential, a natural cutoff is afforded by the range of the potential r_0. Therefore for a given scattering length, one can find the corresponding g, which reproduces the correct low energy behavior.

1.3 Trapping and Cooling of Ultra-cold gases

I now introduce the reader to the basic methods to trap and cool ultra-cold gases. Everything discussed in this section can be found in several excellent review articles such as [11]. These techniques are used ubiquitously throughout cold atoms, irresepective of the nature of the experiment or the type of atom. In the next section, I will discuss how atoms are trapped in optical lattices and

introduce the basic models for thinking about atoms in optical lattices.

The first step in any experimental procedure is to slow down an initially hot gas of atoms. Slowing down the atoms lowers their kinetic energy, hence lowers their temperature. Slowing is usually performed in a Zeeman slower.

Following this the atoms can be further cooled using optical means. This method is known as Doppler cooling or *optical molasses* whereby laser beams detuned red to the atomic transition are applied to the atoms. An atom moving towards the lasers experience a "blue" shift which puts the laser beam in resonance with an atomic transition. Consequently, the atom absorbs a photon and gets a momentum kick in the opposite direction which slows it down. Doppler cooling is typically limited by the natural linewidth (Γ) of the transition which is typically much larger than the recoil energy $\Gamma \gg E_r = \hbar^2 k^2/2m$ where $k = 2\pi/\lambda$ is the photon wave-vector. Using their knowledge of atomic spectra, experimentalists typically use a so-called "narrow"-line transition $\Gamma \sim E_r$ which allows one to attain far lower temperatures. At optical wave-length $E_r \sim 10\mu$K temperatures are obtained using this technique.

Next the atoms are transferred to a magnetic or optical trap for further cooling. A magnetic trap relies on the fact that atoms experience a force in the presence of a magnetic field gradient. A set of magnets produce a magnetic field gradient which produces a potential with a local minimum at some point in space, in the case of a quadrupole trap, $|B| = 0$ at the local minimum, varying linearly away from this point. Atoms are trapped at this local minimum. A subtlety involving magnetic traps is that if the magnetic field is small enough, spin flip transitions can occur leading to a loss of atoms. One way around this is to move the minimum around in space dynamically in a way such that the

average magnetic field is non-zero everywhere. An alternate approach is to add a second magnet which creates a magnetic field at the center, eliminating these losses. The resulting trap has a harmonic profile $V(R) = \frac{1}{2}m\omega^2R^2$, where R is the distance from the center. [12].

Magnetic traps suffer from a major disadvantage namely that the presence of a magnetic field forces the atoms into a particular spin state, thus freezing out the spin degree of freedom. A way around this is to trap atoms purely optically [13]. As a result of this the spin of the atoms is no longer constrained, which allowed experimentalists to study the properties of *spinor* gases, particularly spin-1 and spin-2 bosons.

Once the atoms are trapped, further cooling is done using a process known as *evaporative cooling* where the higher energy atoms are systematically removed from the trap. Higher energy atoms are found on the edges of the trap, and these can be removed by simply lowering the trap depth. As this process naturally leads to atom loss, the initial atom number transferred into the trap needs to be high. Evaporative cooling is one of the most successful cooling techniques and is used in all cold-atom experiments. It was the use of this technique that led to the observation of Bose-Einstein condensation in 1995.

A major component in evaporative cooling is the role of *collisions*. As we have seen (Appendix A) identical fermions do not interact with one another and this poses unique challenges to cooling fermions. The situation is exacerbated in magnetic traps where only a few hyperfine states can be trapped and their collisional properties need to be favorable in order to achieve maximum cooling efficiency. ^{40}K is known to have two stable magnetically trappable states and was cooled to quantum degeneracy in 1999 in the group of Debbie Jin [14].

However one of the workhorse fermi gases, ^{6}Li does not have two magnetically trappable states and hence cannot be evaporatively cooled in a magnetic trap.

A way around this is to use *sympathetic* cooling, whereby the fermionic sample interact with a *bath* of other atoms (either fermionic or bosonic) which removes heat from the sample [15]. A better way is to use optical traps which can confine both low and high field seeking atoms. It was this technique that allowed several groups working on ^{6}Li to attain quantum degeneracy and thereby enabled the study of fermionic physics [16, 17, 18, 19].

1.3.1 Optical trapping

The advent of optical trapping immensely expanded the scope of ultra-cold gases. Paricularly relevant to the subject of this thesis are "optical lattices" where atoms are trapped in the minima of a standing wave created by interfering two laser beams. In this section, I describe how atoms interact with light fields [20].

Atoms can be thought of as tiny dipoles, and thus an electric field interacts with an atom with an energy

$$U_{dip} = \frac{1}{2} e\mathbf{r}.\mathbf{E} = \frac{1}{2}\epsilon_0 \chi E^2 \tag{1.18}$$

where $\mathbf{E} = \mathbf{E}_0 e^{i\mathbf{k}\cdot\mathbf{r}} \cos(\omega t)$ is the electric field, and $e\mathbf{r}$ is the displacement induced in the atom which to linear order is given by $er = \epsilon_0 \chi \mathbf{E}$ where ϵ_0 is the permittivity of free space and χ is the polarizability of the atom.

Treating this potential as a perturbation to the initial Hamiltonian of the atom, the shift in the atomic energy levels can now be calculated to *second* order

in perturbation theory. The first order term vanishes for atoms in their electronic ground states, as they have no permanent dipole moments, hence $\langle\psi|\mathbf{r}|\psi\rangle = 0$.

In order to make progress, we make the simple assumption that the atom can be treated as a two level system, with a ground $|g\rangle$ and excited $|e\rangle$ states with energies E_g and E_e respectively. The atom-light interaction Hamiltonian can then be written as:

$$\mathcal{H}_{a-l} = eE_0 \cos(\omega t)|\langle g|\mathbf{r}|e\rangle\ |e\rangle\langle g| + h.c \tag{1.19}$$

where we have assumed that the wave-length of the radiation is much larger than the size of the atom ($\mathbf{k}\cdot\mathbf{r} \ll 1$). For brevity, we define $\gamma = e\ \langle g|\mathbf{r}|e\rangle E0$.

As the new Hamiltonian is not diagonal in the original basis, and has time-dependence, we write the new wave-function $\psi(t) = c_g(t)e^{-iE_g/\hbar t}|g\rangle + c_e(t)e^{-iE_e/\hbar t}|e\rangle$ where the co-efficients c_e and c_g can in general be complex and are time-dependent.

The equations of motion for the coefficients now read

$$\begin{aligned} i\frac{\partial c_g}{\partial t} &= \gamma^* e^{i\omega_0 t}\cos(\omega t)c_e \\ i\frac{\partial c_e}{\partial t} &= \gamma e^{-i\omega_0 t}\cos(\omega t)c_g \end{aligned} \tag{1.20}$$

where $\omega = (E_e - E_g)/\hbar$ is the energy splitting of the unperturbed states.

Expressing the cosine term in terms of exponentials one obtains:

$$\begin{aligned} i\frac{\partial c_g}{\partial t} &= \frac{1}{2}\gamma^*(e^{i(\omega_0+\omega)t} + e^{i(\omega_0-\omega)t})c_e \\ i\frac{\partial c_e}{\partial t} &= \frac{1}{2}\gamma(e^{-i(\omega_0-\omega)t} + e^{-i(\omega_0+\omega)t})c_g \end{aligned} \tag{1.21}$$

Next we make the so-called rotating wave approximation (RWA) in quantum optics where we assume that the $\omega + \omega_0$ term is oscatillating so fast that we can

simply replace it with its average value 0. Retaining simply the slower term, we define $\delta = \omega_0 - \omega$ to be the *detuning* of the light from the atomic resonance. The resulting equation can be expressed as a matrix equation by making the transformation $c_{g/e} = e^{\mp i\delta t/2}\tilde{c}_{g/e}$ to get:

$$\begin{aligned} i\frac{\partial \tilde{c}_g}{\partial t} &= \frac{\delta}{2}c_g + \frac{\gamma}{2}c_e \\ i\frac{\partial \tilde{c}_e}{\partial t} &= -\frac{\delta}{2}c_e + \frac{\gamma}{2}c_g \end{aligned} \tag{1.22}$$

which is readily solved to yield the perturbed energies $E^{(2)} = \pm\frac{1}{2}\sqrt{\delta^2 + \gamma^2}$.

Now, when there is no perturbing light field, $\gamma = 0$ and $\omega = 0$, one obtains the unpertubed energy levels which are separated by energy ω_0. In the limit where the detuning is much larger than γ and one can expand $E^{(2)}$ to get

$$E^{(2)} = \pm\frac{1}{2}\Big(\delta + \frac{\gamma^2}{2\delta}\Big) \tag{1.23}$$

This effect is known as the A.C. Stark effect. Typical experiments work in this regime of large laser detuning. Note that one still requires that δ be small compared to the bare atomic resonance ω_0 to justify the RWA.

The perturbed energies are proportional to the intensity of the laser light which scales as E^2. Furthermore, it is sensetive to the sign of δ, which can be chosen to be both positive and negative. For example if the laser light is *red* detuned (detuning $\delta < 0$), the atoms are attracted to the intensity *maxima*, as their energy is lowered from its unperturbed value. The opposite is true for *blue* detuned light, where the atoms are repelled from the intensity maxima. Thus by choosing a particular spatial profile for the intensity, one can shape the energy landscape of the atoms. It is this fact that is exploited to make optical lattices, which are discussed in the following section.

1.4 Optical Lattices

The creation of optical lattices has revolutionalized the scope of ultra-cold gases. In solid state systems, electrons live on an underlying crystal lattice created by the atoms. As a result, nearly all the theoretical models that exist for understanding strongly correlated systems are lattice models. Creating an optical lattice thus brought cold atoms one step closer to the goal of quantum emulation. In this section, I discuss how an optical lattice of bosons can be used to realize the Bose Hubbard model, a model which will be studied extensively throughout this thesis [21].

As discussed in the Sec. 1.3.1 on optical trapping, a *single* red detuned laser beam generates a Gaussian profile in which the atoms live. The simplest *optical lattice* is created by taking two such counter-propagating lasers and creating an standing wave with half the wave-length of the laser beams. The resulting potential takes the form

$$V(\mathbf{r}, z) = -V_0 e^{-2r^2/w^2(z)} \cdot \sin^2(kz) \tag{1.24}$$

where V_0 is the depth of the lattice potential, w is the beam waist as before and $k = 2\pi/\lambda$ is the wave-vector of the light.

In order to create a 2D or a 3D lattice, one simply needs to mimic this configuation in orthogonal directions. This allows experimentalists to emulate 1, 2 and 3 dimensional systems. This has been particularly relevant to the cuprate high temperature superconductors where the physics behind the superconductivity is believed to be contained in the 2D dimensional copper-oxygen planes [22].

Near the trap center, on length scales much smaller than the beam waist, we

can ignore the Gaussian and obtain a purely lattice optential

$$V_{lat} = V_0\Big(\sin^2(kx) + \sin^2(ky) + \sin^2(kz)\Big) \tag{1.25}$$

A natural unit to use for optical lattices is the recoil energy $E_r = \frac{\hbar^2 k^2}{2m}$.

Now I consider the single particle quantum mechanics in a lattice potential. The single particle eigenstates in a periodic potential $V(r) = V(r + R)$ are the so-called Bloch functions $\phi_{n,q}$ characterised by a discrete band index n and a quasi-momentum $\mathbf{q}$ within the first Brillouin zone of the lattice [23]. The Fourier transform of the Bloch functions are the so-called Wannier functions which form a complete basis

$$\phi_{n,q}(\mathbf{r}) = \sum_R w_{n,R} e^{i\mathbf{q}\cdot R} \tag{1.26}$$

where R is a lattice vector.

As the wannier functions form an orthonormal basis, the operator to create or annihilate a boson at position r can be expressed as

$$\psi(\mathbf{r}) = \sum_{R,n} w_n(\mathbf{r} - \mathbf{R}) a_{R,n} \tag{1.27}$$

where $a_{R,n}$ is the corresponding annihilation operator for particles in the wannier states.

Therefore the Hamiltonian describing the motion of particles on a discrete lattice can now be written as

$$\mathcal{H}_{kin} = \sum_{R,R',n} J_n(\mathbf{R} - \mathbf{R}') a^\dagger_{\mathbf{R},n} a_{\mathbf{R}',n} \tag{1.28}$$

where the parameter J_n is known as the hopping parameter and can be determined by the expression

$$J_n(R) = \int d\mathbf{r} w^*(\mathbf{R} - r)\Big[-\frac{\hbar^2}{2m}\nabla_r^2 + V_{lat}\Big] w(\mathbf{r} - \mathbf{R}) \tag{1.29}$$

For deep lattices, the atoms are localized in the lowest band of the optical lattice, and it suffices to consider $n = 0$. The Wannier functions tend to be quite short-ranged, typically J is non-zero for nearest neighbors and falls of rather rapidly from then on. As a result, one can reduce Eq. 1.28 to a nearest neighbor hopping model

$$\mathcal{H}_{kin} = -J \sum_{\langle ij \rangle} (a_i^\dagger a_j + h.c) \tag{1.30}$$

where the notation $\langle i\, j \rangle$ represents nearest neighbor sites.

In a similar manner the interaction Hamiltonian (Eq. 1.14) can be expressed as a lattice Hamiltonian with an effective interaction U given by

$$U = 4\pi\hbar^2 a/m \int d\mathbf{r} |w(\mathbf{r})|^4 \tag{1.31}$$

to yield

$$\mathcal{H}_{int} = \frac{U}{2} \sum_i a_i^\dagger a_i^\dagger a_i a_i \tag{1.32}$$

Adding the kinetic and interaction terms, yields the Bose Hubbard model

$$\mathcal{H}_{BH} = -J \sum_{\langle ij \rangle} (a_i^\dagger a_j + h.c) + \frac{U}{2} \sum_i a_i^\dagger a_i^\dagger a_i a_i \tag{1.33}$$

In this manner, bosons in a standing optical potential realize the Bose Hubbard Hamiltonian. This approximation breaks down in shallow lattices, where the effects of higher bands become more important. This happens when the band-spacing, which is comparable to the local harmonic oscillator energy spacing becomes comparable to E_r. Since the local harmonic oscillator energy is comparable to V_0, we require $V_0 \gg E_R$.

Furthermore once interactions are included, the Bose Hubbard model is only valid in the limit where the bandgap is larger than the interactions or the temperature. The interaction energy is given by gn_0 where n_0 is the local density. In

deep lattices $n \sim 1/l^3$ where l is the local harmonic oscillator spacing $l = \hbar/\sqrt{m\omega_0}$, where ω_0 is the local harmonic oscillator frequency. One requires this energy scale to be much smaller than E_r, which sets the bandgap. This requirement is satisfied whenever the scattering length $a \ll l$.

Finally, the single band, nearest neighbor Bose Hubbard model itself is only valid when the wannier functions fall off sufficiently quickly, which implies that the spacing between individual sites $d = \lambda/2$ be much larger than the local oscillator length l. Thus the Bose Hubbard Hamiltonian is valid whenever

$$a \ll l \ll d \tag{1.34}$$

In typical experiments, $d \sim \mu$m, $a \sim$nm, so this requirement is easy to satisfy.

1.5 Probes of Ultra-cold gases

I conclude this chapter with a discussion of various ways to probe ultra-cold gases. Although there are a number of ways to probe cold gases, here I will focus only on a few important ones that are both new and relevant to the topics discussed in this thesis.

1.5.1 Time-of-flight Imaging

The simplest probe of a cold gas is time-of-flight, which implies a sudden switch off of all the lattice and trapping potentials and merely watching the atoms expand as they fall under gravity. After a certain time, atoms are illuminated by

laser light. Since atoms absorb light, the intensity of the outgoing light (I_f) is different from that of the incoming light (I_i).

In particular, one has the basic result of absorption imaging:

$$\frac{I_f}{I_i} = e^{-\sigma \int n(r,z)dz} \tag{1.35}$$

where the light is assumed to travel in the $z-$ direction and σ is the atom-light scattering cross-section.

Now the basic idea behind time of flight is the following. Immediately following the turn off of all trapping potentials, the cloud begins to expand rapidly, resulting in a dramatic reduction in the density over a very short period of time. As a result, once can neglect interactions during time of flight and assume that the cloud expands *ballistically*. Under this assumption the shadow picture taken by the CCD camera can be used to obtain the 3D density $n_{3D}^{TOF}(\mathbf{r})$ which can be related to the *momentum distribution* before time-of-flight using the relation $\mathbf{k} = \frac{m\mathbf{x}}{\hbar t}$. Therefore one has

$$n^{TOF}(\mathbf{x}) = \langle \psi_{TOF}^{\dagger}(\mathbf{r}) \psi_{TOF}(\mathbf{r}) \rangle \rightarrow \langle a_{trap}^{\dagger}(k) a_{trap}(k) \rangle \tag{1.36}$$

Note that for strongly interacting systems, atoms tend to expand *hydrodynamically* due to the interactions and one has to account for this in order to use this technique. Alternatively, one switches off all the interactions extremely rapidly prior to turning off the magneto-optic potentials.

Time of flight is one of the most popular techniques used in cold gases. In particular, it is used to detect the formation of a Bose-Einstein condensate. A BEC is characterized by the macroscopic occupation of a single momentum state. As a result, the momentum distribution following time-of-flight shows

a sharp peak at $k = 0$ for temperatures below T_{BEC} indicating the onset of Bose condensation.

In chapter 7 we will discuss *bandmapping* which is the analog of this method applied to lattice systems.

1.5.2 High resolution imaging

I now discuss two recent high resolution imaging techniques recently developed for bosonic systems, independently in the groups of Markus Greiner at Harvard [24], Immanuel Bloch at Munich [25] and Cheng Chin at Chicago [26]. The Greiner and Bloch group have similar setups and I will discuss these first.

The goal of these experiments is to be able to resolve *individual* atoms on a lattice. Earlier this had been done for lattices with a large spacing of 5μm, which was so large that there was essentially no tunneling between the atoms [25], and the atoms were frozen in space. Through a series of technological breakthroughs, experimentalists at Harvard and Munich are now able to much smaller lattice spacings, thus enabling the atoms to become itinerant.

The basic idea is to create a two dimensional gas by confining atoms to a tight trap in the $z-$ direction with a trapping frequency of $\sim$ 10KHz. In the transverse directions, interfering light beams create an optical lattice with a spacing of .5μm. The gas is illuminated by a large aperture microscope placed $\sim$ 1μm from the 2D gas. A key advantage of the microscope is that it can be used to *project* arbitrary shape potentials that the atoms then experience. These potentials can be lithographically generated on a mask. Improvements in this tech-

nology in the last 2 years has allowed for the projection of nearly defect-free potentials.

The detection of the individual atoms is done by first ramping up the laser intensity, and thus the optical lattice depth to freeze out all atomic motion. Light is then shined on the atoms and the scattered fluorescence light is then captured and imaged. A key limitation to this imaging technique is that illuminating light on trapped atoms can result in light assisted collisions, which lead to molecule formation. The resulting molecule is no longer trapped and exits the system. As a result, the imaging system can only detect an empty site or a singly occupied site. Multiple occupancies exit the trap in pairs.

In Fig. 1.5.2 I show a schematic plot of the Harvard setup and the resulting image.

An analogous technique has been developed in the group of Cheng Chin, which also allows for the *in-situ* measurement of density profiles [26]. While the Munich and Harvard setups can image individual sites, the setup at Chicago produces an image that is coarse grained over 2-3 lattice spacings. The main difference between the two setups is in the imaging system. While the Harbard and Munich setups perform fluorescence imaging and thus measure the local parity on a given site, the Chicago setup uses absorption imaging to take a picture of the two dimensional density profile.

Using this, Cheng Chin was able to observe the *wedding cake* density profile characteristic of the Bose Hubbard model in a trap in deep lattices. As the Harvard and Munich schemes only measure the parity of the occupation number, this technique works extremely well in deep lattices where number fluctuations

are suppressed. However the Chicago scheme is well suited even for superfluids where number fluctuations are large. For example, one is able to extract the *local* compressibility from the density profiles in the superfluid and Mott insulating regimes. Additionally, by taking the Fourier transform of these density fluctuations, one can calcuate the static structure factor of the 2D gas.

In Chapters 4 – 7 we will discuss some of the interesting questions regarding *dynamics* of strongly correlated Bosonic systems in optical lattices that have been possible to address experimentally due to the advances discussed here.

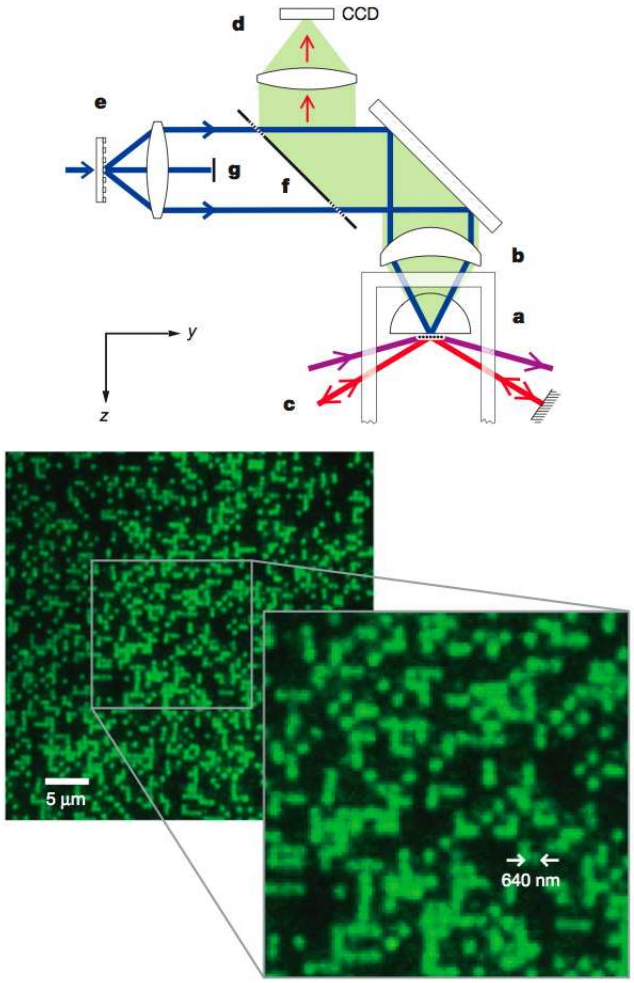

Figure 1.1: **Single-site resolved imaging of a 2D Lattice Bose gas** (Top) The atoms are located in the position marked **a**, close ot the aperturre of the microscope. The lattice is imprinted using laser beams as shown in **e**. Addtional beams are applied in the z direction to tightly confine the atoms in a two-dimensional geometry, and the resulting fluorescence image is collected in **d**.(Bottom) Resulting fluorescence image collected by the camera showing individual atoms. The grid is artificially imposed to match the lattice spacing of 5μm. The images are directly obtained from [24].

BIBLIOGRAPHY

[1] M. H. Anderson, J. R. Ensher, M. R. Matthews, C.E. Wieman and E. A. Cornell, Science **269** 198 (1995).

[2] K. B. Davis, M.-O Mewes, M. R. Andres, N. J. van Druten, D. S. Durfee, D. M. Kurn and W. Ketterle, Phys. Rev. Lett. **75** 3969 (1995).

[3] C. C. Bradley, C. A. Sackett, J. J. Tollett and R. J. Hulet, Phys. Rev. Lett. **75** 1687 (1995).

[4] J. Bardeen, L. N. Cooper and J. R. Schieffer, Phys. Rev. **108** 1175 (1957).

[5] A. J. Leggett in *Modern Trendes in the Theory of Condensed Matter* (Springer-Verlag) 1980

[6] P. Nozières and S. Schmitt-Rink, J. Low. Temp. Phys. **59** 195 (1985).

[7] M. Zwierlein, C.A. Stan, C. H. Schunk, S. M. F. Raupach, A. J. Kerman and W. Ketterle, Phys. Rev. Lett. **92** 120403 (2004)

[8] C. A. Regal, M. greiner and D. S. Jin, Phys.Rev. Lett. **92** 040403 (2004).

[9] T. Bourdel, L. Khaykovich, J. Cubizolles, J. Shang F. Chevy, M. Teichmann, L. Tarruell, S. J.J. M.M Kokkelmans and C. Salomon Phys. Rev. Lett. **93** 050401 (2004).

[10] K. E. Strecker, G. B. Partridge, and R. G. Hulet, Phys. Rev. Lett. **91** 080406 (2003).

[11] W. Ketterle and M. W. Zwierlein, Ultracold Fermi Gases, Proceedings of the International School of Physics, (IOS Press, Amsterdam 2006).

[12] D. E. Pritchard, Phys. Rev. Lett. **51** 1336 (1983).

[13] D.M.Stamper-Kurn, M.R.Andrews, A.P.Chikkatur, S.Inouye, H.J.Miesner, J.Stenger, and W.Ketterle, Phys.Rev.Lett., **80** 2027 (1998).

[14] B. Demarco and D. S. Jin, Science **285** 1703 (1999).

[15] A. G. Truscott, K. E. Strecker, W. I. McAlexander, G. B. Partridge, and R. G. Hulet, Science **291** 2570 (2001).

[16] Z. Hadzibabic, C. A. Stan, K. Dieckmann, S. Gupta, M. W. Zwierlein, A.Gorlitz and W. Ketterle, Phys. Rev. Lett. **88** 160401 (2008).

[17] S. R. Granade, M. E. Gehm, K. M. O'Hara, and J. E. Thomas Phys. Rev. Lett. **88** 120405 (2002).

[18] F. Schreck, L. Khaykovich, K. L. Korwin, G. Ferrari, T. Bourdel, J. Cubizolles and C. Salomon Phys. Rev. Lett. **87** 080403 (2001).

[19] S. Jochim, M. Bartenstein, A. Altmeyer, C. Hendl, S. Riedl, C. Chin, J. Hecker-Denschlag and R. Grimm Science **302** 2101 (2003).

[20] C. Foot *Atomic Physics* (Oxford University Press, Oxford 2005).

[21] I. Bloch, J. Dalibard, and W. Zwerger, Rev. Mod. Phys. **80** 885 (2008).

[22] P. W. Anderson, Science **237** 1196 (1987).

[23] N. W. Ashcroft and N. D. Mermin *Solid State Physics* (Holt, Reinhardt and Winston, New York 1976).

[24] W. S. Bakr, J. I Gillen, A. Peng, S. Fölling and M. Greiner, Nature **462** 74 (2009).

[25] J. F. Sherson, C .Weitenberg, M. Endres, M. Cheneau, I. Bloch and S. Kuhr Nature **467** 68 (2010).

[26] N. Gemelke, X. Zhang, C-L. Hung and C. Chin, Nature **460** 995 (2009).

[27] K. Nelson, X. Li and D. Weiss, Nature Phys **3** 556 (2007).

[28] C-L. Hung, X. Zhang, L-C. Ha, S-K Tung, N. Gemelke and C. Chin, New Journal of Physics **13**075019 (2011).

CHAPTER 2

COLLISIONLESS SPIN-WAVE DYNAMICS IN A SPIN-1/2 FERMI GAS: A NUMERICAL STUDY

This Chapter was adapted from "Anomalous Spin segregation in a weakly interacting two-component Fermi gas", by Stefan S. Natu and Erich J. Mueller, which is published in Physical Review A (R) 79 051601 (2009). In this chapter I show how by carefully tuning parameters, one can obtain very interesting dynamics, even for a thermal gas

2.1 Introduction

In this Chapter, I study spin waves in a *thermal* spin-1/2 Fermi gas. By tuning the interacting strength using a magnetic field, experimenalists Du, Luo, Clancy and Thomas at Duke created a gas of spin-1/2 atoms so weakly interacting that the s-wave scattering length (a) was on the order of Å s [1]. Furthermore, the gas was a *thermal* gas, with the temperature $T \sim 4E_F$, several orders of magnitude larger than the interaction energy. The experiment thus realized a gas in the so-called *Knudsen* regime, where the mean collision time τ_{coll} was much longer than the time for *coherent* spin precesion due to exchange effects. As a result the cloud developed a spin texture of alternating spin $\uparrow$ and spin $\downarrow$ domains, with a length scale comparable to the cloud size.

Here I provide an explanation for this phenomenon using a collisionless Boltzmann equation. As seen in experiments, I find that slight differences in the trapping potentials in the two spin states drive small spin currents. Hartree-Fock type interactions convert these currents into a redistribution of popula-

tions in energy space, and consequently a long lived spin texture develops. I explore the interaction strength dependence of these dynamics, finding nontrivial dependence on system parameters and close agreement with experiment. My approach was motivated by discussions with John Thomas, who has recently explored a simplified version of this theory in a work with Du, Luo, and Clancy [2]. A concurrent study by Piéchon, Fuchs, and Laloë [3] reached similar conclusions.

A typical assumption employed in spin wave theory is the assumption of local equilibrium. In this case the mean collision time of the gas given by $\tau_{coll} \sim 1/(nv\sigma)$ where $v \sim \sqrt{k_B T/m}$ and $\sigma = 4\pi a^2$ is the collision cross-section is so short that collisions rapidly establish local equilibrium before any spin dynamics can develop. In such a system, spin waves can be treated with linear response theory or hydrodynamics, and the local magnetization which develops is much smaller than the total density $M(\mathbf{r}) = (n_\uparrow(\mathbf{r}) - n_\downarrow(\mathbf{r}))/(n_\uparrow(\mathbf{r}) + n_\downarrow(\mathbf{r})) \ll 1$. Experiments at JILA studying spin waves in ultra-cold bosonic ^{87}Rb were in this regime [4, 5, 6, 7].

The experiments at Duke were in the so called collisionless or Knudsen regime where the mean collision time was longer than the lifetime of the experiment. In this limit, exchange effects dominate and the gas is *not* in local equilibrium. As a result, the usual hydrodynamic approach of considering small deviations from equilibrium fails, and spin waves become a non-linear effect. A manifestation of this is that the local magnetization $M(\mathbf{r}) \sim O(1)$. This regime was thoroughly studied several groups [8, 9, 10, 11, 12] and soon confirmed by experiments on spin polarized Hydrogen [13, 14, 15].

In the Duke experiments [1] a cold gas ($T/T_F \sim 4$) of roughly 2×10^5, ^{6}Li

atoms, in their lowest hyperfine state (denoted $\sigma = \downarrow$), was prepared in an optical plus magnetic trap with a trapping potential of the form $U_\downarrow = \frac{1}{2}m\omega_R^2 r^2 + \frac{1}{2}m\omega_{Z,\downarrow}^2 Z^2$, with $\omega_R = 2\pi \times 4360\text{Hz}$ and $\omega_{Z,\downarrow} = 2\pi \times 145\text{Hz}$. A radio pulse was used to coherently transfer atoms into a superposition of the $\downarrow$ and the next hyperfine level (denoted $\uparrow$). The subsequent dynamics were observed for several different bias magnetic fields, hence several different scattering lengths.

When the scattering length was small and negative they observed that after $\sim 100\text{ms}$ of evolution, the two components of the gas segregate axially with the $\uparrow$ component moving inward, and the other moving outward. This spin texture persisted on timescales of a few seconds, much longer than the timescale for small oscillations. When the sign of the scattering length was changed, the $\uparrow$ moved outward and the $\downarrow$ moved inward. When the scattering length was tuned to zero, no dynamics was seen.

This behavior is striking. According to hydrodynamic spin wave theory [14, 5], the characteristic timescale for any oscillations should be given by the axial oscillator time, roughly two orders of magnitude faster than the observed dynamics. Moreover the only possible mechanism for driving this spin segregation is the very slight difference in the axial trap potential $\frac{d^2}{dz^2}[(U_\uparrow - U_\downarrow)] \sim 2\pi(4.4 \times 10^{-4})\text{Hz}/\mu\text{m}^2$. It is surprising that such a small difference in the trap leads to such dramatic density redistributions.

An intuitive picture of these dynamics is presented by Du *et al.* [2]. They note that since the time-scale of spin rearrangement is long compared to the oscillation period, local equilibrium is never attained. Instead, each atom's spin dynamics is controlled by a mean field, averaged over its periodic trajectory. Low energy atoms that spend more time in high density regions experience a

greater mean field. The ↓ atoms see a slightly weaker trapping potential and hence, for a given energy, have trajectories which extend over more space. This results in those atoms seeing a smaller mean field. The net result of the subsequent dynamics is a spin segregation in energy space.

Here I show how this behavior plays out in phase space. Below, I derive an effective 1D collisionless Boltzmann equation, capable of describing the dynamics of the quasi-1 dimensional Boltzmann gas in Ref. [1]. Solving this equation numerically, I reproduce the experimental observations.

2.2 Model

At the temperatures of interest ($T \sim 27\mu$K) one only needs to consider s-wave scattering and the Hamiltonian reduces to

$$\hat{H}(t) = \sum_{\sigma=\uparrow,\downarrow} \int d\mathbf{r}\, \Psi^\dagger_\sigma(\mathbf{r},t)\left(-\frac{1}{2m}\nabla^2_r + U_\sigma(r)\right)\Psi_\sigma(\mathbf{r},t) + g \times \int d\mathbf{r}_1 \Psi^\dagger_\uparrow(\mathbf{r}_1,t)\Psi^\dagger_\downarrow(\mathbf{r}_1,t)\Psi_\downarrow(\mathbf{r}_1,t)\Psi_\uparrow(\mathbf{r}_1,t), \tag{2.1}$$

where the field operators obey the fermionic equal time anti-commutation relations $\{\Psi^\dagger_\sigma(\mathbf{r}_1,t), \Psi_{\sigma'}(\mathbf{r}_2,t)\} = \delta(\mathbf{r}_1 - \mathbf{r}_2)\delta_{\sigma,\sigma'}$, and $g = \frac{4\pi a}{m}$ with s-wave scattering length a. Near the magnetic fields of interest, the scattering length dependence on magnetic field can be approximated by $a(B) = -3.5(B - B_0)a_B/G$ [1]. I have set $\hbar = 1$ throughout, and I work in the Larmor frame rotating with a frequency equal to that of the ↓→↑ transition for a uniform gas.

Given the small scattering lengths, and low densities in this experiment

($a \sim 4a_B$, $n \sim 10^{12}\text{cm}^{-3}$), the mean collision time $\tau = 1/(n\sigma v) \sim 10$ s is much longer than the timescale of the experiment, and interactions only enter at the mean field level. From experimental studies of relaxation in a single component gas [1], it appears that the time between background collisions τ_b, due to an imperfect vacuum, is also on the order of several seconds. For times short compared to τ and τ_b, one can describe the system in terms of a collisionless Boltzmann equation, where the system is described by a Hartree-Fock approximation. The long timescales involved in collisional relaxation also explain why a simple hydrodynamic theory does not capture the physics of the phenomenon.

Following [1], I use the Heisenberg equations for Ψ_σ(r, t) to derive the equations of motion for the spin dependent Wigner function

$$\begin{aligned} \overleftrightarrow{\mathbf{F}} &= \begin{pmatrix} f_{\uparrow\uparrow}(\mathbf{p},\mathbf{R},t) & f_{\uparrow\downarrow}(\mathbf{p},\mathbf{R},t) \\ f_{\downarrow\uparrow}(\mathbf{p},\mathbf{R},t) & f_{\downarrow\downarrow}(\mathbf{p},\mathbf{R},t) \end{pmatrix} \\ f_{\sigma\sigma'}(\mathbf{p},\mathbf{R},t) &= \int d\mathbf{r} e^{-i\mathbf{p}\cdot\mathbf{r}} \langle \Psi^\dagger_\sigma(\mathbf{R}-\frac{\mathbf{r}}{2},t)\Psi_{\sigma'}(\mathbf{R}+\frac{\mathbf{r}}{2},t)\rangle, \end{aligned} \tag{2.2}$$

which is the quantum analogue of the classical distribution function. I refer the reader to Appendix B and C for a more thorough discussion of Wigner functions. Here $\mathbf{p}$ represents the momentum, $\mathbf{r} = \mathbf{r}_1 - \mathbf{r}_2$ is the relative coordinate and $\mathbf{R} = \frac{\mathbf{r}_1+\mathbf{r}_2}{2}$ is the center of mass coordinate. Taking moments of the Wigner function [1], one obtains equations involving densities, spin densities and currents such as

$$\begin{aligned} \langle s_{\sigma,\sigma'}(\mathbf{R},t)\rangle = \langle \Psi^\dagger_\sigma(\mathbf{R},t)\Psi_{\sigma'}(\mathbf{R},t)\rangle &= \int \frac{d\mathbf{p}}{(2\pi)^3} f_{\sigma\sigma'}(\mathbf{p},\mathbf{R},t) \\ \langle \mathbf{j}_{\sigma\sigma'}(\mathbf{R},t)\rangle &= \int \frac{d\mathbf{p}}{(2\pi)^3}\mathbf{p} f_{\sigma\sigma'}(\mathbf{p},\mathbf{R},t) \end{aligned} \tag{2.3}$$

I define $s_{\sigma\sigma} = s_\sigma$, $s_{\uparrow\downarrow} = s_+$, $s_{\downarrow\uparrow} = s_-$ and analogously for the spin currents. Here $s_\pm$ refer the spin raising and lowering operators that are related to the

transverse components of the spin s_x and s_y in the usual way $s_\pm = s_x \pm i s_y$.

Throughout, I use upper-case letters to denote the components of position and momentum, and lower-case letters to denote the spin degrees of freedom. These transverse spin components represent a quantum coherence which is not captured by a classical model of a two component gas. The z-spin density is $s_z(\mathbf{R},t) = s_\downarrow(\mathbf{R},t) - s_\uparrow(\mathbf{R},t)$, and the particle number is $N = \int d\mathbf{R}\; s(\mathbf{R},t)$ where $s(\mathbf{R},t) = s_\uparrow(\mathbf{R},t) + s_\downarrow(\mathbf{R},t)$. Assuming that all potentials are slowly varying in space and time, one finds

$$\frac{\partial}{\partial t}\overleftrightarrow{\mathbf{F}} + \frac{\mathbf{p}}{m}\cdot\nabla_{\mathbf{R}}\overleftrightarrow{\mathbf{F}} = i[\overleftrightarrow{\mathbf{V}},\overleftrightarrow{\mathbf{F}}] + \frac{1}{2}\{\nabla_{\mathbf{R}}\overleftrightarrow{\mathbf{V}},\nabla_{\mathbf{p}}\overleftrightarrow{\mathbf{F}}\} \tag{2.4}$$

where the potential matrix is

$$\overleftrightarrow{\mathbf{V}} = \begin{pmatrix} U_\uparrow^{eff} & -g s_+ \\ -g s_- & U_\downarrow^{eff} \end{pmatrix} \tag{2.5}$$

and the effective potentials are $U_\uparrow^{eff}(R,t) = U_\uparrow(R) + g s_\downarrow(\mathbf{R},t)$ and $U_\downarrow^{eff}(R) = U_\downarrow(R) + g s_\uparrow(\mathbf{R},t)$. Commutators and anti-commutators are respectively given by square brackets and braces. The diagonal terms of the potential matrix include the direct contribution to forward scattering, while the off diagonal components represent the exchange contribution. A detailed derivation of Eq. 2.4 is presented Appendix B and closely follows the analogous derivation for a spinless gas in Ref. [1].

Given the differences between the radial and axial trapping frequencies, the relevant dynamics of the system are one-dimensional. In the nondegenerate limit that I consider here one can reduce (Eq. 2.5) to a one dimensional Boltzmann equation by making the ansatz: $f(\mathbf{p},\mathbf{R},t) = f(p_\perp,p_Z,R_\perp,Z,t) = f(p_\perp,R_\perp)f(p_Z,Z,t)$, where the notation $\perp$ has been used to denote the transverse

directions. The initial distribution is assumed to be a stationary state of the non-interacting Boltzmann equation for spin-down particles:

$$f_{\sigma\sigma'} = \frac{A}{2} e^{-\beta\left(p_Z^2/2m + U_\uparrow(Z)\right)} e^{-\beta\left(p_\perp^2/2m + U(R_\perp)\right)} \tag{2.6}$$

where the prefactor $A = N\omega_z\omega_r^2/(k_BT)^3$ is defined such that the constraint $N = \int d\mathbf{R}(s_\uparrow(\mathbf{R},t) + s_\downarrow(\mathbf{R},t))$ is satisfied.

By assuming the above Gaussian density profile, I express the 3D density as

$$s^{3D}_{\sigma\sigma'}(\mathbf{p}, R_\perp, Z, t) = \frac{A}{2}\int \frac{d\mathbf{p}}{(2\pi)^3} f_{\sigma\sigma'}(\mathbf{p}_\perp, R) f_{\sigma\sigma'}(p_Z, Z, t) = \int \frac{d^2p_\perp}{(2\pi)^2} f_{\sigma\sigma'}(p_\perp, R) s^{1D}_{\sigma\sigma'}(Z,t) \tag{2.7}$$

where I have defined

$$s^{1D}_{\sigma\sigma'}(Z,t) = \frac{A}{2}\int \frac{dp_Z}{2\pi} f_{\sigma\sigma'}(p_Z, Z, t) \tag{2.8}$$

Spatial averaging in the transverse direction renormalizes the coupling constant by $\frac{1}{2}$ [5]. Finally, integrating the transverse momentum coordinates yields an effective interaction strength $g^{1D} = \frac{1}{8\pi^2} gN(m\omega_z)(\omega_r/k_BT)^2$.

2.3 Results and Discussion

Working in units where lengths and momenta are measured in terms of the oscillator length $(m\omega_z)^{-1/2}$ and $(mk_BT)^{1/2}$ respectively, I use a phase space conserving split-step approach [18] to integrate Eq. (2.5), using a 20 by 20 by 800 grid in Z-p_Z-t with step sizes $\delta Z = 20\ (m\omega_z)^{-1/2}$, $\delta p_Z = 0.6\ (mk_BT)^{1/2}$, and $\delta t = 0.04\frac{2\pi}{\omega_z}$. The grid was chosen to be sufficiently fine so that our results no longer depended on the step sizes.

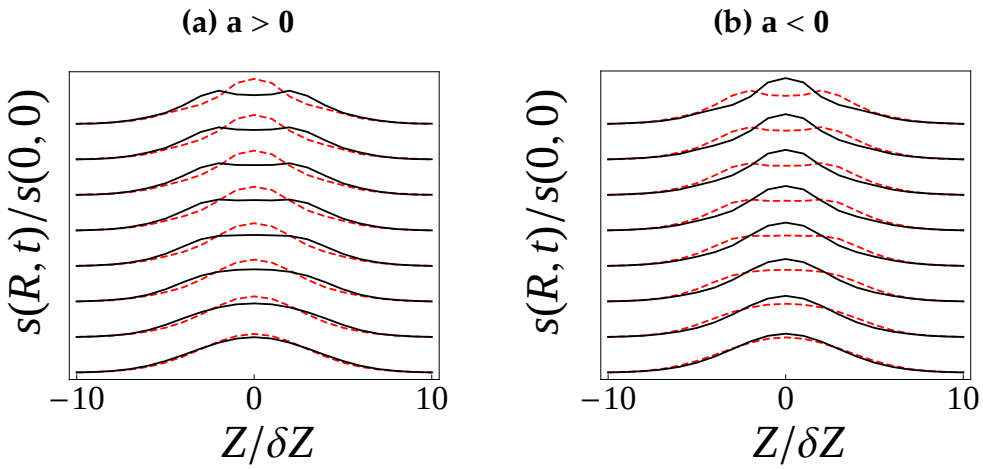

Figure 2.1: Time evolution of one-dimensional densities $s_\uparrow$ and $s_\downarrow$: The up- (black, solid), and down- (red, dashed) spin density in space (horizontal axis in units of $\delta Z = 20\ (m\omega_z)^{-1/2}$) for (a) $a = 4.5a_B$, (b) $a = 0$ and (c) $a = -4.5a_B$, where a_B is the Bohr radius. Time runs from bottom to top, with each offset density profile is separated by 25ms. No dynamics are seen on this scale for $a = 0$.

As in the experiment, I initialize the system in a transversely magnetized state along s_x. The trapping parameters for the spin ↑ and spin ↓ atoms were identical to the experiment. In Fig. 2.1, I show the time evolution of the density profile for the up (black/solid curve) and down spins (red/dashed curve) in space for the first 200 ms. I plot the behavior for positive and negative values of the scattering length, finding that the timescales are in agreement with experiment [1].

In Fig. 7.4 (top), I quantify the magnitude of the spin segregation by plotting the central density difference ($s_z = s_\downarrow - s_\uparrow$), normalized to the total density ($s = s_\uparrow + s_\downarrow$) as a function of time for a range of scattering lengths. This quantity peaks near $t \sim 200$ ms. I extract the timescale associated with spin segregation by taking the slope of the graph at small times (Fig. 7.4(b) green curve) to find

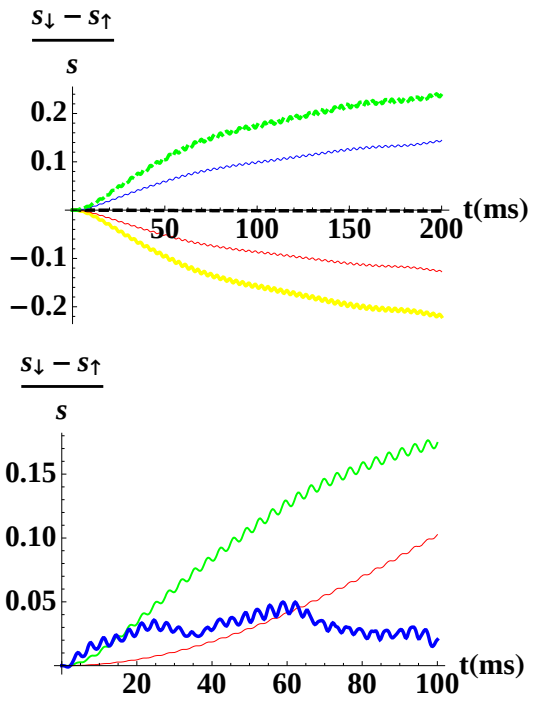

Figure 2.2: Left: Central spin density difference ($s_z(0,t) = s_\downarrow(0,t) - s_\uparrow(0,t)$) normalized to the total central density ($s = s_\uparrow(0) + s_\downarrow(0)$) for various scattering lengths. The total central density is constant in time. Bottom to top: $a = -4.55\ a_B$, $a = -2.45\ a_B$, $a = 0\ a_B$, $a = 2.8\ a_B$, and $a = 4.55\ a_B$.Right: First 100ms of evolution of s_z/s for $a = 4.55\ a_B$, and different values of $\delta\omega = \omega_\uparrow - \omega_\downarrow$: thin (red) – $2\pi \times 0.15$ mHz, green – $2\pi \times 1.5$ mHz, thick (blue) – $2\pi \times 15$ mHz. The green curve corresponds to the experimental value of $\delta\omega$.

$\frac{d}{dt}\frac{s_z(0,t)}{s} \sim 1/200\ (\text{ms})^{-1}$ for $a = 4.55 a_B$. Furthermore, the figure reveals oscillations in the spin density difference at a frequency $\sim 2\pi 300$ Hz ($\sim 2\omega_z$) that is weakly dependent on the interaction strength, corresponding to the lowest breathing mode of a two component Fermi gas [3]. The amplitude of these oscillations depends on the difference in the trap frequencies seen by the ↑ and ↓ atoms. These oscillations are not captured in the analysis presented in [2].

In previous experiments on bosons [4], the spin dynamics were much faster than such collective modes. This difference can be attributed to the ratios of the

mean field interaction energy to the trap frequency $\lambda = g^{1D}/\omega_z$. In the current experiment $\lambda \sim 0.2$ while in [4], $\lambda \sim 10$.

Fig. 7.4 (bottom) shows that both the magnitude and timescale for spin segregation seen in [1] is strongly dependent on the difference in trapping frequencies ($\delta\omega = \omega_\uparrow - \omega_\downarrow$). Had this frequency difference in [1] been an order of magnitude larger (blue/ thick curve in Fig. 7.4(b)), the dynamics would have been much more complicated and much less dramatic.

As previously discussed, an important observation in [2] was that the spin segregation in [1] can be viewed as a segregation in phase space. To illustrate this I plot in Fig. 2.3 by plotting the phase space distributions for $a = -4.5a_B$ for $t = 0$, 100 and 200 ms respectively. One sees that the phase space distributions are not separately functions of Z and p_Z, but instead depend on $\omega_z^2 Z^2 + p_Z^2/m$. This is a unique feature of the Knudsen gas, and does not occur in the hydrodynamic limit where the spin dynamics can be viewed purely as a spin texture in *real* space.

Finally I note that this spin segregation is very robust. I can illustrate this by exciting a large amplitude spin dipole mode at $t = 0$. Spin segregation occurs even as the $\uparrow$ and $\downarrow$ atoms slosh around in the trap, out of phase with one another. As may be expected for a gas in the Knudsen regime, oscillations on timescales much shorter than the interactions do not change the long term dynamics. Nonetheless, it would be interesting to observe this stability experimentally.

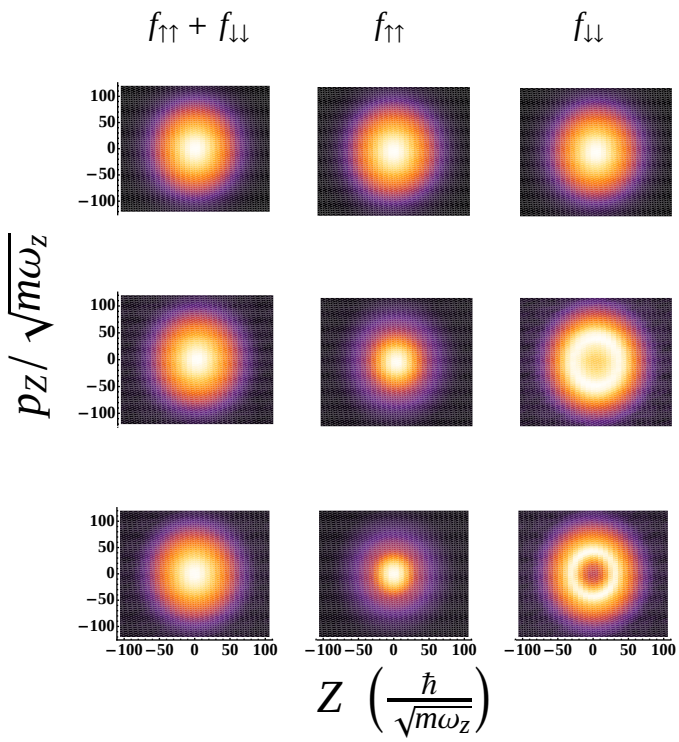

Figure 2.3: Spin segregation in phase space. Lighter colors represent higher density. The total phase space distribution (left column), up-spin distribution (middle column) and down spin distribution (right column) at $t = 0$ (top row), $t = 100$ms (center row) and $t = 200$ms (bottom row) for $a = -4.5\ a_B$ are shown. The phase space distribution is only a function of energy, but it is not of a simple Boltzmann form.

2.4 Summary and Conclusions

Using standard techniques [1], I have derived a collisionless Boltzmann equation which reproduces the anomalous spin waves seen in [1]. This is an exciting regime for spin waves, as the system is far from local equilibrium. Remarkably we find an ergodicity where the phase space distribution function is only a function of energy – but is not a simple exponential.

My numerical simulations indicate that this spin segregation depends

strongly on the difference in the trapping frequencies seen by the two spin species. Moreover, despite being in a nondegenerate regime, substantial quantum coherences are found in this system.

Much can be learned from studying how these collisionless dynamics evolve into hydrodynamics as the scattering length is made larger. A recent experiment in the group of Martin Zwierlein studied the properties of a colliding cloud of spin $\uparrow$ and $\downarrow$ atoms in the strongly interacting regime [20]. Remarkably they observed that the clouds simply bounced off one another, penetrating very slowly over a timescale of roughly a second, demonstrating high resistance to the flow of spin current. Such experiments can be nicely modelled by a Boltzmann equation but collisions play a crucial role in the dynamics.

In Appendix C, I derive the Boltzmann equation using the equations of motion approach by Kadanoff and Baym [1]. I then derive a general matrix collision integral for the two component Fermi gas, which is the natural generalization of Eq. 2.4 to strongly interacting systems.

BIBLIOGRAPHY

[1] X.Du, L.Luo, B.Clancy, and J.E. Thomas, Phys. Rev. Lett. **101** 150401 (2008).

[2] X.Du, Y.Zhang, J.Petricka, and J.E.Thomas, Phys. Rev. Lett. **103** 010401 (2009).

[3] F.Piéchon, J.N.Fuchs and F.Laloë, Phys. Rev. Lett. **102** 215301 (2009).

[4] H.J. Lewandowski, D.M. Harber, D.L.Whitaker, and E.A. Cornell, Phys. Rev. Lett. **88** 070403 (2002).

[5] M.Ö.Oktel and L.S. Levitov, Phys. Rev. Lett **88**, 230403 (2002).

[6] J.E.Williams, T. Nikuni, and Charles W. Clark, Phys. Rev. Lett. **88**, 230405 (2002).

[7] J.N.Fuchs, D.M.Gangardt, F. Laloë, Phys. Rev. Lett. **88**, 230404 (2002).

[8] E. P. Bashkin, JETP Lett. **33** (1981); JETP **60** 1122 (1984).

[9] V.P.Silin, Sov. Phys. JETP **6**, 945 (1958).

[10] A.J.Legett, J.Phys C **3** 448 (1970).

[11] C. Lhuillier and F. Laloë, J.Phys (Paris) **43** 197 (1982).

[12] C. Lhuillier and F. Laloë, J.Phys (Paris) **43** 225 (1982).

[13] B.R. Johnson, J.S. Denker, N.Bigelow, L.P.Levy, J.H. Freed, and D.M. Lee, Phys. Rev. Lett. **52** 1508 (1984).

[14] L.P. Levy and A.E. Ruckenstein, Phys. Rev. Lett. **52**, 1512 (1984).

[15] N.P.Bigelow, J.H. Freed and D.M. Lee, Phys Rev. Lett., **63** 1609 (1989).

[16] J. W. Jeon and W. J. Mullin, J. Phys. France **49** (1988).

[17] *Quantum Statistical Mechanics*, L. P. Kadanoff, and G. Baym, W. A. Benjamin, Inc. 1962.

[18] *Numerical Recipes Third Edition: The Art of Scientific Computing* W.H.Press, S.A. Teukolsky, W.T.Vetterling, and B.P.Flannery, Cambridge University Press, 2007.

[19] *Bose-Einstein Condensation in Dilute Gases* C.J.Pethick and H.Smith, Cambridge University Press, 2002.

[20] A. Sommer, M. Ku, G. Roati and M. Zwierlein, Nature **472** 201 (2011).

CHAPTER 3

MEAN-FIELD MODELS FOR BOSONS AT ZERO TEMPERATURE

3.1 Introduction

In this chapter I will overview two simple models describing bosons which will be used extensively throughout this thesis. I start by considering a homogeneous gas of bosons described and discuss the Bogoliubov mean-field approach. I will introduce the model, derive the excitation spectrum and calculate one body and two body correlation functions. I then discuss their properties and how they can be measured. Next I will discuss the phenomenology of lattice bosons using the single-band Bose Hubbard model. I will describe the static properties of this model using a Gutzwiller mean-field theory, and calculate the zero temperature phase diagram. Finally I consider time-dependent fluctuations about this theory and calculate the excitation spectrum of the gas. For simplicity, I will limit myself to three dimensions.

In Chapter 4, I will use the Bogoliubov theory developed here to calculate the properties of correlation functions following a quench. In Chapters 5 – 7 I will extensively use time-dependent Gutzwiller theory to study a variety of experimentally relevant problems. I will try and convince the reader that the simple picture I develop here actually does a remarkable job in explaining puzzling features in recent experiments on bosons in optical lattices.

3.2 Bogoliubov mean-field theory for bosons

Consider a homogeneous gas of bosons in 3 dimensions, interacting with a repulsive s-wave contact interaction. The Hamiltonian for the system in momentum space is written as:

$$\mathcal{H} = \sum_k \left(\epsilon_k - \mu\right) a_k^\dagger a_k + \frac{g}{2V} \sum_{pqk} a_{p+q/2}^\dagger a_{k-q/2}^\dagger a_k a_p \qquad (3.1)$$

where $g = 4\pi a\hbar^2/m > 0$ where a is the s-wave scattering length. The operator a_k annihilates a boson with momentum k and obeys the standard bosonic commutation relations $[a_k, a_{k'}^\dagger] = \delta_{k,k'}$ and $[a_k, a_{k'}] = 0$. In free space, the dispersion $\epsilon(k) = \frac{\hbar^2 k^2}{2m}$ and the chemical potential μ fixes the number of particles N and V is the volume.

The ground state of the interacting system is a macroscopically occupied $k = 0$ single particle state *i.e* $N_0 = \langle a_{k=0}^\dagger a_{k=0}\rangle = N$. In the thermodynamic limit, where N and V tend to infinity keeping N/V constant, one has $a_0|N_0\rangle = \sqrt{N_0}|N_0 - 1\rangle \approx \sqrt{N_0}|N_0\rangle$ and we can thus replace the operators a_0 and $a_0^\dagger$ with a real c-number $\sqrt{N_0}$. Fixing the total number of particles requires $\mu = gn_0$, the Hartree mean-field energy of the condensate.

The Bogoliubov mean-field theory assumes that interactions are weak, *i.e* the number of excited atoms $N_{ex} = \sum_{k\neq 0}\langle a_k^\dagger a_k\rangle$ is small compared to the number of condensed atoms. Thus to lowest order, one retains only those terms in the interaction Hamiltonian which have two or more powers of a_0. One finds:

$$\sum_{pqk} a_{p+q/2}^\dagger a_{k-q/2}^\dagger a_k a_p = |a_0|^4 + |a_0|^2 \sum_{q\neq 0} (a_{q/2}^\dagger a_{-q/2}^\dagger + a_{q/2} a_{-q/2} + 4 a_q^\dagger a_q) \qquad (3.2)$$

Including the kinetic energy term and rearranging terms one obtains the Bogoliubov hamiltonian

$$\mathcal{H}_{bog} = \frac{gN_0^2}{2V} + \sum_{k\neq 0} \left(\epsilon_k - \mu + 2gn_0\right) a_k^\dagger a_k + \frac{gn_0}{2} \sum_{k\neq 0} (a_k^\dagger a_{-k}^\dagger + a_k a_{-k}) \tag{3.3}$$

where $n_0 = N_0/V$ is the condensate density.

The first term in this expression is proportional to $gN_0^2/V \sim gN^2/V$ is the mean-field energy of the condensate. The second term is the kinetic energy of the excited atoms supplemented by a Hartree-Fock shift arising from the interaction with the condensate. The third term corresponds to the scattering or two atoms from states with momenta p and $-p$ to the condensate and vice-versa.

The resulting Bogoliubov Hamiltonian is quadratic in the a_k operators and can be diagonalized by making the transformation $a_k = u_k b_k - v_k^* b_{-k}^\dagger$ where u_k and v_k are complex numbers and b_k, and $b_k^\dagger$ satisfy the Bose commutation relations. The commutation relations enforce that $u_k^2 - v_k^2 = 1$ for all k.

Inserting this transformation into Eq. 3.3, and forcing all terms with two powers of b_k or $b_k^\dagger$ to zero, one obtains a non-interacting Hamiltonian for the quasi-particles:

$$\mathcal{H}_{qp} = \sum_k E_k b_k^\dagger b_k \tag{3.4}$$

where

$$E_k = \sqrt{\epsilon_k(\epsilon_k + 2gn_0)} \tag{3.5}$$

and the co-efficients u_k and v_k satisfy:

$$u_k = \sqrt{\frac{1}{2}\left(\frac{\epsilon_k + gn_0}{E_k} + 1\right)} \tag{3.6}$$

$$v_k = -\sqrt{\frac{1}{2}\left(\frac{\epsilon_k + gn_0}{E_k} - 1\right)}$$

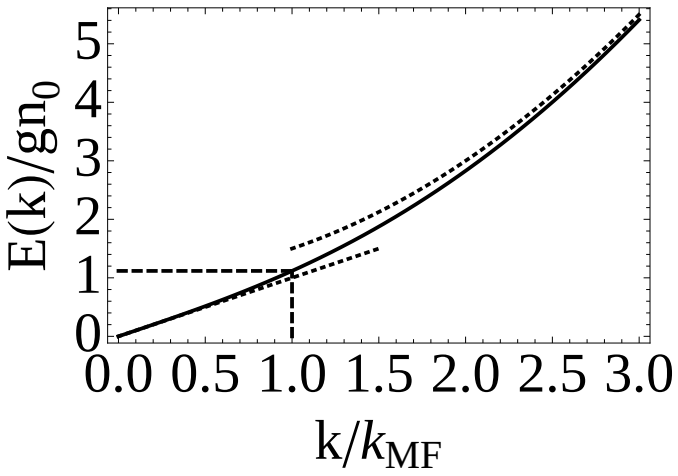

Figure 3.1: **Bogoliubov dispersion** Dispersion of a weakly interacting Bose gas. For momenta smaller than $k_{MF} = \sqrt{ngn_0}/\hbar$, the dispersion is linear with a sound speed $c = \sqrt{gn_0/m}$. For momenta larger than k_{MF}, the dispersion becomes free particle-like. The energy where the dispersion changes character is set by the chemical potential $\mu = gn_0$.

For a non-interacting gas, $u_k = 1$ and $v_k = 0$.

Thus the Bogoliubov transformation yields a dispersion $E_k = \sqrt{\epsilon_k(\epsilon_k + 2gn_0)}$, which is plotted in Fig. 3.1. For small $k \ll k_{MF} = \sqrt{ngn_0}/\hbar$, this dispersion is *linear* in k, corresponding to an undamped sound-like excitation with sound velocity $c = \sqrt{gn_0/m}$. For large $k \gg k_{MF}$, one recovers the usual quadratic dispersion of a non-interacting gas. The momentum at which the dispersion changes character $k_{MF} = \sqrt{mgn_0}/\hbar$ is the inverse healing length of the condensate.

Since the Bogoliubov Hamiltonian is a non-interacting Hamiltonian in the b_k operators, all thermodynamic properties of the gas can be readily derived. At finite temperature, one has that $\langle b_k^\dagger b_k \rangle = g(k) = (e^{\beta E_k} - 1)^{-1}$, the Bose distribution, where $\beta = 1/k_B T$.

The number of excited atoms is given by

$$N_{ex} = \langle a_k^\dagger a_k \rangle = \sum_k |v_k|^2 + \sum_k (u_k^2 + v_k^2) g(k) \tag{3.7}$$

The first term is the so called "quantum depleted" fraction, which is the number of non-condensed atoms arising purely from quantum fluctuations. The second term is the thermal component. The condensate fraction is one of the most commonly measured probes in cold gases and it is obtained by time-of-flight imaging of an expanding cloud.

At zero temperature, substituting Eq. 3.6, we find that the density of excited atoms $n_{ex} = \zeta^{-3}/(3\pi^2)$ where $\zeta = \hbar/\sqrt{mgn_0}$ is the condensate healing length. Thus there is roughly one excited particle per ζ^{-3}. Substituting for $g = 4\pi a\hbar^2/m$, we find that $n_{ex}/n = \frac{8}{3\sqrt{\pi}}\sqrt{(na^3)}$.

Another useful quantity to consider is the density-density correlation function $g^{(2)}(\mathbf{r} - \mathbf{r}') = \sum_{\mathbf{q}} e^{i\mathbf{q}\cdot(\mathbf{r}-\mathbf{r}')}\langle \rho_{\mathbf{q}}\rho_{-\mathbf{q}}\rangle$ where $\rho_{\mathbf{q}} = \sum_{\mathbf{k}} a^\dagger_{\mathbf{k}+\mathbf{q}} a_{\mathbf{k}}$. This is a measure of the probability of simultaneously finding a particle at point $\mathbf{r}$ and $\mathbf{r}'$. This quantity is harder to measure but has been done recently through direct single site imaging of individual atoms [1], or indirectly through noise correlations [2, 3, 4]. Recently, using high resolution imaging techniques the group of Cheng Chin at the University of Chicago has successfully measured shot to shot density fluctuations in a 2D Bose gas [5].

For a homogenous system, at zero temperature, one finds that

$$g^{(2)}_\delta = n_0^2 + 2n_0 n_{ex} + n_0 \sum_{\mathbf{k}} e^{i\mathbf{k}\cdot\delta}\left(2|v_k|^2 + u_k^* v_k + u_k v_k^*\right) \tag{3.8}$$

where $\delta = |\mathbf{r} - \mathbf{r}'|$. In the absence of interactions, $n_{ex} = 0$, and one has $g^{(2)}_\delta = n_0^2$ is a constant, independent of δ. Substituting Eq. 3.6 and normalizing all lengths by

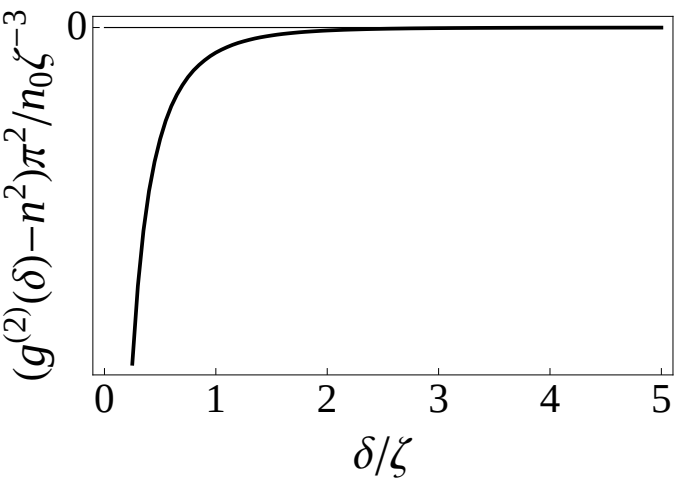

Figure 3.2: **Density-density correlation function** Plot of $g^{(2)}_\delta$ for an interacting gas, obtained by integrating Eq. 3.9 as a function of δ/ζ. At large distance, the gas becomes uncorrelated exponentially with δ, and $g^{(2)}$ reduces to n_0^2. At short distances, $\delta < \zeta$, the density-density correlation function diverges as $1/\delta$. At these short distances one must include the contribution to the correlation function from the non-condensed particles which yields a stronger divergence of $1/\delta^2$. This arises from the divergence in the relative two-particle wave-function interacting with a singular contact interaction [6].

ζ and momenta by k_{MF}, one obtains the equation

$$g^{(2)}_\delta = n^2 + \frac{n_0\zeta^{-3}}{\pi^2\delta}\int_0^\infty x\sin(\sqrt{2}x\delta)\left(\frac{x}{\sqrt{x^2+2}}-1\right) \tag{3.9}$$

where $n^2 \approx n_0^2 + 2n_0n_{ex}$ is the total density.

In Fig 3.2 we plot the density-density correlation function in equilibrium at zero temperature for a particular value of the interaction strength as a function of δ. First note that the density-density correlations are smaller than those for a Bose condensate, owing to the mutual repulsion between the particles. At very short distances the density-density correlation function diverges as $1/\delta$. Here one has to include correlations arising purely between non-condensed particles, which are ignored in this theory. Inclusion of these terms results in an even

stronger divergence of $1/\delta^2$ (with opposite sign), which results from the singular nature of the wave-function of two-particles interacting with a contact interaction. At long distances, $\delta \gg \zeta$, the gas becomes uncorrelated and $g^{(2)} \to n^2$.

The integrand of Eq. 3.9 is another useful quantity, namely the static structure factor: $S(\mathbf{k}) = \int d\mathbf{r} e^{i\mathbf{k}\cdot(\mathbf{r}-\mathbf{r}')} g^{(2)}(\mathbf{r}-\mathbf{r}')$. One finds that $S(\mathbf{k}) = C + n_0(\epsilon_k/E_k - 1)$ where C is a momentum independent constant, proportional to the total density.

For $k \gg k_{MF}$, $S(k) \to C$ as $1/k^2$. The large k behavior of $S(k)$ contains information about the short distance physics of $g^{(2)}$. In particular, this implies that 3D $g^{(2)}(\delta) - n^2 \sim \int dk e^{ik\delta}$ diverges as $1/\delta$ for small δ. In 2D $g^{(2)}(\delta) - n^2 \sim \int dk e^{ik\delta}/k \sim \log(\delta)$ and in 1D, $g^{(2)}(\delta) - n^2 \to 0$.

Similarly, for small $k \ll k_{MF}$, $S(k) \approx C - n_0 + k/k_{MF} + O(k/k_{MF})^2$. Thus one can extract the speed of sound by looking at the slope of $S(k)$ near $k = 0$.

I refer the reader to Ref. [7] for a detailed finite temperature analysis of the density-density correlation functions for a weakly interacting Bose gas.

A third useful quantity to consider is the fluctuations in the phase $\langle \delta\phi_k \delta\phi_{-k} \rangle$ of the condensate wave-function. This quantity is the hardest to measure, but is extremely useful as it contains information about long range order. In Bogoliubov theory one finds that

$$\langle \delta\phi_k \delta\phi_{-k} \rangle = \frac{1}{4n_0^2}\Big(-1 + u_k^* v_k + u_k v_k^* - |v_k|^2 \Big) \tag{3.10}$$

The spatially dependent phase fluctuations are obtained by taking a Fourier transform $\langle \delta\phi(\mathbf{r}) \delta\phi(\mathbf{r}') \rangle = \int d\mathbf{k} e^{i\mathbf{k}\cdot(\mathbf{r}-\mathbf{r}')} \langle \delta\phi_{\mathbf{k}} \delta\phi_{-\mathbf{k}} \rangle$.

For a homogeneous gas in equilibrium at zero temperature one finds

$$\langle \delta\phi_k \delta\phi_{-k} \rangle = -\frac{1}{2n_0^2}\Big(\frac{\epsilon_k + 2gn_0}{E_k} - 1 \Big) \tag{3.11}$$

up to a constant. For large values of $k \gg k_{MF}$, $\langle \delta\phi_k \delta\phi_{-k} \rangle \rightarrow -\frac{1}{2n_0^2 k^2}$, while for small values of k, $\langle \delta\phi_k \delta\phi_{-k} \rangle \rightarrow 1/k$.

Both the density and phase fluctuations have the same ultra-violet behavior but differ at low k in that while density-fluctuations approach a constant, phase fluctuations diverge as $1/k$. In dimensions greater than 1 phase fluctuations are negligible at zero temperature: $\langle \delta\phi(\mathbf{r}) \delta\phi(\mathbf{r}') \rangle \rightarrow 0$ as $|\mathbf{r} - \mathbf{r}'| \rightarrow \infty$. The situation is different in 1 dimension where the integral is infra-red divergent indicating the absence of long range order at zero temperature [8].

The existence of a macroscopic phase in a BEC was demonstrated in a beautiful experiment by Andrews *et al.* who measured the interference pattern resulting from two overlapping Bose-condensates [9]. This technique has been used to study vortices in 2D gases [10] and more recently the absence of thermalization in 1D systems [11].

3.3 Bosons in an optical lattice: Bose Hubbard model

I now turn my attention to the physics of bosons in optical lattices which realize the Bose Hubbard Hamiltonian [12] first developed by Fisher *et al.* [13]:

$$\mathcal{H}_{BH} = -J \sum_{\langle ij \rangle} \left(a_i^\dagger a_j + h.c. \right) + \sum_i \left[\frac{U}{2} n_i (n_i - 1) - \mu_i n_i \right] \tag{3.12}$$

where a_i and $a_i^\dagger$ are bosonic annihilation and creation operators at lattice site i, and $\mu_i = \mu - V_{\text{ex}}(i)$, where μ is the chemical potential and $V_{\text{ex}}(i)$ is the external potential at site i. In Chapter 1, I discussed how one obtains the hopping and on-site interaction energy from the Wannier functions. For typical lattice spacings in ultra-cold gases, second and third nearest neighbor hoppings terms are

significantly smaller and can be ignored.

The basic physics of this model can be studied by considering two limits: (a) $J \gg U$: in this limit, the interactions can be ignored, and the atoms occupy the lowest $k = 0$ momentum state, and as long as the temperature T is much smaller than J, the system becomes a weakly interacting superfluid. In the opposite limit (b) $U \gg J$, the tunneling can be ignored and different sites decouple. The state of the system can then be described as a produce of Fock states with occupation n on each site.

The two limits described here have quite different physics and standard weak coupling mean-field theories or strong coupling expansions work in one regime or the other. Here I describe a mean-field approach which becomes exact in the zero tunneling ($J = 0$) and zero interaction limits ($U = 0$) and serves as an interpolation scheme in between.

3.4 Gutzwiller mean-field theory

For simplicity, we consider a homogeneous gas of bosons in an optical lattice. In this case, $\mu_i = \mu$ a constant, fixed by the total atom number $N = \sum_i \langle a_i^\dagger a_i \rangle$. The starting point of the Gutzwiller mean-field theory is the variational wave-function

$$\Psi = \bigotimes_i \sum_m c_m |m\rangle_i \tag{3.13}$$

where $|m\rangle_i$ is the m-particle Fock state on site i, with real coefficients c_m. The wave-function is readily extended to inhomogeneous systems by making the co-efficients position dependent. Next we decouple the Bose-Hubbard Hamil-

tonian into a sum of single site Hamiltonians coupled by a mean-field

$$\alpha = z\langle a\rangle = z\sum_m \sqrt{m+1}c_{m+1}c_m \tag{3.14}$$

where z is the co-ordination number of the lattice ($z = 2d$ for a hyper-cubic lattice in d dimensions).

The Gutzwiller description is simplistic in that it divides the atoms into $k = 0$ condensed and $k \neq 0$ non-condensed atoms. The number of condensed atoms is $N_c = \sum_i \langle a\rangle^2$.

Solving the Schrodinger equation for this trial wave-function yields the equation:

$$\epsilon c_m^{(i)} = -J\alpha\left(\sqrt{m+1}c_{m+1} + \sqrt{m}c_{m-1}\right) + \left[\frac{U}{2}m(m-1) - \mu m\right]c_m, \tag{3.15}$$

where ϵ is the eigenvalues of the problem .The equation is a non-linear equation in the c_m and is solved by solved at each J/U by truncating Ψ to a reasonably number of states, choosing a trial state, calcuating α and iterating Eq. 3.15 repeatedly until convergence is achieved. Even with a large number of basis states, the convergence is extremely rapid. For small values of J/U, it suffices to make a "particle-hole" approximation by truncating Ψ to three states $n-1, n, n+1$, where n is the average (integer) occupation. In the superfluid limit of large J/U, this approximation is insufficient and a large number of states need to be kept.

In Fig. 3.3 we plot the phase diagram for a 3D cubic lattice as a function of J/U for different values of μ/U. Also shown is the condensate fraction as a function of J/U. The order parameter smoothly approaches 0 indicating a second order quantum phase transition at a critical value of J/U which is μ dependent. The phase boundary can be readily determined by noting that $\alpha = 0$ at this point which is done numerically to obtain Fig. 3.3.

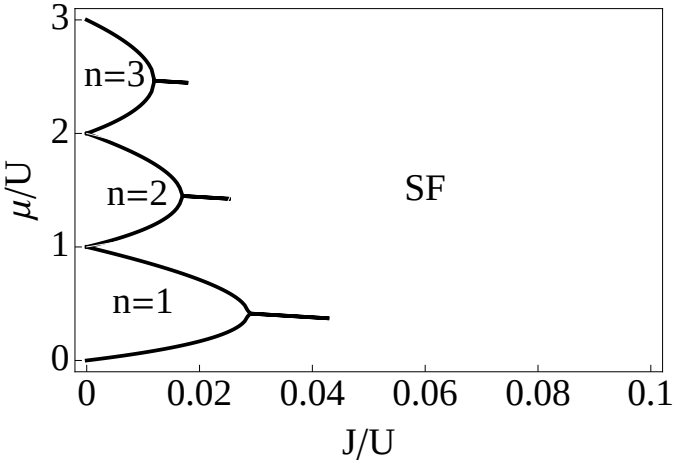

Figure 3.3: **mean-field phase diagram of the Bose-Hubbard model** Mean-field phase diagram for the Bose Hubbard model obtained by iterating Eq. 3.15 for different values of J/U and μ/U at zero temperature. For a critical value of J/U (which is μ dependent) one obtains a phase transition between a superfluid and a Mott insulator. The lines emanating from the tip of the Mott lobes are lines of integer density.

The regions inside the lobes correspond to states with definite quantized value of the density. The density does not vary with chemical potential, therefore the compressibility $\kappa = \partial n/\partial\mu = 0$, and the state is *incompressible*. In other words, it costs energy of order U to add or remove a particle from this state, which we call the Mott gap. The regions outside the lobes correspond to a compressible superfluid where the number of particles fluctuates with chemical potential $\kappa \neq 0$. As a result the phase transition between a superfluid and Mott insulator is accompanied by a discontinuous change in the compressibility κ.

The situation is different along the contours of integer density, shown by the solid lines emerging from the tips of the Mott lobes. Along these contours the value of the density is pinned to the value in the Mott state. Hence at the Mott tip, the density is unchanged even if the chemical potential is varied, implying that $\partial\mu/\partial n \to \infty$, corresponding to a vanishing compressibility at the Mott tips.

The Bose Hubbard model Eq. 3.12 is sign problem free and amenable to Quantum Monte Carlo (QMC) simulations. In 3D, QMC simulations by Capogrosso-Sansone, Prokof'ev and Svistunov find the tip of the $n = 1$ Mott lobe at $U/J = 29.34$, compared to the mean-field prediction of $U/J = 34.9$ [14]. Thus the Gutzwiller mean-field overestimates the superfluid regions of the phase diagram. In lower dimensions, the discrepancy is larger, which is not surprising.

Although the Gutzwiller mean-field theory is only approximate near phase boundaries, a major advantage of this method as I will show in later chapters, is that it is readily extended to studying dynamics. Recently the static single-site Gutzwiller mean field theory described here has been extended to clusters [15]. The agreement with QMC is pretty good for even a smaller number of clusters. One way to view the Gutzwiller mean-field Hamiltonian is as the leading order term in an expansion in $1/z$, the co-ordination number. As the expansion parameter is not the hopping or the interactions, this model allows one to study the entire phase diagram (with reasonable accuracy). Recently this expansion has been carried out to higher order by various groups to derive an effective impurity action, which is then solved using QMC [16, 17].

3.5 Finite-temperature Gutzwiller

The Gutzwiller theory described here is readily extended to finite temperatures by defining a partition function for a single site as $\mathcal{Z} = \sum_{n=0}^{\infty} e^{-\beta E_n}$, where E_n are the eigenvalues of the single site Hamiltonian, which depend on J/U, μ/U and T/U. The average occupation and mean-field have to be determined self-consistently using the relations: $n_0 = 1/\mathcal{Z} \sum_n n e^{-\beta E_n} / \sum_n e^{-\beta E_n}$ and

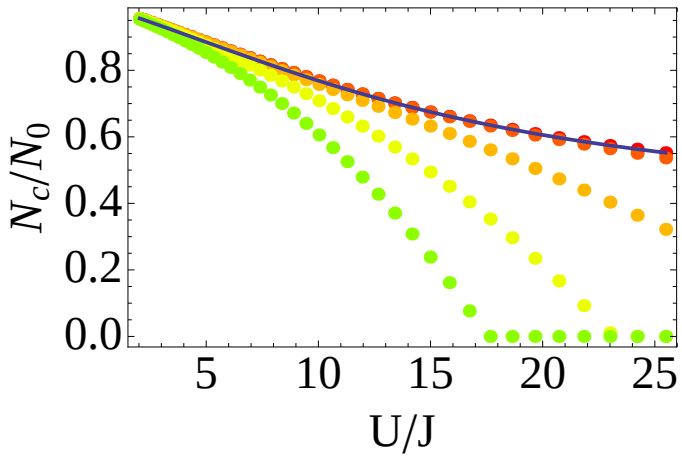

Figure 3.4: **Finite Temperature condensate fraction** Condensate fraction $N_c = |\langle a \rangle|^2$ plotted as a function of U/J for different temperatures. The blue line is the zero temperature result. For higher temperatures (highest temperature shown is $T = 1.6J$ (green), superfluid-normal transition occurs for smaller values of U/J.

$\alpha = 1/\mathcal{Z} \sum_n \alpha_n e^{-\beta E_n}$. In practice one truncates the Hamiltonian to a few sites in order to perform the sums.

In Fig. 3.4 we plot the average value of the mean-field order parameter (normalized to the total atom number) as a function of U/J for different temperatures T/J. The full finite temperature phase diagram of the Bose Hubbard model can be found in [18].

3.6 Dynamics

In this section, I obtain the excitation spectrum of the Bose Hubbard model by linearizing for small perturbations about the Gutzwiller wave-function. Krutitsky and Navez perform a detailed analysis of the excitation spectrum using the Gutzwiller approach in [19]. Here I highlight some important results which will

become useful later.

To obtain the excitation spectrum about the Gutzwiller ground state, we linearize the Gutzwiller wave function as follows: we write

$$c_m^{(i)} = c_m^{eq} + u_{k,m} e^{i(ki-\omega t)} + v_{k,m} e^{-i(ki-\omega t)} \tag{3.16}$$

whre $u_{k,m}$ and $v_{k,m}$ are vectors of size M, which is the number of total states included in the basis. This has the flavor of the Bogoliubov approximation developed for the homogeneous gas in the continuum. However unlike in that case, the u_{km} and v_{km} do not obey any constraints.

Inserting Eq. 3.16 into Eq. 3.15 we obtain the following matrix equation for the u_{km} and v_{km} which have to be solved numerically.

$$\omega_k \begin{pmatrix} u_k \\ v_k \end{pmatrix} = \begin{pmatrix} A_k & B_k \\ -B_k & -A_k \end{pmatrix} \tag{3.17}$$

where we have used the short hand u_k to denote the vector u_{km} and A_k do denote the matrix $A_k^{nn'}$. The matrix elements A_k and B_k take the form

$$\begin{aligned} A_k^{nn'} = -J\alpha\Big(\sqrt{n'}\delta_{n',n+1} + \sqrt{n}\delta_{n,n'+1}\Big) + \Big[\frac{U}{2}n(n-1) - \mu n - \hbar\omega_0\Big]\delta_{n,n'} - \\ J_k\Big[\sqrt{n+1}\,\sqrt{n'+1}c_{n'+1}^{eq}c_{n+1}^{eq} + \sqrt{n}\,\sqrt{n'}c_{n-1}^{eq}c_{n'-1}^{eq}\Big] \end{aligned} \tag{3.18}$$

and

$$B_k^{nn'} = -J_k\Big[\sqrt{n+1}\,\sqrt{n'}c_{n+1}^{eq}c_{n'-1}^{eq} + \sqrt{n}\,\sqrt{n'+1}c_{n-1}^{eq}c_{n'+1}^{eq}\Big] \tag{3.19}$$

where $J_k = zJ\cos(kd)$ where d is the lattice spacing, ω_0 is the energy of the ground state and $\alpha = z\langle a\rangle$ in the ground state.

Since the u_k and v_ks are vectors, these equations need to be solved numerically. However they can be solved analytically deep in the Mott regime where

$\alpha = 0$ and it suffices to only retain a few basis states. Deep in the superfluid, a large number of basis states need to be kept to properly capture the dynamics.

In Figs. 3.5 and 3.6, I plot characteristic spectra deep in the superfluid phase, near the superfluid Mott transition and finally deep in the Mott phase. Typically the number of modes obtained will be twice the number of states kept. However the bulk of the modes are at high energies ($\sim E_R$) and here I only focus on the *two* lowest modes.

3.6.1 Excitation spectra in the Superfluid

Deep in the superfluid limit, the Gutzwiller ground state is one where all the particles condense at the bottom of the band. As a result, the non-linearity of the bandstructure is not very important as there are no particles at the edge of the Brillouin zone. The band structure only changes the effective mass, and one expects Bogoliubov theory to be valid. Indeed as shown in Fig. 3.5, the dispersion obtained from the Gutzwiller approach matches the Bogoliubov dispersion at small k, with the speed of sound given by $c = d\sqrt{2J/\kappa}\alpha/\hbar$ where κ is the compressibility defined as $\kappa = \partial n/\partial\mu$. Since almost all the particles are condensed, $\alpha \approx \sqrt{n}$, and $\kappa \approx 1/U$. Hence $c = \sqrt{2JUn}$ which is precisely the Bogoliubov expression with an effective mass $m^* = \hbar^2/2Jd^2$.

Near the Mott transition, an additional mode appears which is gapped. The gap to this excitation can be calculated very close to the Mott transition where it suffices to retain only 3 states, *i.e* the so called particle-hole approximation. For the $n = 1$ Mott insulator I find, $\Delta = \frac{1}{4}(U + \sqrt{48z^2\langle a\rangle^2 J^2 + U^2})$. The mode has a quadratic dispersion at low k, and hence is particle-hole like in character. Deep

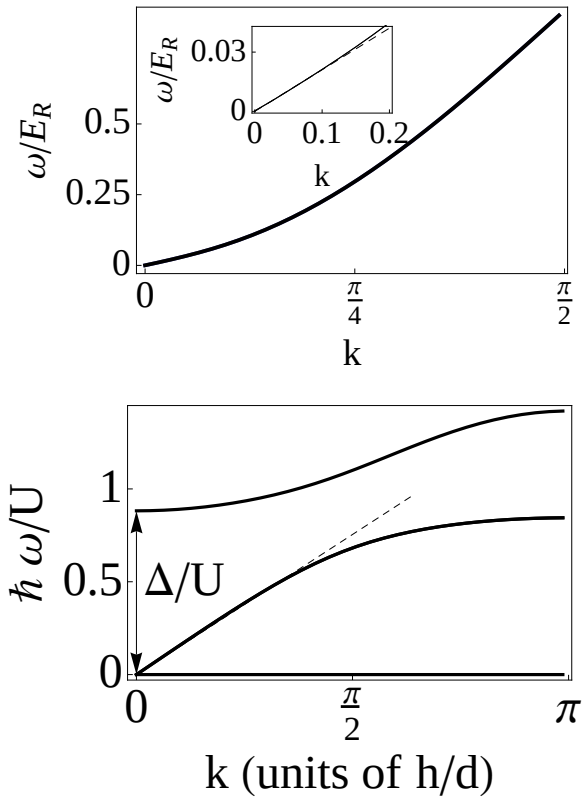

Figure 3.5: **Charcteristic Excitation Spectra in the Superfluid phase in 3D** (Top) Deep in the superfluid, the excitations are Bogoliubov like. The inset shows that the spectrum is indeed linear at low k. The dashed line is $\omega = ck$ with c given by Bogoliubov theory. (Bottom) Near the superfluid Mott boundary, an additional gapped mode is present. The gap is of order $U/2$ for $J/U \ll 1$. The phonon mode is also present but the sound velocity smoothly vanishes as the Mott transition is approached.

in the superfluid this mode gets pushed up to high energies and eventually the gap becomes comparable to the recoil energy. The phonon-like excitation remains and Bogoliubov theory still captures the speed of sound well, even in deep lattices.

3.6.2 Excitation spectra at the Superfluid-Mott boundary

At the Mott-superfluid boundary, the phonon sound speed smoothly approaches 0, and the gapped excitation remains gapped. The vanishing of the sound speed can be understood simply from the fact that the superfluid order parameter α smoothly goes to zero as the Mott transition is approached. Meanwhile the gas still has a finite compressibility. As a result, $c \to 0$ at the Mott boundary.

The behavior is *qualitatively* different at the tip of the Mott lobes where phase transition occurs at fixed density, hence the compressibility also vanishes such that α/κ stays finite. As a result the sound speed remains finite as the phase transition is crossed. The gapped mode becomes degenerate with the phonon at low k.

3.6.3 Excitation spectra in the Mott Phase

In the Mott phase one finds two modes, both of which are gapped, corresponding to the energy required to create a particle and a hole. If the chemical potential is chosen such that one has particle-hole symmetry, then the two modes are degenerate. As $J \to 0$, the gap to these excitations becomes $\Delta = U/2$. This occurs at the tip of the Mott lobes. In Chapter 6, we will show that the existence of this Mott gap has important implications for timescales for dynamics in inhomogeneous systems.

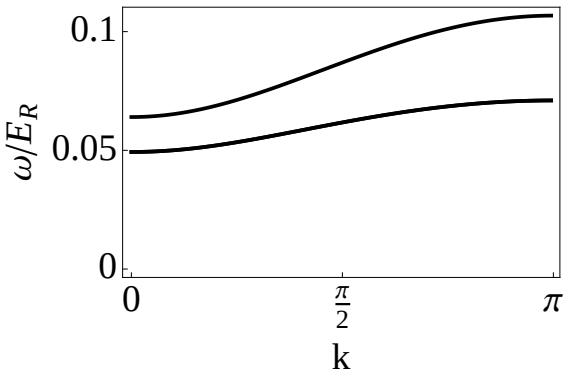

Figure 3.6: **Charcteristic Excitation Spectra in the Mott phase in** 3**D** (Top) In the Mott phase, the excitations are gapped and have quadratic dispersion at low k. Generically, particle-hole symmetry is absent and one obtains two distinct modes, corresponding to the energy required to create a particle or a hole on top of the Mott insulating background.

3.7 Low energy physics near the supefluid Mott boundary

I now discuss the low energy physics near the superfluid-Mott boundary using a Ginzburg Landau theory. The discussion in this section will closely follow Chapters 10 and 11 in the textbook *Quantum Phase Transitions* by Sachdev [20]. I start by writing down the partition function for the Bose Hubbard model

$$\mathcal{Z}_B = Tre^{-\beta\mathcal{H}_{BH}} = \int \mathcal{D}b_i(\tau)\mathcal{D}b_i^*(\tau)e^{-\int_0^\beta d\tau\mathcal{L}_{BH}} \tag{3.20}$$

where the Lagrangian $\mathcal{L}$ is

$$\mathcal{L}_{BH} = \sum_i \left(b_i(\tau)\frac{\partial b_i(\tau)}{\partial\tau} - \mu b_i^* b_i + \frac{U}{2}b_i^* b_i^* b_i b_i\right) - J\sum_{\langle ij\rangle}(b_i^* b_j + b_j^* b_i) \tag{3.21}$$

We now decouple the hopping term by defining an auxillary field $\Psi_{Bi}(\tau)$ and using the following identity for Gaussian integrals

$$\int \mathcal{D}x_i^*\mathcal{D}x_i^* e^{-x_i^* H_{ij}x_j + J_i^* x_i + J_i x_i^*} = det[H]^{-1}e^{J_i^* H_{ij}^{-1}J_j} \tag{3.22}$$

which is sometimes known as a Hubbard-Stratonivich transformation. Doing so, one gets:

$$\mathcal{Z}_B = \int \mathcal{D}b_i(\tau)\mathcal{D}b_i^*(\tau)\mathcal{D}\Psi_{Bi}(\tau)\mathcal{D}\Psi_{Bi}^*(\tau)e^{-\int_0^\beta d\tau\mathcal{L}} \tag{3.23}$$

where the new Lagrangian is:

$$\mathcal{L} = \sum_i \left(b_i(\tau)\frac{\partial b_i(\tau)}{\partial\tau} - \mu b_i^* b_i + \frac{U}{2}b_i^* b_i^* b_i b_i - \Psi_{Bi}b_i^* - \Psi_{Bi}^* b_i\right) + \sum_{i,j}\Psi_{Bi}^* J_{ij}^{-1}\Psi_{Bj} \tag{3.24}$$

where we have generalized the hopping term to a matrix $J_{ij} = J$ if i, j are nearest neighbors and 0 otherwise.

Next we expand $\mathcal{L}$ in powers of Ψ_B, by integrating out the b_i fields. This can be done exactly as the Ψ independent part of $\mathcal{L}$ is a sum of single site Hamiltonians for the b_is, which can be diagonalized exactly. Re-exponentiating the resulting Taylor series and expressing the terms in terms of spatial and temporal gradients of the fields Ψ we obtain the following Ginzburg Landau theory for the auxiliary fields

$$\mathcal{L}_B = K_1\Psi_B\frac{\partial\Psi_B}{\partial\tau} + K_2|\frac{\partial\Psi_B}{\partial\tau}|^2 + K_3|\partial\Psi_B|^2 + r|\Psi_B|^2 + \frac{u}{2}|\Psi_B|^4 \tag{3.25}$$

where the detailed expressions for the co-efficients are provided in Appendix D. For now we only concentrate on the qualitative information contained in this action.

First consider the static part of the action. This has the form of a standard Ginzburg Landau action with a spatial derivative term, and a quadratic and quartic term. In the homogeneous limit, where the spatial derivative can be ignored, the action has a trivial solution corresponding to $\Psi_B = 0$ and a non-trivial one where $\Psi_B = \sqrt{-2r/u}$. Thus the mean-field critical point occurs when $r = 0$.

Next note that when $K_1 \neq 0$, one can ignore the K_2 term as it has two time derivatives. In this case, we obtain the standard Gross Pitaevskii action for a Bose-Einstein condensate. Notice that when K_2 is ignored, we have one time derivative and two spatial derivatives in the action. This implies a quadratic dispersion $\omega \sim k^2$, which is consistent with the vanishing sound velocity near the Mott boundary from the Gutzwiller approach.

The physics is different if the K_1 term is identically zero, which occurs at the Mott lobe (see Appendix D). In this case, the K_2 term must be retained in the action and one finds a linear dispersion $\omega \sim k$, as I obtained earlier using the Gutzwiller technique.

The phase transition between the superfluid and Mott insulator can be classified into two separate universality classes, with different critical exponents depending on whether K_1 is zero or non-zero. For $K_1 \neq 0$, the action is identical to a dilute Bose gas. Using high resolution imaging tecnhniques, experimentalists at Chicago were able to exctact the critical exponents for this theory by measuring the equation of state of the dilute Bose gas [18, 21].

When K_1 is zero, the resulting action is identical to that of a quantum rotor or a classical XY model. Experimentally the properties of this transition are harder to extract as cold atomic systems are inhomogeneous and the number of atoms near the Mott tip are typically very small. Nonetheless, measuring the excitation spectrum near this critical point has attracted a lot of attention recently [22, 23].

BIBLIOGRAPHY

[1] M. Cheneau, P. Barmettler, D. Poletti, M. Endres, P. Schaub, T. Fukuhara, C. Gross, I. Bloch, C. Kollath and S. Kuhr, Nature **481** 484 (2012).

[2] S. Fölling, F. Gerbier, A. Widera, O. Mandel, T. Gericke and I. Bloch, Nature **434** 481-484 (2005).

[3] E. Altman, E. Demler and M. D. Lukin, Phys. Rev A **70** 013603 (2004)

[4] M. Greiner, C. A. Regal J. T. Stewart and D. S. Jin Phys. Rev. Lett. **94** 110401 (2005).

[5] C-L. Hung, X. Zhang, L-C. Ha, S-K. Tung, N. Gemelke and C. Chin, New Journal of Physics, **13** 075019 (2011).

[6] T. D. Lee, K. Huang and C. N. Yang, Phys. Rev. **106** 1135 (1957).

[7] M. Naraschewski and R. J. Glauber, Phys. Rev. A **59** 4595 (1999).

[8] N. D. Mermin and H. Wagner, Phys. Rev. Lett. **17** 1133 (1966).

[9] M. R. Andrews, C. G. Townsend, H.-J. Miesner, D. S. Durfee, D. M. Kurn and W. Ketterle, Science **275** 637-641 (1997).

[10] Z. Hadzibabic, P. Kruger, M. Cheneau, B. Battelier and J. Dalibard, Nature **441** 1118-1121 (2006).

[11] S. Hofferberth, I. Lesanovsky, B. Fischer, T. Schumm and J. Schmiedmayer, Nature **449** 324-327 (2007).

[12] D. Jaksch, C. Bruder, J. I. Cirac, C. W. Gardiner and P. Zoller, Phys. Rev. Lett. **81** 3108, (1998).

[13] M. Fisher, P. B. Weichman, G. Grinstein and D. S. Fisher, Phys. Rev. B **40** 546-570 (1989).

[14] B. Capogrosso-Sansone, N.V.Prokof'ev, and B. Svistunov, Phys. Rev. B **75**, 134302 (2007).

[15] T. McIntosh, P. Pisarski, R. J. Gooding and E. Zaremba arXiv:1111.4102 (2011).

[16] A. Hubener, M. Snoek and W. Hofstetter, Phys. Rev. B **80** 245109 (2009).

[17] P. Anders, E. Gull, L. Pollet, M. Troyer and P. Werner, Phys. Rev. Lett. **105** 096402 (2010).

[18] K. R. A. Hazzard and E. J. Mueller, Phys. Rev. A **84** 013604 (2011).

[19] K. V. Krutitsky and P. Navez, Phys. Rev. A **84** 033602 (2011).

[20] S. Sachdev, *Quantum Phase Transitions*, Cambridge University Press, Cambridge 2001.

[21] X. Zhang, C-L. Hung, S-K. Tung and C. Chin, Science **335** 1070 (2012).

[22] M. Endres, T. Fukuhara, D. Pekker, M. Cheneau, P. Schaub, C. Gross, E. Demler, S. Kuhr and I. Bloch Nature **487** 454 (2012).

[23] L. Pollet and N. V. Prokof'ev eprint.arXiv: 1204.5190.

CHAPTER 4

DYNAMICS OF CORRELATIONS IN A DILUTE BOSE GAS FOLLOWING AN INTERACTION QUENCH

This Chapter was adapted from "Dynamics of correlations in a dilute Bose gas following an interaction quench", by Stefan S. Natu and Erich J. Mueller, which is currently under review for publication in Physical Review A. What can we learn by forcing a cold gas out of equilibrium? In this Chapter, I explore some of the consequences that result from such a procedure

In Chapter 3, I discussed the static properties of a weakly interacting Bose gas and introduced the Bogoliubov approximation. In this chapter I calculate the dynamics of the one and two body correlation functions in a homogeneous Bose gas at zero temperature following a sudden change in the interaction strength, with and without an underlying lattice. My main focus will be threefold: First I wish to simply elucidate the timescales for dynamics in this simple, interacting, many-body system. Secondly, I relate the long and short time features in the correlation functions to the underlying *known* excitation spectrum. As I show in this Chapter, my calculations suggest that the dynamics of correlations may be useful in extracting many body parameters such as the phonon velocity. Finally, as many of the strongly interacting models are lattice models, I wish to understand the features in the correlation functions produced by the lattice separately from those produced by interactions.

Throughout, I focus on conceptually simple examples that cleanly highlight the features in the correlation functions arising separately from interactions and band structure. In the continuum, I show that the Bogoliubov spectrum leads to a diffusive evolution of density correlations for short times, and ballistic at long

times. In the lattice I find that the correlation functions develop additional oscillations. Moreover, the lattice dispersion induces an additional velocity scale, and some features instead propagate with that velocity. Finally, I discuss the time-evolution of a generalization of the Tan contact following a quench. These predictions can be readily tested in experiments and serve to benchmark the dynamics of more complicated systems.

4.1 Introduction

New higher resolution imaging techniques are allowing cold atom experiments to probe spatial correlation functions [3, 2]. Recently, the focus has turned to the dynamics of these correlations following a sudden change in experimental parameters such as lattice or trap depth or interaction strength [3, 4, 5, 6, 7, 8, 9]. In many ways, experiments are ahead of theory, as the very paradigms for thinking of these highly nonequilibrium experiments are just being developed [10, 11, 12, 13]. Here I use the time dependent Bogoliubov approximation to study quenches in a weakly interacting Bose gas. I am thereby able to organize the phenomena, for example separating out interaction effects from lattice effects. Although experiments to date have been in a strong or intermediate coupling regime and cannot be directly modeled by my technique, the existing data appears to be consistent with these organizational principles.

There are a number of fundamental issues which can be probed through the time dependence of correlation functions. For example, studies of lattice models have found that the manner in which correlations develop following a quench is directly related to questions of causality [7, 10, 11, 13, 14, 15, 17, 18]. This has important implications for understanding how quantum systems approach

equilibrium and the timescales involved. Another key issue probed by these studies is the nature of the final state obtained at long times following such a quench, and the degree of short or long range order [12, 13, 19, 20, 21, 22, 23]. Here I explore how the underlying dispersion influences the spatio-temporal characteristics of the correlation functions.

Typically the time-evolution of correlation functions can be quite complicated [5, 7, 15] and non-intuitive. My aim in this chapter is to organize the salient features in the density-density correlation function for a weakly interacting Bose gas, whose static properties are textbook knowledge for atomic physicists [24, 25, 26, 27]. Using time dependent Bogoliubov theory, I calculate how the correlation functions evolve following a sudden change in the interaction strength. I find that in free space the density correlations spread diffusively at short times, crossing over to ballistic at long times. The speed of propagation is the phonon velocity. Furthermore, the decay of the correlation functions at long times is strongly influenced by the underlying dispersion.

As many of the strongly correlated models are lattice models, separating the role of the lattice from that of the interactions is crucial. I find that in the lattice, new features appear which propagate with a speed determined by the bandwidth. The speed of propagation crosses over to the sound speed at long times.

In addition to "long wavelength" physics, I find that the short length-scale behavior of the correlation functions has interesting structure. Immediately following the quench, the two-particle correlation function develops a divergence which scales as $1/|\mathbf{r} - \mathbf{r}'|^2$. This structure is due to the singular nature of the two-particle relative wave function at short distances [24]. In equilibrium, this

singularity has attracted a lot of attention recently following the work of Tan, who was able to relate the short distance structure of the two-particle correlation function in a two-component Fermi gas to the internal energy via a quantity called the "contact" [28, 29, 30, 31]. Here I study the dynamics of the contact (and its generalizations) following a quench.

This Chapter is organized as follows: In Sec. II we describe our system, derive in detail the equations of motion governing the dynamics of the correlation functions in the presence and absence of a lattice, and discuss the regimes of validity of our results. In Secs. III and IV, we focus on the dynamics of correlations in the continuum. To highlight the role of interactions, we study two types of quenches: a sudden quench from a non-interacting system to an interacting gas and the reverse quench. In the former the system evolves with a Bogoliubov dispersion while in the latter case, the dispersion is free. In Sec V. we discuss the lattice and compare and contrast the lattice from the continuum. In Sec VI., we discuss the short-range physics in the two-particle correlation functions, and relate our results to the contact. In Sec. VII, we summarize our results. Throughout this paper, we limit our discussion to sudden quenches at time $t = 0$ between different initial and final states.

4.2 Model

I start with the Hamiltonian for Bose gas interacting with a contact interaction:

$$\mathcal{H} = \sum_k \left(\epsilon_k - \mu\right) a_k^\dagger a_k + \frac{g}{2\Omega} \sum_{pqk} a_{p+q/2}^\dagger a_{k-q/2}^\dagger a_k a_p \tag{4.1}$$

where $g > 0$ parametrizes the interactions, Ω is the volume, and a_k is the bosonic annhilation operator. In three-dimensional free space, $g = 4\pi a\hbar^2/m$, where a

is the s-wave scattering length. In a lattice, $g = Ud^D$, where U is the on-site interaction energy, D is the dimension of space and d is the lattice spacing. In free space, the dispersion $\epsilon(k) = \frac{\hbar^2 k^2}{2m}$, while in a lattice $\epsilon(k) = -2J\cos(kd)$, where J is the bandwidth and d is the lattice spacing. In the former case, the sum is over all momenta while in the latter it is restricted to the first Brillouin zone.

First, I study the effects of interactions on the dynamics of correlations in a 3D continuum system. Later I will highlight the differences between the lattice and continuum by considering a 1D system in the presence and absence of a lattice potential. The latter choice is motivated by experiments.

Working in the Heisenberg representation, I now derive the equations of motion that we study in the rest of the paper. At time $t \leq 0$, the system is assumed to be in equilibrium at zero temperature with $g = g_i$. At time $t > 0$, the interactions are constant with $g = g_f$. We now present two approaches for deriving the equations for the correlation functions.

4.2.1 Time-dependent Bogoliubov approximation

In 3D, for weak interactions $na^3 \ll 1$ (where n is the total density), the properties of Eq. 4.1 are well described by a Bogoliubov variational ansatz, where one sets the density of condensed atoms $n_0 = \langle a_{k=0}\rangle^2$ and writes

$$a_{k\neq 0}(t) = u_k(t)b_k + v_k^*(t)b_{-k}^\dagger \tag{4.2}$$

where b_k denotes the bosonic annihilation operator for the non-condensed atoms and has no time dependence and is formally treated as small. I choose b_k operators such that $b_k|\psi_0)\rangle = 0$ where ψ_0 is the initial state (with interaction g_i).

Substituting Eq. 4.2 into Eq. 4.1, and discarding all terms cubic or higher order in the b_ks, following standard arguments I obtain:

$$u_k(t=0) = \sqrt{\frac{1}{2}\left(1 + \frac{\epsilon_k + g_i n_0}{E_k^i}\right)} \qquad (4.3)$$
$$v_k(t=0) = -\sqrt{\frac{1}{2}\left(\frac{\epsilon_k + g_i n_0}{E_k^i} - 1\right)}$$

where $E_k^i = \sqrt{\epsilon_k(\epsilon_k + 2g_i n_0)}$. At future times these coherence factors $u_k(t)$ and $v_k(t)$ will evolve, acquiring complex values, but will always satisfy $|u_k(t)|^2 - |v_k(t)|^2 = 1$. I work in the regime where one can neglect the time dependence of n_0.

The equations of motion for the u_k and v_ks are obtained from the Heisenberg equations of motion for a_k. These equations are linear and can be readily integrated to give:

$$\begin{pmatrix} u_k(t) \\ v_k(t) \end{pmatrix} = \left[\cos(E_k^f t)\hat{I} - i\frac{\sin(E_k^f t)}{E_k^f}\begin{pmatrix} \epsilon_k + g_f n_0 & g_f n_0 \\ -g_f n_0 & -(\epsilon_k + g_f n_0) \end{pmatrix}\right]\begin{pmatrix} u_k(0) \\ v_k(0) \end{pmatrix} \qquad (4.4)$$

where $E_k^f = \sqrt{\epsilon(k)(\epsilon(k) + 2g_f n_0)}$ is the Bogoliubov dispersion where $\epsilon_k = \hbar^2 k^2/2m$.

4.2.2 Expressions for Correlation functions

Here I am interested in the dynamics of two correlation functions: the non-condensed fraction ($n_{ex} = \sum_{\mathbf{k}\neq\mathbf{0}}\langle a_k^\dagger a_k\rangle$), and the *equal time* density-density correlation function $g^{(2)}(\mathbf{r}-\mathbf{r}')(t) = \sum_{\mathbf{q}} e^{i\mathbf{q}\cdot(\mathbf{r}-\mathbf{r}')}\langle\rho_{\mathbf{q}}(t)\rho_{-\mathbf{q}}(t)\rangle$ where $\rho_{\mathbf{q}}(t) = \sum_{\mathbf{k}} a^\dagger_{\mathbf{k}+\mathbf{q}}(t)a_{\mathbf{k}}(t)$. The former is readily measured in time-of-flight experiments [6], while the latter is probed using Bragg spectroscopy [4, 29, 32], noise correlations [33, 34] or by direct in-situ measurements [5, 7]. At zero temperature,

$$n_{ex}(t) = \sum_{\mathbf{k}} |v_k(t)|^2 \qquad (4.5)$$

The approximation of neglecting the time-dependence of n_0 is valid only as long as $n_{ex} \ll n$ for all times. The density correlations are

$$g^{(2)}_{\delta}(t) = n^2 + n \sum_{\mathbf{k}} e^{i\mathbf{k}\cdot\delta}\Big(2|v_k(t)|^2 + u^*_k(t)v_k(t) + u_k(t)v^*_k(t)\Big) + \tilde{g}^{(2)}_{\delta} \tag{4.6}$$

where $\delta = |\mathbf{r} - \mathbf{r}'|$.

The term $\tilde{g}^{(2)}_{\delta}$ is quartic in the u_ks and v_ks and arises from correlations between the non-condensed atoms. These correlations become important only at extremely short distances $\delta \sim a \sim 50$nm, which is roughly 20 times smaller than the typical condensate healing length $\zeta = \hbar/\sqrt{mgn} \sim \mu$m. As I am primarily concerned with $\delta \geq \zeta$, I will ignore corrections to the dynamics arising from this term, except in Section V.

Computing the cubic and quartic terms in Eq. 4.1, after renormalizing the interactions to control an ultra-violet divergence, one finds that this expectation value is small as long as $n_{ex} \ll n$.

4.2.3 Number-phase formulation

The time-dependent Bogoliubov approximation is predicated upon on the depletion being small $n_{ex} \ll n$. This inequality is dramatically violated in $1D$, where $n_{ex} = n$. Following Shevshenko [35], I now reformulate the time dependent Bogoliubov approximation in terms of number and phase variables formally writing $\psi(r) = \sum_k e^{ik\cdot r} a_k = e^{i\phi}\sqrt{\rho}$. To the extent that the hermitian operators ρ and ϕ are well defined, they obey the commutation relations

$[\rho(r), \rho(r')] = [\phi(r), \phi(r')] = 0$ and $[\rho(r), \phi(r')] = i\delta(r - r')$. The breakdown of the Bogoliubov theory in 1D can then be understood as a consequence of the fact that the phase fluctuations between points r and r' diverge, $\langle(\phi(r) - \phi(r'))^2\rangle \to \infty$, as $|r - r'| \to \infty$. Despite this divergence, the gradients of ϕ remain small if the interactions are weak.

The analog of the Bogoliubov approximation thus becomes an expansion in $\nabla\phi$ and the deviation $\delta\rho = \rho - n$, where n is the c-number density. Formally, one introduces Bogoliubov operators via

$$\frac{\delta\rho_k}{\sqrt{n}} = (u_k + v_k)b_k + (u_k^* + v_k^*)b_{-k}^\dagger \tag{4.7}$$

$$2i\sqrt{n}\phi_k = (u_k - v_k)b_k - (u_k^* - v_k^*)b_{-k}^\dagger. \tag{4.8}$$

The equations of motion for u_k and v_k will again yield Eq. 4.4, but with n_0 replaced by n. By construction, the density-density correlators are again given by Eq. 4.6, but now the quartic term is formally zero. Thus Eq. 4.7 does not capture the ultraviolet structure investigated in section V.

Before proceeding to deriving the equations of motion, it is useful to explore in a little more detail how Eqs. 4.7 and 4.8 resolve the divergences of Bogoliubov theory in 1D. Taking the equilibrium coherence factors in Eq. 4.3, one sees that as $k \to 0$, the two relevant combinations scale as $u_k + v_k \sim k^{1/2}$ and $u_k - v_k \sim k^{-1/2}$. Thus the amplitude of the density fluctuations vanish as $k \to 0$, but the amplitude of the phase fluctuations diverge. In 3D the phase space for these fluctuations is sufficiently small that this divergence is unimportant. In 1D, however, they eliminate all long range phase order. Phase gradients (governed by $k\phi_k$), are well behaved as $k \to 0$. This latter feature will be essential for deriving the formalism.

Finally one can calculate the the condensate fraction by looking at the long distance properties of the single particle density matrix,

$$g_1(r,r') = \langle \psi^\dagger(r)\psi(r')\rangle = \langle \sqrt{\rho(r)}e^{i(\phi(r')-\phi(r))}\sqrt{\rho(r')}\rangle, \tag{4.9}$$

which can be expressed in terms of Bogoliubov operators using Eqs. 4.7 and 4.8. In 3D one can expand the resulting expression to quadratic order in the b's, recovering $\lim_{|r-r'|\to\infty} g_1^{(3D)}(r,r') \to n - \sum_k |v_k|^2$. In 1D the phase fluctuations diverge, and $g_1^{(1D)}(r,r') \to 0$ as $|r-r'| \to \infty$.

Having established that the number-phase representation has the right structure to generalize the Bogoliubov results, I now sketch the formal derivation of Eq. 4.4. Specializing to the free-space case, the Hamiltonian is

$$H = \int dr \, \frac{\sqrt{\rho}|\nabla\phi|^2\sqrt{\rho}}{2m} + \frac{|\nabla\rho|^2}{8m\rho} - \mu\rho + \frac{g}{2}\rho^2. \tag{4.10}$$

We substitute Eqs. 4.7 and 4.8, and take the b_k's to be small. Truncating to quadratic order in these operators gives exactly the traditional Bogoliubov expression, but with n_0 replaced by n. Our derivation of Eq. 4.4 then goes through as before.

As with Sec. II B, one again asks whether the expectation value of the neglected terms are small. Focussing on the infrared behavior, one deduces from dimensional analysis that the relevant dimensionless parameter controlling the expansion is $\gamma = (mg/\hbar^2)n^{1-2/D}$. Thus in 1D my approximation works best at high density, while in 3D it works best at low density [36].

The first term in Eq. 4.6 is roughly equal to n^2 where $n = n_0 + n_{ex}$ is the total density. The second term denotes correlations between the condensed and non-condensed atoms. In a non-interacting gas at zero temperature, $u_k = 1$ and $v_k = 0$, therefore $n_{ex} = 0$ and $g_\delta^{(2)} = n_0^2$, independent of δ.

4.2.4 Regimes of validity

The static properties of the two-particle correlation function at zero and finite temperature have been extensively studied by Naraschewski and Glauber [25]. Here I consider quenches at $T = 0$, where the only length scale in the problem is the coherence length of the condensate ζ. Finite temperature introduces another length scale namely the thermal deBroglie wave-length $\lambda_{th} = \hbar/\sqrt{mk_BT}$. At very low temperatures, the mean separation between particles is on the order of ζ, and the physics is interaction dominated. At high temperatures, the mean separation between the particles is set by λ_{th} and interactions play a minor role in the properties of the gas. I expect my results to be valid as long as $T \ll \mu$. The dynamics of correlation functions at finite temperatures is an important direction for further study.

I also emphasize at the outset that the Bogoliubov approximation *collisionless*, and as such only capable of describing the initial stages of dynamics of an interacting gas. Although correlations approach steady state values within this framework at long times, the final state need not be thermal. A more sophisticated theory of equilibration would take into account "collisions" between the Bogoliubov quasi-particles (Landau damping), which is beyond the scope of this work [37].

4.3 Non-condensed fraction in the 3D continuum

Prior to discussing the density-density correlation function, it is instrucive to consider a simpler quantity: the non-condensed fraction. (This is simply re-

lated to the condensate fraction: $n_0 = N - n_{ex}$, which is readily measured in time-of-flight experiments). The dynamics of this quantity following a quench will illustrate the timescales involved in reaching a steady state for a weakly interacting Bose gas. Perhaps not surprisingly, this timescale is determined by $\tau_{mf} = \hbar/g_f n$, the mean-field time in the final state after the quench.

4.3.1 Quench from $g_i = 0$ to $g_f > 0$

The conceptually simplest case is to consider a quench from $g = 0$ to some final $g > 0$. From Eq. 4.4, I find that $v_k(t) = -ign \sin(E_k t)/E_k$, thus $n_{ex} = \sum_{\mathbf{k}} |v_k|^2 = (gn)^2 \sum_{\mathbf{k}} \sin(E_k t)^2/E_k^2$. At long times, the sum is dominated by small values of k, where the dispersion is linear $E_k = ck$, where $c = \sqrt{2gn/m}$ is the speed of sound. With this substitution, the sum is readily performed to yield the expression:

$$n_{ex}(t) = \frac{1}{4\pi}\zeta^{-3}(1 - e^{-4t/\tau_{MF}}) \tag{4.11}$$

where $\zeta = \hbar/\sqrt{mgn}$ is the healing length of the condensate and $\tau_{MF} = \hbar/gn$ is the characteristic relaxation time following the quench. Therefore the population of non-condensed particles grows linearly at short times, saturating on timescales $t \sim \tau_{MF}$. At long times, the number of excitations created is *larger* than the predicted zero temperature equilibrium value $n_{ex,eq} = \zeta^{-3}/6\pi^2$. Associating the energy of the final state with a temperature $T \sim gn$, the number of excitations created is somewhat smaller than the corresponding equilibrium finite temperature value of $n_{ex} \sim \zeta^{-3}/\pi^2$.

Although the dynamics in this case is rather simple, the physics behind it is quite interesting. Within the collisionless Bogoliubov approximation, the number of particles at each momentum k must be conserved ($\langle a_k^\dagger a_k \rangle$). As a result the

dynamics here represents a *collective* oscillation of particles in and out of the condensate with different wave-vectors k. The exponential decay of the condensate fraction is due to a dephasing of these collective oscillations [38].

4.3.2 Quench from $g_i > 0$ to $g_f > 0$

Next, I consider a quench from some initial interaction strength g_i to a final value g_f. Unlike the previous case, there are now two timescales in the problem: $\tau_{i/f} = \hbar/g_{i/f}n$. The dynamics of the non-condensed fraction depends on both these times.

Upon evaluating Eq. 4.4 I find:

$$n_{ex}(t) = \sum_k |v_k(0)|^2 - g_f(g_i - g_f)n^2 \frac{\epsilon(k)\sin(E_k t)^2}{E_k^3} \tag{4.12}$$

The first term in this expression is the number of excitations present in the system initially. The minus sign in front of the second term indicates that if $g_i > g_f$, the number of non-condensed particles decreases over time, and vice-versa if $g_i < g_f$. Alternatively, the condensate fraction grows if $g_i > g_f$ and reduces if $g_i < g_f$.

The number of *new* excitations created/destroyed is thus proportional to $g_f \times (g_i - g_f)$. If $g_f = 0$, then this term is identically zero and no more excitations are created or lost. The initially quantum depleted superfluid remains depleted, unless interactions can redistribute momentum.

To obtain the relevant timescale governing the redistribution of momentum, I evaluate the expression for n_{ex} assuming a linear dispersion. Defining $\zeta = \hbar/\sqrt{mg_i n}$ as the healing length of the initial state, I obtain:

$$n_{ex}(t) = \frac{1}{3\pi^2}\zeta^{-3}\Big(1 - 3\pi\tilde{g}_f(1-\tilde{g}_f)t/\sqrt{\tau_i\tau_f} \Big[I_0(4t/\tau_f) - L_0(4t/\tau_f)\Big]\Big) \tag{4.13}$$

where $\tilde{g}_f = g_f/g_i$, and I_0 and L_0 denote the Bessel function of the second kind and the modified Struve function respectively. For small arguments, $I_0(x) - L_0(x) \approx 1 - 2x/\pi + O(x^2)$, while for $x \gg 1$, $I_0(x) - L_0(x) \approx 2/\pi x + O(x^{-3})$.

Unlike the case of a quench from zero interactions, where τ_{MF} was the only relevant timescale, the dynamics here are governed by *two* timescales: at short times, the number of excitations decreases linearly in time with a timescale given by the geometric mean of the initial and final interaction strengths. At long times $t > \tau_f$, the number of excitations created/destroyed saturates to a constant. Notice also that unlike the case for a quench from zero interactions, the excited fraction saturates *algebraically* rather than exponentially.

In Fig. 4.1, I plot the excited fraction using Eq. 4.13. and also by numerically integrating Eq. 4.12 assuming the full Bogoliubov dispersion. The formula in Eq. 4.13 indeed captures all the relevant features seen in the dynamics.

Again the number of excitations present at long times after the quench is always greater than the number of excitations in the equilibrium final state at zero temperature. Given that the Bogoliubov approximation is collisionless, there is no reason to expect the

To summarize, the long time dynamics of the condensate fraction following a quench is governed by the mean-field time of the final state. At short times however there is considerable redistribution of particles into/out of the condensate due to interactions, on a timescale that depends on the initial and

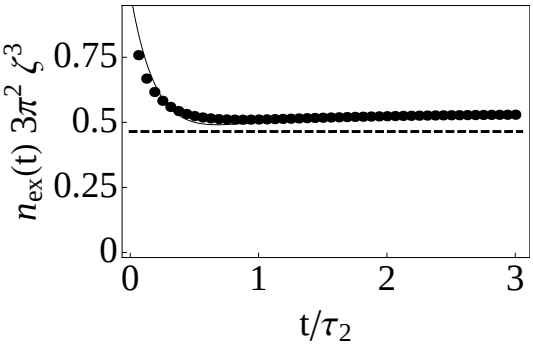

Figure 4.1: **Quasi-momentum redistribution in 3D following a sudden change in interactions:** Plotted is the fraction of non-condensed atoms normalized to the initial excitation fraction following a sudden quench to weaker interactions $g_f/g_i = 0.6$. The excitation density is expressed in terms of ζ, the healing length of the initial condensate. Note that the analytic formula Eq. 4.13 (solid curve) captures the dynamics very well, particularly the long time limit. The characteristic relaxation time is set by $\tau_f = \hbar/g_f n$, the mean-field time of the final state. The dashed curve is the excitation fraction at the final interaction strength in equilibrium.

final interaction strength. In all cases, the final state has more excitations than the corresponding zero temperature equilibrium state. The deviations from the equilibrium zero temperature state for weak interactions are small, typically on the order of $O(na^3)$.

4.4 Two-particle correlations in the continuum

I now turn to the dynamics of the two-particle correlation function, which will be my focus for the rest of this Chapter. In this section, I study two types of quenches in the continuum: a quench from zero interactions to an interacting gas and vice versa. My goal is to highlight the role of the Bogoliubov dispersion in determining the features observed in the density-density correlation function.

4.4.1 Short time dynamics: Diffusive to ballistic crossover

Consider the evolution of $g_\delta^{(2)}$ following a sudden quench from $g = 0$ to $g = g_f > 0$. At $t = 0$, $u_k = 1$ and $v_k = 0$, and neglecting the quartic term $\tilde{g}_\delta^{(2)}$, Eq. 4.6 simplifies to $g_\delta^{(2)}(t) = n^2 - 2gn^2 \sum_{\mathbf{k}} e^{i\mathbf{k}\cdot\delta} \frac{\sin^2(E_k t)}{E_k^2} \epsilon_k$. Focussing on the longer range physics, I introduce dimensionless variables $\tilde{\delta} = \delta/\zeta$ and $\tilde{t} = t/\tau_{MF}$ and write

$$g_\delta^{(2)} - n^2 = -\frac{2}{\pi^2 \tilde{\delta}} n \zeta^{-3} \int_0^\infty d\tilde{k} \tilde{k} \frac{\sin(\sqrt{2}\tilde{k}\delta)}{\tilde{k}^2 + 2} \times \sin^2\left(\sqrt{\tilde{k}^2(\tilde{k}^2+2)}\tilde{t}\right) \tag{4.14}$$

where $k = \sqrt{2}\tilde{k}/\zeta$, and I have neglected $\tilde{g}^{(2)}$. The minus sign in front of Eq. 4.14 reflects the fact that for repulsive interactions the probability of finding a particle a distance δ apart is smaller than for a non-interacting system.

In Fig. 4.2, I plot the evolution of the density-density correlation function $g^{(2)} - n^2$ as a function of $\tilde{t}$ for $\tilde{\delta} = 4$. Focussing on the short time dynamics I find that the correlations rapidly oscillate. The temporal period of oscillations increases with time. The structure is revealed in a saddle point approximation (with the dominant wave-vectors near $k \sim \delta/t$). Within this approximation, $g_\delta^{(2)}$ oscillates as $\sin(\delta^2/t + \phi)$.

The temporal location of the last maximum in the correlation function (t_{max}) is denoted by an arrow in Fig. 4.2(left). In the inset, I show how this feature disperses with $\tilde{\delta}$. When $\delta \leq \zeta = \hbar/\sqrt{m g_f n}$, the correlations spread diffusively ($\delta \propto \sqrt{t}$), while for $\delta \geq \zeta$, correlations spread ballistically ($\delta \propto vt$). This is indicated by the linear plus square root fit shown in the inset. The slope of the linear part matches the sound velocity of the system. Therefore, the time-evolution of the density-density correlation function can be used to extract the sound velocity of an interacting Bose gas.

Physically, this crossover behavior arises from the Bogoliubov dispersion. At short distances, the large momentum structure of the dispersion dominates $E_k \sim k^2$, causing diffusive dynamics; longer range correlations are governed by the linear part of the dispersion and spread ballistically.

To further illustrate the existence of this crossover, I also consider a quench in the reverse direction from $g_i > 0$ to $g_f = 0$. Note that even for a quench to the non-interacting state, density-density correlations evolve in time (though the condensate fraction remains fixed). I find that

$$g_\delta^{(2)}(t) = g^{(2)}(t=0) - 4n \sum_k e^{i\mathbf{k}\cdot\delta} \sin(\epsilon_k t)^2 u_k(0) v_k(0) \tag{4.15}$$

Introducing dimensionless variables as before:

$$g_\delta^{(2)}(\tilde{t}) - g^{(2)}(t=0) = 2\frac{n\zeta^{-3}}{\pi^2\tilde{\delta}} \int_0^\infty \frac{\sin(\sqrt{2}\tilde{k}\tilde{\delta}) \sin(\tilde{k}^2\tilde{t})^2}{\sqrt{\tilde{k}^2+2}} \tag{4.16}$$

The minus sign in front of the expression Eq. 4.14 signifies that upon increasing the repulsive interactions, the probability of finding a particle a certain distance apart from another particle decreases. On the other hand, for a quench to zero interactions, density density correlations grow in time.

As in the case of the quench from $g_i = 0$, correlations show rapid oscillations at short times, eventually saturating to some aymptotic value. As shown in Fig. 4.2, the temporal location of the last maximum in this correlation function disperses *diffusively* on all length scales as the non-interacting dispersion is $E_k = k^2/2m$ for all k. We find $\tilde{\delta} = \pi\sqrt{\tilde{t}_{min}}$. Thus the short time dynamics of the density-density correlation function is strongly influenced by the underlying dispersion.

At very small distances and short times, the dynamics is governed by the higher momentum component of the dispersion which is k^2 like. This causes short range correlations to disperse diffusively in time.

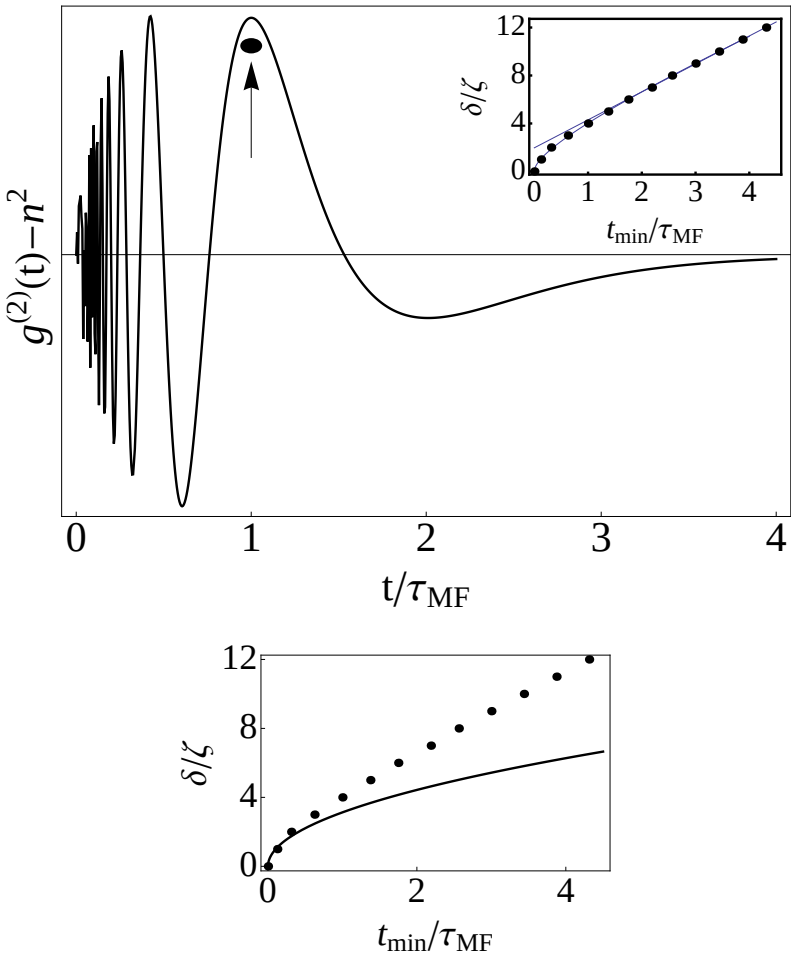

Figure 4.2: **Short-time dynamics of density-density correlations in 3D** Top: density-density correlations $g^{(2)}(\delta/\zeta = 4) - n^2$ normalized to the asymptotic value at long times for a quench from a non-interacting state to some final $g_f > 0$. Length and time is measured in terms of the condensate healing length ($\zeta = \hbar/\sqrt{mg_f n}$) and mean-field time $\tau_{MF} = \hbar/(g_f n)$ in the final state. Correlations develop in an oscillatory manner and rapidly saturate at times $t - \delta/c > \tau_{MF}$. Inset shows the temporal location of the maximum in the correlation function (arrow on left graph) (abscissa) plotted versus δ/ζ (ordinate). Long range correlations $\delta/\zeta \gg 1$ spread ballistically while short range correlations $\delta/\zeta \ll 1$ spread diffusively. The lines show purely linear and linear plus square root fit to the data. The slope of the linear part matches the sound velocity of the gas. Bottom: Dots are the same as the inset on left. Solid line shows the location of the last maximum in the correlation function for a quench from finite interactions to $g = 0$. The dynamics are purely diffusive in this case, with a diffusion constant $\approx \pi$.

4.4.2 Long time dynamics: Exponential versus algebraic decay

Equally interesting is the manner in which the correlations decay once they have developed. I revisit the two quenches considered in the previous subsection individually.

For a quench from $g = 0$, the phase of the $\sin^2(E_k t)$ term in Eq. 4.14 oscillates rapidly and can be replaced by $1/2$ to yield

$$g_\delta^{(2)}(t \to \infty) = n^2 - \frac{n\zeta^{-3}}{4\pi\tilde{\delta}} e^{-2\tilde{\delta}} \tag{4.17}$$

where $\tilde{\delta} = \delta/\zeta$. Thus at long times, $g_\delta^{(2)}$ appears to diverge as $\delta \to 0$. On distances much shorter than ζ, one must also include the contribution from $\tilde{g}_\delta^{(2)}$, which yields an even stronger divergence as $1/\delta^2$. Therefore, at small distances, $g_\delta^{(2)} \sim 1/\delta^2 - a/\delta$ [24]. At large δ, $g^{(2)}(\delta)$ approaches n^2 from below, as expected for a repulsive gas.

In order to study how this quantity approaches Eq. 4.17 on long times, I write $\sin^2(E_k t) = \frac{1}{2}(1 - \cos(2E_k t))$ and substitute $E_k \approx ck$. Integrating the resulting expression we find:

$$g_\delta^{(2)}(\tilde{t}) - g_\delta^{(2)}(\tilde{t} \to \infty) = -\frac{1}{4\pi\tilde{\delta}} n\zeta^{-3} e^{-2(2\tilde{t}-\tilde{\delta})} \tag{4.18}$$

Thus for a quench to an interacting gas, correlations decay *exponentially* on times $\tilde{t} > \tilde{\delta}/2$. The timescale for this decay is set by τ_{MF} in the interacting state.

I now consider the reverse quench, namely from an interacting gas to a non-interacting gas. Performing the same analysis as before, I find that on long times, the correlations asymptote to

$$g_\delta^{(2)}(t \to \infty) = n^2 + \frac{n}{6\pi^2\zeta^3\tilde{\delta}}\Big[4\tilde{\delta} - 3\pi(I_2(2\tilde{\delta}) - L_2(2\tilde{\delta}))\Big] \tag{4.19}$$

where I_2 and L_2 are the Bessel and Struve L functions of the second kind respectively.

For small $\tilde{\delta}$ the term in square brackets behaves linearly in δ, while at large distances is scales as $1/\tilde{\delta}$. Therefore, at very short distances $\delta \ll \zeta$, $g^{(2)}$ approaches a *constant* value of $n^2+2n/(3\pi^2\zeta^3) = n^2+4nn_{ex}$, which is the Hartree-Fock result for the density correlations in a non-interacting Bose gas at finite temperatures [25, 26]. (Note that there is no short distance divergence in the density-density correlation function for a non-interacting Bose gas at finite temperature – this is purely a feature of the singular repulsive interactions.) At long distances it decays to n^2 as $1/\tilde{\delta}^2$. The long time density-density correlation function is plotted in Fig. 4.3.

Once again replacing $\sin^2(k^2t)$ with $\frac{1}{2}(1-\cos(2k^2t))$, I now perform the integral in Eq. 4.16 numerically to find that correlations asymptote to their steady state values *algebraically*. Further analysis reveals that they decay as $(t/\tau_{MF})^{-1}$. In Fig. 4.3, I plot the long time behavior of the density-density correlation function for both types the quenches. For the case of a quench from zero interactions, the mean-field time of the final state sets the characteristic relaxation time for the correlation function. On the other hand, for a quench to zero interactions, the mean-field relaxation time diverges ($\tau_{MF} \propto 1/\sqrt{g} \to \infty$ as $g \to 0$), producing a qualitatively different behavior in the long time dynamics of the correlation function.

It is tempting to connect the behavior found above and that observed numerically and experimentally in strongly interacting Bose gases [7, 14, 15]. Analytic calculations in 1D lattice Bose gas have shown that for sudden quenches from a Mott insulating initial state to a non-interacting final state, density-density

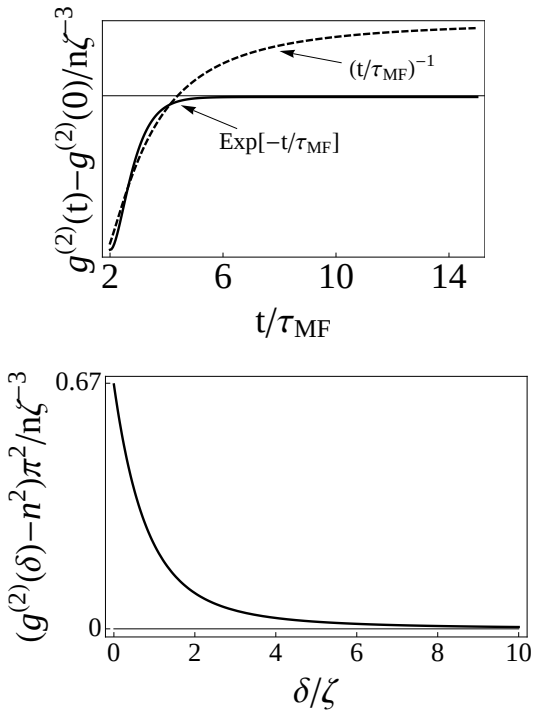

Figure 4.3: **Long-time density-density correlation function** Top: Long time behavior of the density-density correlation for the quenches considered in Sec. IVA: dashed curve: quench *to* zero interactions from some initial interaction strength $g > 0$. solid curve: quench to a finite interaction $g > 0$ from $g = 0$. In either case, lengths and times are normalize to the coherence length and mean-field time in the interacting initial/final state. Bottom: Density-density correlation function at long times following a quench from finite interaction strength to $g = 0$. The equilibrium value of $g^2(\delta)$ for a non-interacting condensate is n_0^2. The corresponding finite temperature correlation function is shown in the dashed curve. At long distances $g^{(2)}_{\delta\gg\zeta}(t = \infty) \to n^2 + O(\tilde{\delta}^{-2})$ from above, whereas for short distances $g^{(2)}_{\delta\ll\zeta}(t = \infty) \to n^2 + 4nn_{ex}$.

correlations decay *algebraically* as $(t/J)^{-1}$, where the hopping J is the natural energy scale in the problem [14, 15], while experimental and numerical work on quenches in the strongly interacting regime find a much more rapid decay of correlations [7, 15]. Although I do not directly model the Munich experiments here, very similar behavior occurs in the weakly interacting case.

4.5 Lattice vs. continuum

I now ask whether additional features are found in the presence of an underlying lattice. The conceptually simplest case to consider is a quench from finite interactions to $g = 0$, in the presence and absence of a lattice. To relate our calculations to experiments, I choose a 1D lattice with band structure $\epsilon(k) = 4J\sin^2(kd/2)$, but the physics described here is qualitatively similar in higher dimensions.

I start by numerically integrating Eq. 4.15 in 1 dimension, and plot the resulting density-density correlation function in Fig. 4.4. As in the 3D case, I find a single feature which spreads diffusively for all δ. Next I substitute a lattice dispersion in Eq. 4.15 to obtain:

$$g^{(2)}_{\tilde{\delta}}(t) = g^{(2)}_{\tilde{\delta}}(0) + \frac{2g_i n^2}{\pi d}\int_{-\pi}^{\pi} dk e^{ik\tilde{\delta}} \frac{\sin(4J\sin^2(k/2)t)^2}{|\sin(k/2)|\sqrt{4J\sin^2(k/2)+2g_i n}} \tag{4.20}$$

where $\tilde{\delta} = \delta/d$. Normalizing the energy and time units by J, I numerically integrate Eq. 4.20 and plot in Fig. 4.4 the typical post-quench dynamics of the density-density correlations as a function of time, following such a quench. I choose $g_i n/J = 1$, none of the qualitative features discussed here are affected by this choice.

At long times, the correlations in the lattice and continuum both decay to their asymptotic values algebraically, but in addition, the lattice introduces periodic oscillations. The period of these oscillations is largely independent of δ, and is proportional is set by the band-width. These oscillations are a purely lat-

tice effect and were also observed experimentally for quenches within the Mott insulating phase [7].

The differences between the lattice and continuum are even more striking at short times, as these reveal the high momentum structure of the underlying excitation spectrum. In Fig. 4.4, I plot the density-density correlation function for different values of δ and highlight two features. For comparison I also show the density-density correlations in the continuum for the same quench. The open circles denote the position of the first maximum in the correlation function while the filled circles denote the minimum in the correlation function. These features disperse differently, the position of the maximum disperses ballistically, while the position of the minimum disperses diffusively.

The linearly dispersing maximum has no analog in the continuum and emerges purely due to the lattice band-structure, which imposes a maximum velocity ($4Jd$ [11] in 1D) on the spreading of correlations. The analog of this feature in the strongly interacting case has been studied in detail recently both theoretically and experimentally [7, 15].

For quenches to an interacting final state $g_f \neq 0$, the dynamics become more complicated. The minimum in the correlation functions disperses diffusively, then ballistically, similar to the 3D continuum case. The maximum in the correlation function disperses linearly with a velocity set by the band structure for small values of g_f crossing over to the superfluid velocity for larger g_f.

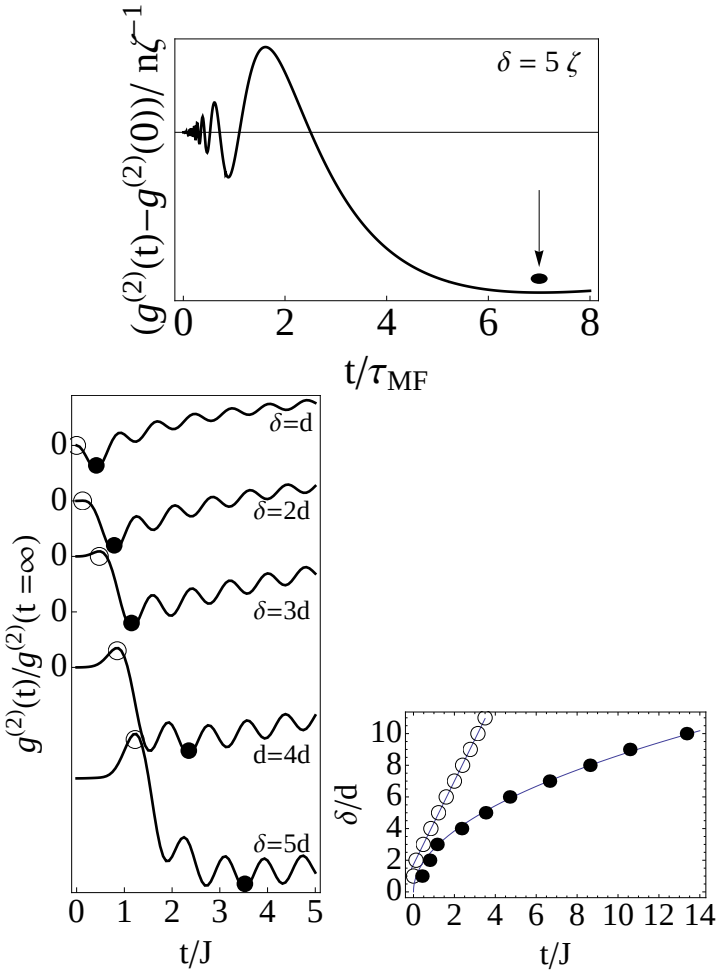

Figure 4.4: **Dynamics of density-density correlations in a 1D lattice** (Top): A plot of the evolution of the density-density correlations in the 1D continuum for the same quench at $\delta = 5\zeta$ for comparison. The minimum in the correlation function (filled circle) disperses diffusively (Bottom, Left): Typical structure of density-density correlations $g^{(2)}(\delta)(t)-g^{(2)}(\delta)(0)$ for different values of δ normalized to the asymptotic value at long times for a quench from $g_i > 0$ to $g_f = 0$. Lengths and times are measured in terms of the lattice spacing and inverse hopping J^{-1}. Correlations in a lattice oscillate with a period proportional to $1/J$ and decay with a time constant independent of δ. The temporal location of the first maximum (t_{max}) and the minimum (t_{min}) are indicated by open and filled circles. (Bottom, Right): t_{max} disperses ballistically at all distances, while t_{min} disperses diffusively. This latter features is the analog of the quantity highlighted on the top right.

4.6 Short distance structure of two-particle correlations

Thus far, I have neglected the contribution to the correlation functions arising purely from the non-condensed atoms. For $\delta \sim \zeta$, and weak interactions, these terms are of order $O(a/\zeta)^2$, (for typical densities $a \sim 50$nm and $\zeta \sim \mu$m) and can be ignored. However for $\delta \ll \zeta$, these terms give rise to a $1/\delta^2$ divergence in the correlation function as a result of the singular nature of the relative wave-function of two particles interacting with a zero range interaction [24]. The two-particle correlation function $g^{(2)}(\delta) \sim (1 - a/\delta)^2$ where the correlations between non-condensed particles dominate the short distance behavior and the interaction between the condensed and non-condensed particles leads to a sub leading $1/\delta$ correction which is opposite in sign.

Recently Shina Tan showed that for a two-component Fermi gas interacting with a contact interaction, the short distance structure of the two-body correlation is related to the internal energy via the "contact" defined as $C = \lim_{\delta\to 0} \delta^2 g^{(2)}(\delta)$ [28]. For a Bose-Einstein condensate, C to leading order is $16\pi^2 n_0^2 a^2(1 + O(\sqrt{na^3}))$ [24, 31]. Experiments using Bragg spectroscopy to probe the Fourier transform of $g^{(2)}$ have a typical momentum resolution of $k = 2\pi/\delta_{min}$ where $\delta_{min} \sim 0.5\mu$m [29]. As a result, experiments actually probe $C(\delta) = \delta^2 g^{(2)}(\delta)$ evaluated at δ_{min}.

The dominant contribution to these correlations from the non-condensed atoms is a term of the form $\tilde{g}^{(2)}_\delta = |\sum_{\mathbf{p}} e^{i\mathbf{p}\cdot\delta} u^*_p(t)v_p(t)|^2$. Adding this term to Eq. 4.6, and multiplying by δ^2 we numerically integrate the resulting equation to obtain $C(\delta)$ for a quench from $g_i = 0$ to $g_f = g$.

In Fig. 4.5 I plot $C(\delta)$ as a function of δ at different times. The contribution

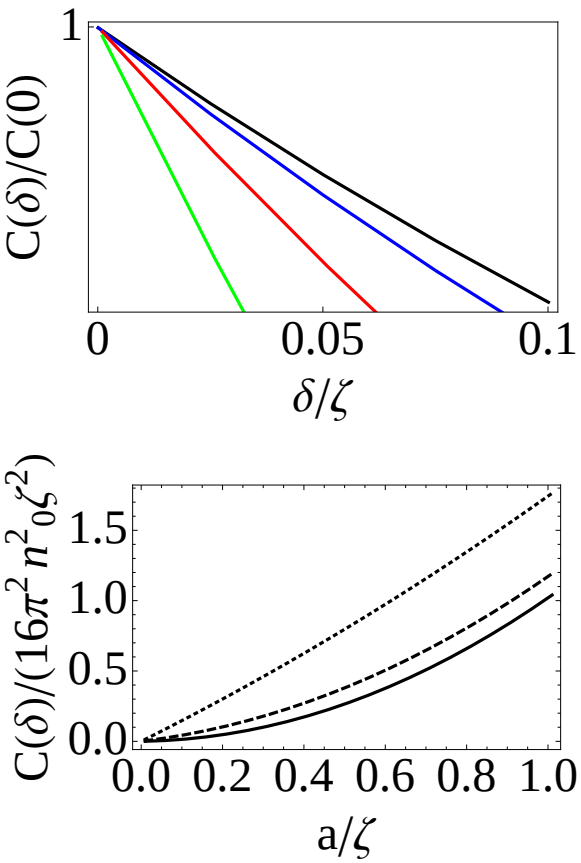

Figure 4.5: **Dynamics of the contact $C(\delta)$ in a 3D Bose gas:** (Top) Dynamics of the position dependent contact $C(\delta) = \delta^2 g^{(2)}(\delta)$ (normalized to the true contact within the Bogoliubov approximation) at different times following the quench, as a function of δ. At $t < 0$, the gas is non-interacting and $C(\delta) = 0$. Immediately after the quench, the zero distance correlations respond instantaneously. Colors correspond to different times: $t/\tau_{MF} = 0.025$ (green), 0.1 (red), 0.3 (blue), 0.9 (black). We choose $a = 5\zeta$. For times $\tau > \tau_{MF}$, $C(\delta)$ saturates to it's equilibrium value for a given δ. (Bottom) Dependence of $C(\delta)$ with scattering length a measured in units of ζ. From top to bottom: $\delta/\zeta = 1$, $\delta/\zeta = 0.1$ and $\delta/\zeta = 0.01$. In order to obtain the expected quadratic dependence of the true contact C with a for a Bose-Einstein condensate, one has to probe correlations on length scales $\delta \sim$ nm.

to $g^{(2)}$ from correlations between the condensate and the non-condensate atoms dominates unless $\delta/\zeta \ll 1$ or $a \geq \zeta$. I choose $a = 5\zeta$ (although smaller values of a yield the same qualitative result). Immediately following the quench, the zero range correlations jump to their equilibrium value. However $\mathcal{C}(\delta)$ changes in time for finite δ and relaxes to a stationary value (denoted by the black curve) on times $t \sim \tau_{MF}$. Therefore, although the true contact does not have any time-dependence, the experimentally relevant quantity $\mathcal{C}(\delta)$ changes in time following an interaction ramp.

Finally I note that *even in equilibrium* the scattering length dependence of $\mathcal{C}(\delta)$ is strongly influenced by δ. For example, the $\delta \sim \mu$m scale studied in experiments, one has to go to very large interactions in order to suppress the contribution to $g^{(2)}$ arising from correlations between the condensed and non-condensed atoms. This is illustrated this in Fig. 4.5 (right) where I plot $\mathcal{C}(\delta, a)$ as a function of a for different values of δ, after the system has equilibrated following the ramp. For $\delta \sim \zeta$ (typically μm), $\mathcal{C}(a)$ varies linearly with a at small a. The quadratic dependence of $\mathcal{C}(\delta)$ with a for a weakly interacting BEC emerges only for small δ ~nm.

In Fig. 4.5 I plot the dynamics of $\mathcal{C}(\delta)$ for different values of δ for different times. Note that the true contact $\mathcal{C}(0)$ suddenly jumps to it's equilibrium value in the final state. However the experimentally measured contact shows dynamics. For small values of δ, the $\mathcal{C}(\delta)$ approaches it's equilibirum value on a time $t \sim \tau_{MF}$. As the inset shows, in order to probe the true contact, the experimental resolution needs to be $\delta \leq 0.01\zeta \sim 10$nm.

4.7 Conclusions

Relating the information contained in the fluctuations of an interacting system driven out of equilibrium to the underlying many body parameters is a challenging task. Here I have studied a simple model, a homogenous Bose gas at zero temperature, where one can calculate the one and two body correlations of the system following a sudden change in the interactions. My study reveals that the dynamics of these correlations reveal a wealth of information about the underlying excitation spectrum of the system.

First, I considered the dynamics of single particle correlations, such as the condensate fraction or equivalently, the excited fraction of atoms following a sudden interaction ramp. For a quench from a non-interacting gas, I found that all the dynamics are governed by a single timescale, the mean-field time. For quenches between two interacting systems, there are two relevant timescales governing the long and short term dynamics of the gas. The excited fraction at long times after the quench is always greater than the expected equilibrium value.

Next, I considered the dynamics of the two particle correlation function. For quenches between interacting initial and final states, I found a non-trivial crossover between diffusive spreading of short-range correlations and the ballistic spread of long range correlations. I related this crossover to the underlying Bogoliubov dispersion and showed that the interacting dispersion leads to a much more rapid decay of correlations as compared to the free case.

I studied the case of a Bose gas in a lattice and discuss the additional features that arise in the correlations from the band structure. Comparing a 1D

lattice with the 1D continuum case, I found that the band structure leads to an additional linearly dispersing feature in the correlation functions. For a non-interacting final state, the velocity is set by the bandwidth, while for an interacting final state, it crosses over to the sound speed of the gas.

Finally I discussed the dynamics of the contact following a sudden quench. I found that while the true zero range contact instantaneously takes on the new equilibrium value, the finite resolution of an experiment will make the contact appear time dependent.

BIBLIOGRAPHY

[1] W. S. Bakr, A. Peng, M. E. Tai, R. Ma, J. Simon, J. Gillen, S. Foelling, L. Pollet and M. Greiner Science **329** 547 (2010).

[2] C-L. Hung, X. Zhang, L-C. Ha, S-K Tung, N. Gemelke and C. Chin New. J. Phys. **13** 075019 (2011).

[3] M. Greiner, O. Mandel, T. W. Hänsch and I. Bloch, Nature **419** 51 (2002).

[4] H. Miyake, G. Siviloglou, G. Puentes, D. E. Pritchard, W. Ketterle and D. M. Weld, Phys. Rev. Lett. **107** 175302 (2011).

[5] S. Trotzky, Y-A. Chen, A. Flesch, I. P. McCulloch, U. Schollwöck, J. Eisert, and I. Bloch Nature Physics **8** 325 (2012).

[6] S. S. Natu, D. C. McKay, B. DeMarco and E. J. Mueller, Phys. Rev. A **85** .061601 (R) (2012).

[7] M. Cheneau, P. Barmettler, D. Poletti, M. Endres, P. Schaub, T. Fukuhara, C. Gross, I. Bloch, C. Kollath and S. Kuhr, Nature, **481** 484 (2012).

[8] C-L. Hung, V. Gurarie and C. Chin, eprint.arXiv:1209.0011.

[9] A. Imambekov, I. E. Mazets, D. S. Petrov, V. Gritsev, S. Manz, S. Hofferberth, T. Schumm, E. Demler and J. Schmiedmayer, Phys. Rev. A **80** 033604 (2009).

[10] E. H. Lieb and D. W. Robinson, Commun. Math. Phys., **28** 251 (1972).

[11] P. Calabrese and J. Cardy, Phys. Rev. Lett., **96** 136801 (2006).

[12] M. Moeckel and S. Kehrein Phys. Rev. Lett. **100** 175702 (2008).

[13] C. Kollath, A. Laeuchli and E. Altman, Phys. Rev. Lett. **98** 180601 (2007).

[14] S. S. Natu and E. J. Mueller arXiv: 1201.6674.

[15] P. Barmettler, D. Poletti, M. Cheneau and C. Kollath, Phys. Rev. A **85** 053625 (2012).

[16] A. Polkovnikov, S. Sachdev, S. M. Girvin, Phys. Rev. A **66** 053607 (2002).

[17] M. Rigol and A. Muramatsu, Phys. Rev. Lett. **93** 230404 (2004).

[18] S. Manmana, S. Wessel, R. M. Noack and A. Muramatsu, Phys. Rev. B **79** 155104 (2009).

[19] M Gring, M. Kuhnert, T. Langen, T. Kitagawa, B. Rauer, M. Schreitl, I. Mazets, D. A. Smith, E. Demler and J. Schmiedmayer, Science **337** 1318 (2012).

[20] T. Kinoshita, T. Wenger and D. Weiss, Nature **440** 900 (2006).

[21] J. D. Sau, B. Wang and S. Das Sarma, Phys. Rev. A **85** 013644 (2012).

[22] T. W. B. Kibble, J. Phys. A **9** 1387 (1976); W. H. Zurek, Nature **317** 505 (1985).

[23] U. R. Fischer, R. Schutzhold and M. Uhlmann, Phys. Rev. A **77** 043615 (2008).

[24] T. D. Lee, K. Huang and C. N. Yang, Phys. Rev. **106** 1135 (1957).

[25] M. Naraschewski and R. J. Glauber, Phys. Rev. A **59** 4595 (1999).

[26] *Bose-Einstein Condensation in Dilute Gases* C.J.Pethick and H.Smith, Cambridge University Press, 2002.

[27] F. Dalfovo, S. Giorgini, L.P. Pitaevskii, and S. Stringari, Rev. Mod. Phys. **71** 463 (1999).

[28] S. Tan, Ann. Phys. **323** 2952 (2008); 2971 (2008); 2987 (2008); E. Braaten and L. Platter, Phys. Rev. Lett. **100** 205301 (2008); F. Werner, L. Tarruell and Y. Castin Eur. Phys. J B **68** 401 (2009); S. Zhang and A. J Leggett, Phys. Rev. A **79** 023601 (2009).

[29] E. D. Kuhnle *et al.* Phys. Rev. Lett. **105** 070402 (2010).

[30] J. M. Diederix, T. C. F van Heijst and H. T. C Stoof, Phys. Rev A **84** 033618 (2011).

[31] R. J. Wild, *et al.* Phys. Rev. Lett. **108** 145305 (2012).

[32] T. A. Corcovilos, *et al.* Phys. Rev. A **81** 013415 (2010).

[33] E. Altman, E. Demler and M. D. Lukin, Phys. Rev A **70** 013603 (2004);

[34] M. Greiner, C. A. Regal J. T. Stewart and D. S. Jin Phys. Rev. Lett. **94** 110401 (2005).

[35] S. I. Shevshenko, Sov. J. Low Temp. Phys. **18** 223 (1992).

[36] D. S. Petrov, G. V. Shlyapnikov and J. T. M. Walraven, Phys. Rev. Lett. **85** 3745 (2000).

[37] A. Griffin, T. Nikuni and E. Zaremba *Bose-Condensed Gases at Finite temperatures* Cambridge University Press Cambridge, (2009).

[38] *Theory of Quantum Degenerate Gases* Erich J. Mueller, PhD Thesis (2001).

CHAPTER 5

DYNAMICS OF CORRELATIONS IN SHALLOW OPTICAL LATTICES

This Chapter was adapted from "Dynamics of correlations in shallow optical lattices", by Stefan S. Natu and Erich J. Mueller, which is currently under review for publication in Physical Review A. I now consider the same problem as in chapter 4, with a different initial state: namely a Mott insulator. In this Chapter, I am interested in asking whether any of the features predicted in Chapter 4 are generic

5.1 Introduction

In Chapter 4, I used a Bogoliubov mean-field approach to study the generic features arising in correlation functions following an interaction quench within a weakly interacting superfluid. An extremely interesting question, which is largely in the domain of sophisticated numerical methods, is how various correlations functions evolve following a quench from a *Mott insulating* initial state to a superfluid. This question is particularly topical as there are several experimental groups with the tools to answer these questions, both in real and momentum space [1, 2, 3, 4, 5, 6, 7, 8, 9, 10, 11, 12].

In this Chapter, I calculate how density-correlations evolve following such a quench, and how quasimomentum is redistributed. By working in the weakly interacting limit I produce *analytic* expressions. In particular, the time dependence of the static structure factor is quite simple. My weak coupling calculations complement classical field studies [13, 14, 15] valid at large filling factors, sophisticated numerically exact approaches [16, 17, 18, 19, 20, 21, 22] and strong coupling theories [8, 23] . A remarkable fact is that much of the physics seen in

these sophisticated calculations is already present in my calculations.

This study is also particularly relevant to understanding how *isolated*, *quantum* systems approach equilibrium [16, 24, 25, 26, 27, 28, 29]. This is a relatively new area of research, primarily motivated by experiments in ultra-cold gases. Studying this question in the context of thermal phase transitions led to an understanding of spinodal decompositions and thermal coarsening [31]. Whether similar behavior occurs for quantum quenches is at present unclear.

Here I study the momentum distribution of the lattice Bose gas after a sudden quench to weak interactions. I demonstrate that in 1D, our system does *not* relax to thermal equilibrium on a timescale $t \sim J/(Un_0)^2$ following the quench, despite having exponentially decaying correlations in real space. However, in higher dimensions, the momentum distribution rapidly approaches a thermal distribution. For the one and two dimensional cases considered here, quasi-long range order is never established in finite time.

Before delving into the details of the calculation, I describe a recent experiment on a 1D lattice Bose gas that has motivated my calculations [11]. The experimental procedure involves first creating a degenerate gas of ^{87}Rb atoms in 1 dimensional tubes containing roughly 20 atoms per tube. Counter propagating lattice beams create an optical lattice in the long axis of the tube. The lattice depth is slowly ramped up till the system is well into the Mott insulating initial state. The lattice depth is then suddenly lowered on a timescale fast compared to the tunneling time such that the system is close to the Mott-superfluid critical point but still in the Mott state. The system is allowed to evolve for a time t after the ramp and then the lattice depth is suddenly increased to $80E_R$ to freeze the atoms in place, after which they are imaged using flourescence imaging. From

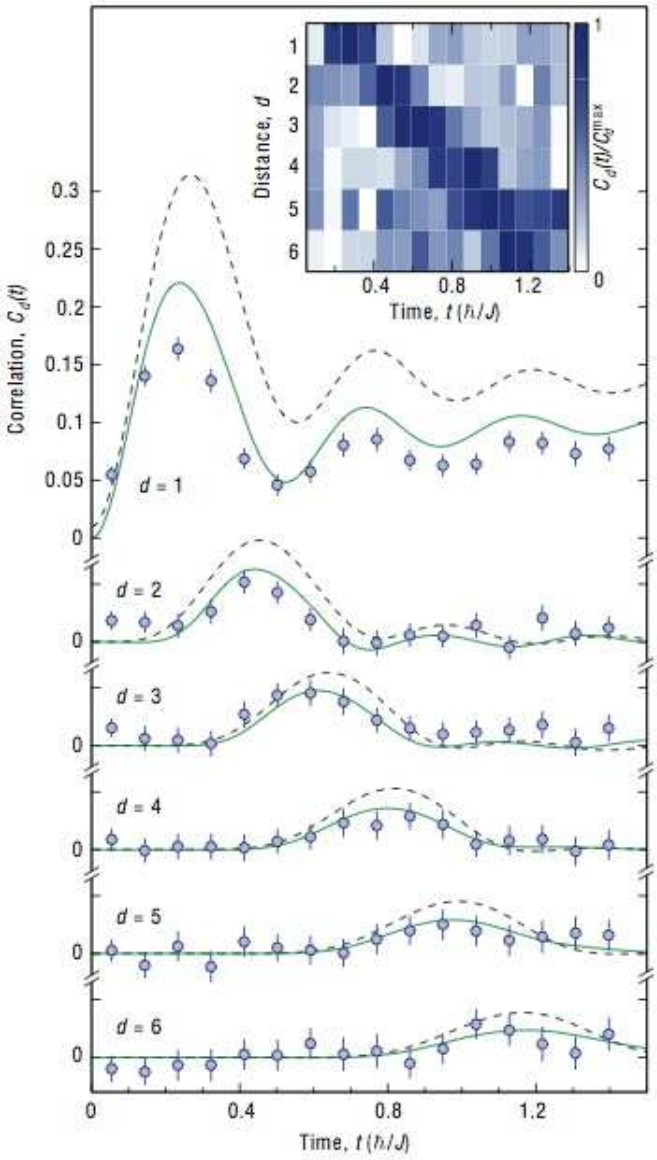

Figure 5.1: **Light-cone evolution of density-density correlations in a 1D Bose gas** Experimental plot showing the *ballistic* spreading of density-density correlations for a quench within the Mott insulating phase. This image is reproduced from [11].

the resulting snapshot of the atoms positions, the density-density correlation function is determined (plotted in Fig. 5.1).

The plot shows that correlations spread ballistically through the system following the quench. In this chapter I consider a much simpler version of this

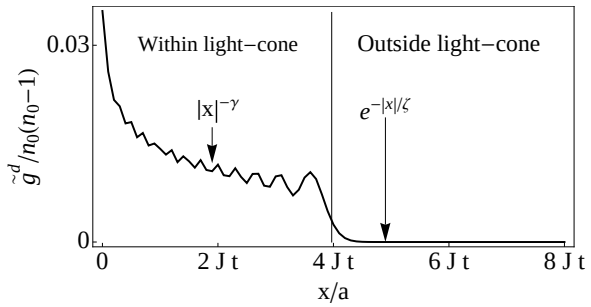

Figure 5.2: **Generic structure of light-cone dynamics in** 1 **dimension:** Density-Density correlation function $\tilde{g}^d = \langle a_d^\dagger(t) a_0^\dagger(t) a_0(t) a_d(t) \rangle$ plotted after some time t of evolution following a quench to a *non-interacting state*. The vertical line demarcates the region within the light-cone after this time. Correlations decay exponentially outside the light-cone with some correlation length ζ. Within the light cone, correlations decay as algebraically with some exponent γ. For the quench considered here, we numerically find γ to be quite small, on the order of 10^{-2}. Characteristic oscillations on the order of a lattice site are observed, arising purely from the underlying lattice band-structure.

experiment. I consider a quench from a Mott insulating initial state (initially at $J/U = 0$) to a non-interacting final state ($U = 0$). Rather surprisingly, the features in this simplified case are strikingly similar to those in the experiment.

The experiment in Fig. 5.1 is an example of *light-cone dynamics*, wherein immediately following a quench, the system responds by producing quasi-particles which propagate in different directions with some velocity (v which may depend on direction) [24, 30]. After some time t, quasi-particles from different regions of space arrive at the same point and interfere, causing those regions to become causally connected. This gives rise to a light-cone effect, where correlations develop in a power law manner in regions within the light cone but decay exponentially outside the light-cone (see Fig. 5.2). In this chapter, I will investigate this phenomenon for the case of weakly interacting systems.

5.2 Formalism

I consider a homogeneous gas of bosons in an optical lattice described by the single-band Bose-Hubbard Hamiltonian [32, 33]:

$$\mathcal{H} = -J \sum_{\langle ij \rangle} \left(a_i^\dagger a_j + h.c \right) + \sum_i \left[\frac{U}{2} n_i (n_i - 1) - \mu n_i \right] \tag{5.1}$$

where $a_i(\mathtt{t})$ denotes the boson annihilation operator at site i, J denotes the hopping and U the on-site repulsive interaction. The kinetic energy sum is over nearest neighbor pairs $\langle ij \rangle$.

The basic objects of this study are the one- and two-body density matrices; $g^i_j(\mathtt{t}) = \frac{1}{i}\langle a_i^\dagger(\mathtt{t}) a_j(\mathtt{t})\rangle$ and $g^{ij}_{kl}(\mathtt{t}) = -\langle a_i^\dagger(\mathtt{t}) a_j^\dagger(\mathtt{t}) a_k(\mathtt{t}) a_l(\mathtt{t})\rangle$, where $a_i(\mathtt{t})$ denotes the boson annihilation operator at site i and time $\mathtt{t}$. More generally one can write the n-body density matrix as $g^{i_1 \ldots i_n}_{j_1 \ldots j_n}(\mathtt{t}) = \frac{1}{i^n}\langle a_{i_i}^\dagger(\mathtt{t}) \ldots . a_{i_n}^\dagger(\mathtt{t}) a_{j_n}(t) \ldots a_{j_1}(\mathtt{t})\rangle$. In various references, these are also referred to as the n-body correlation functions, the $2n$ point functions, or the equal time Green's functions.

The one- and two-body correlation functions can be readily probed in cold-atom experiments. The former is related to the momentum distribution function $g(\mathbf{k}) = \frac{1}{i}\langle a_{\mathbf{k}}^\dagger a_{\mathbf{k}}\rangle = \sum_{i,j} e^{i\mathbf{k}\cdot(i-j)} g^i_j$, which is probed through bandmapping [3, 4] or time-of-flight [10, 12]. The density-density correlation function g^{ij}_{ji} can be measured directly using the advanced imaging techniques developed at Chicago, Harvard and Munich [5, 6, 7]. Momentum resolved experiments such as Bragg scattering [1, 2] or noise spectroscopy [8, 9] can be used to probe the structure factor $S(\mathbf{q}) = \langle \rho_{\mathbf{q}}^\dagger \rho_{-\mathbf{q}}\rangle = -\sum_{ij} e^{i\mathbf{q}\cdot(i-j)} g^{ij}_{ji}$, where $\rho_{\mathbf{q}} = \sum_{\mathbf{k}} a^\dagger_{\mathbf{k}+\mathbf{q}} a_{\mathbf{k}}$.

The equations of motion for the n-body Green's functions are constructed

from the equations of motion for the operators $a_i(t)$ and $a_i^\dagger(t)$:

$$i\partial_t a_i = -Ja_{\langle i\rangle} + Ua_i^\dagger a_i a_i - (\mu - U)a_i \tag{5.2}$$

where all temporal dependence is implicit.

For the one- and two-body Green's functions we obtain:

$$i\partial_t g_j^i = -J(g_{j+\langle j\rangle}^i - g_j^{i+\langle i\rangle}) - iU(g_{ij}^{ii} - g_{jj}^{ij}) \tag{5.3}$$

$$\begin{aligned} i\partial_t g_{kl}^{ij} = -J\left(g_{k+\langle k\rangle}^{ij} + g_{kl+\langle l\rangle}^{ij} - g_{kl}^{i+\langle i\rangle j} - g_{kl}^{ij+\langle j\rangle}\right) \\ -iU(g_{ikl}^{iij} + g_{jkl}^{ijj} - g_{kkl}^{ijk} - g_{kll}^{ijl}) \end{aligned} \tag{5.4}$$

where the notation $\langle i\rangle$ denotes a sum over all the nearest neighbors of site i. For example, in one dimension $g_{j+\langle j\rangle}^i = g_{j+1}^i + g_{j-1}^i$. In a translationally invariant system (such as the one I consider) $g_{j+\langle j\rangle}^i = g_j^{i+\langle i\rangle}$, and the term proportional to J in Eq. 5.3 vanishes.

The interaction term couples the n-body Green's function with the $n+1$-body Green's function. The full interacting many body dynamics is described by the resulting infinite set of coupled differential equations.

Here I limit myself to the case of a shallow lattice, where interactions are weak following the quench. The single-band Bose Hubbard model is a valid description of bosons in optical lattices even for shallow lattices ($J/U \gg 1$), provided that the mean separation between the bands is larger than the interaction energy (alternatively $V_R/E_R > 1$, where V_R is the lattice depth). Most of the experiments are in this regime.

Throughout this Chapter, we assume that the initial state at time $t < 0$ is a homogeneous Mott insulator with n_0 bosons per site ($U = \infty$). At $t = 0$ we

suddenly quench the system to a final value of interactions $U \geq 0$ and study the subsequent evolution of the correlation functions. The dynamics is studied using a weak-coupling perturbation theory in the dimensionless parameter U/J which is assumed to be small following the quench.

Since I am interested in the weakly interacting regime, understanding the non-interacting limit is crucial [23]. I first set $U = 0$ and calculate the *non-interacting* density-density correlation functions (Eq. (5.4)). I then perturbatively include the effects of U, determining how interactions influence the density-density correlations and the quasi-momentum redistribution in the lattice (Eq. 5.3).

5.3 Density-Density Correlations in 1D

I start by considering a one dimensional system and choose a homogenous initial state with a density of n_0 bosons per site. At $\mathtt{t} < 0$, the sites are completely decoupled, leading to a uniform quasi-momentum distribution with magnitude $g(k) = n_0$. At $\mathtt{t} = 0$, I suddenly quench the system to a *non-interacting* state $U = 0$.

In the absence of interactions, there is no quasi-momentum redistribution, and the momentum occupations do not change in time. This can be easily seen by taking the Fourier transform of Eq. 5.3. However density-density correlations given by Eq. 5.4 show interesting dynamics. To solve Eq. (5.4), it is convenient to define a reduced two body Green's function $\tilde{g}^{ij}_{kl} = g^{ij}_{kl} - g^i_k g^j_l - g^i_l g^j_k$. Since the one body correlations do not evolve in time, $\tilde{g}^{ij}_{kl}$ obeys the same dynamical equation as g^{ij}_{kl}. At $\mathtt{t} = 0$, $\tilde{g}^{ij}_{kl} = n_0(n_0 + 1)$ if $i = j = k = l$, but 0 otherwise. In Fourier space this becomes $\tilde{g}^{pq}_{rs} = n_0(n_0 + 1)\delta(p + q - r - s)$.

Setting $U = 0$, Eq. 5.4 is readily solved in Fourier space to yield $\tilde{g}^{pq}_{rs}(\mathtt{t}) = e^{-i2J\ \mathtt{t}(\cos(p)+\cos(q)-\cos(r)-\cos(s))} g^{pq}_{rs}(\mathtt{t}=0)$. At $\mathtt{t} = 0$, $g^{pq}_{rs}(\mathtt{t}=0) = n_0(n_0-1)\delta(p+q-r-s) + n_0^2(\delta(p-s)\delta(q-r) + \delta(p-r)\delta(q-s))$. The second term generates no dynamics and produces an overall constant, which I ignore.

In real space, the density-density correlation function then becomes:

$$\tilde{g}^{ij}_{ji}(\mathtt{t}) \equiv \tilde{g}^{d} = n_0(n_0-1)\int_{-\pi}^{\pi}\frac{dk}{2\pi}e^{2ikd/a}J_0[4J\ \mathtt{t}\sin(k)]^2 \tag{5.5}$$

where $\tilde{g}^{ij}_{ji}$ symbol is the correlation function after subtraction of the constant term, $d = i - j$, and $i^\nu J_\nu(z) = \frac{1}{2\pi}\int_{-\pi}^{\pi} dk\ e^{i(\nu k + z\cos(k))}$ is the Bessel function of first kind. A similar expression for the non-interacting limit has been also derived by Barmettler *et al.* who focus on quenches to much stronger interactions ($U \geq J$) [23].

In Fig. 5.3, I plot the dynamics of the two body Green's function. As is apparent in the figure, the density correlations spread in a light-cone-like manner (similar to Fig. 5.1). One can extract a characteristic velocity associated with the ballistic spread of correlations by plotting the location of the maximum of $\tilde{g}^d$ (indicated in Fig. 5.3 by the dashed line) as a function of d. I obtain a velocity of $v = 3.7Ja$. Studies by Barmettler *et al.* show that this velocity has a dependence on d and approaches $4Ja$ as $d \to \infty$ [23].

I emphasize that "light-cone dynamics" is a feature of the lattice and *not* the interactions. As pointed out by Calabrese and Cardy, the initial state has very high energy ($E = 0$ in my case) compared to the ground state of the final Hamiltonian ($E_g = -2J$ in my case) and acts as a source for quasi-particles traveling in different directions [24]. These matter waves carry information about correlations in the initial state. At time $\mathtt{t}$ after the quench, the waves emanating from points $d = 2v\mathtt{t}$ apart interfere, giving rise to an interference pattern

in the density-density correlation function. In the non-interacting limit, these matter waves consist simply of freely propagating bosons propagating with a maximum velocity of $2Ja$ in opposite directions, giving rise to the factor of 2 in the above expression for d. Correlations decay exponentially outside the region described by the light-cone (see Fig. 5.2).

The density-density correlations for a non-interacting gas (Eq. 5.5) bear a striking similarity to the features observed both numerically and experimentally in the strongly interacting regime [11, 22, 23]. In fact, these features appear to be generic and have also been observed in interacting Fermi systems [30]. This similarity suggests that a similar mechanism is responsible for the build-up of correlations in the strongly interacting limit, where instead of freely propagating bosons, one has freely propagating doublon and holon pairs with a new propagation velocity. For very strong interactions, one estimates that the doublon hopping matrix element is $J_{doublon} = 2J$), and correlations propagate with a velocity $v \sim 2Ja(1+2) = 6Ja$, which is consistent with the experimental and numerical findings [23, 11].

I now briefly discuss the signatures of light-cone dynamics in momentum space. In Fig. 5.3, we also plot the structure factor obtained by taking the Fourier transform of the density-density correlation function. This can simply be read off from Eq. 5.5 as $S(q)(\mathtt{t}) = n_0(n_0-1)J_0[4J\,\mathtt{t}\sin(q/2)]^2$. At $\mathtt{t} = 0$, the structure factor is a constant as all momentum states are equally occupied. As the system begins to develop correlations between neighboring sites, the structure factor shows periodic oscillations whose amplitude decays in time. Using the asymptotic behavior of the Bessel function $J_0(z) \sim (2/\pi z)^{1/2}\cos(z-\pi/4))$ as $z \to \infty$, we find that for long times the oscillations have period $\tau_{osc} = \pi/[4J\sin(k/2)]$. At

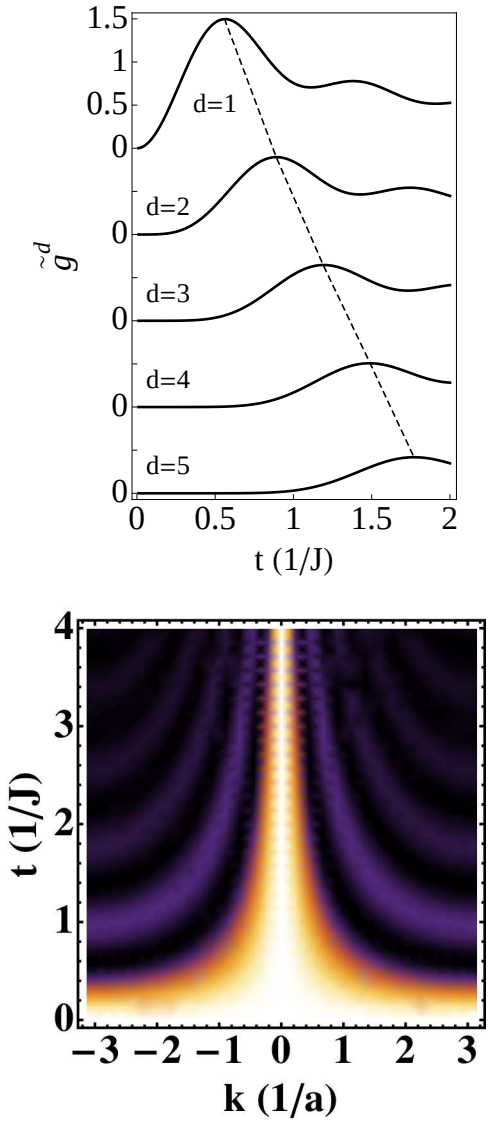

Figure 5.3: **Light-cone evolution of density-density correlations in 1D.** (c.f. Fig. 2, Ref. [11]). Top: Density-density correlation function for a homogeneous, non-interacting system $\tilde{g}^{ij}_{ji}(\mathtt{t}) \equiv \tilde{g}^d(\mathtt{t})$ ($d = i - j$). Line shows the location of the peak in $\tilde{g}^d$ used to extract the velocity of spread of correlations. We find $v = 3.7Ja$, consistent with the spreading velocity expected for non-interacting particles. As discussed in the main text, the structure of the density-density correlations is robust against interactions to first order in U/J. Bottom: Time-Evolution of the structure factor. Lighter colors indicate higher intensity. At $\mathtt{t} = 0$, all momenta are equally occupied and $S(k)(0) = 1$ for all k. At intermediate times $S(k)$ shows oscillations due to interference between atomic wave-packets moving ballistically. Higher momentum contributions to $S(k)$ decay as $1/J\mathtt{t}$, consistent with the linear spreading of correlations in real-space.

long times, the correlations are found to decay to steady state values as $1/J\mathtt{t}$. In k space, the envelope of the structure factor decays as $1/k$. These features can be readily accessed in experiments.

The long time behavior of correlations however is very different in the non-interacting and strongly interacting limit. In contrast with the rather slow decay of correlations for the quench to $U = 0$, density-density correlations appear to decay rapidly in the strongly interacting case [11, 23]. The mechanism for the decay contains information about the nature of the quasi-particles and their interactions and merits further study.

We now consider a quench to a weakly interacting final state $U/J \ll 1$ and compute the effect on the density-density correlation functions to first order in perturbation theory. Interestingly, we find that the non-interacting density-density correlations are completely unaffected.

In order to calculate g_{rs}^{pq} to first order in interactions, we Fourier transform Eq. 5.4 and assume that the three-body correlator g_{suv}^{pqr} evolves freely as it would for a non-interacting system. We then substitute the expression for the three-body correlation function into Eq. 5.3 and obtain the two-body correlation function in Fourier space (details are supplied in Appendix E):

$$
\begin{aligned}
g_{rs}^{pq}(\mathtt{t}) = \Bigg(g_{rs}^{pq}(0) - i\frac{Un_0^2(n_0-1)}{J} \times \int_0^{\mathtt{t}} d\tau \delta_{p+q-r-s} \sum_{\delta} J_\delta(\tau)^2 \Big(i^{2\delta} e^{i\tau(\cos p+\cos q)} e^{-i\delta(q+p)} - \\
i^{-2\delta} e^{-i\tau(\cos r+\cos s)} e^{i\delta(r+s)} \Big) - i\frac{Un_0(n_0-1)(n_0-2)}{J} \times \\
\int_0^{\mathtt{t}} d\tau \delta_{p+q-r-s} \sum_{\delta} J_\delta(-\tau)^3 \Big(i^{\delta} (e^{i\tau\cos p} e^{-i\delta p} + e^{i\tau\cos q} e^{-i\delta q}) - \\
i^{-\delta} (e^{-i\tau\cos r} e^{i\delta r} + e^{-i\tau\cos s} e^{i\delta s}) \Big) \Bigg) \times e^{-i\mathtt{t}(\cos p+\cos q-\cos r-\cos s)}
\end{aligned}
\tag{5.6}
$$

The first term in the brackets is the non-interacting two-point correlation function which now acquires a time and momentum dependent correction of order U/J from the three-body terms (Eq.5.4).

Taking the Fourier transform of the above expression, one finds that g_{ji}^{ij} is completely unaffected to linear order in U/J, for any filling. Our calculations imply that for a quench to the weakly interacting regime, g_{ji}^{ij} scales as $g_{ji}^{ij}(\mathtt{t}) \sim g_{ji}^{(0)ij}(\mathtt{t}) + O(Un/J)^2$, where $g_{ji}^{(0)ij}(\mathtt{t})$ is the non-interacting density-density correlation function calculated above.

Different behavior is found when the initial state is a weakly interacting superfluid (Chapter 4). In this case, following the quench, the density-density correlation function to leading order is proportional to $U\ n_0 n_{ex}$ where n_0 is the condensate density and n_{ex} is the density of quasi-particle excitations out of the condensate.

5.4 Momentum distribution in 1D

As in the case of the density-density correlations, I calculate the momentum distribution perturbatively in the final (dimensionless) interaction strength U/J. In the absence of interactions ($U = 0$), there is no momentum redistribution. Thus we must take $U \neq 0$ after the quench in Eq. 5.3.

To leading order in the interaction strength U, we solve Eq. 5.3 by replacing the two body correlator $g_{ij}^{kl}(\mathtt{t})$ with the noninteracting result in Eq. 5.5. Defining $x \equiv 2J\mathtt{t}$ and using the integral identity $J_\nu(z) = \frac{i^{-n}}{2\pi}\int_{-\pi}^{\pi} d\theta e^{i(n\theta + z\cos(\theta))}$, I find that the occupation numbers obey:

$$\partial_{\mathtt{t}} g_q(\mathtt{t}) = \frac{U n_0(n_0-1)}{2J} \sum_{k=-\infty}^{\infty} J_k(-\mathtt{t}) J_k^2(\mathtt{t}) \times \left(i^{-k} e^{i(qk - \mathtt{t}\cos(q))} - i^{k} e^{-i(qk - \mathtt{t}\cos(q))} \right) \tag{5.7}$$

where I have normalized time in units of $1/2J$. Note that to first order in U/J, interactions merely shift the magnitude of the momentum distribution. The right-hand-side of Eq. 5.7 is invariant under the inversion $q \to -q$ but switches sign under the transformation $q \to \pi - q$. This implies that $q = \pm\pi/2$ is a stationary point and states at $q = \pi/2$ have no dynamics. In real space, this symmetry implies $g^i_j = 0$ if $d = |i - j|$ is even.

To lowest order in interactions, I assume that the two-body correlation function behaves as if interactions are absent, *i.e* every momentum state evolves independently $g^{pq}_{rs} \sim \delta(p + q - r - s) e^{-i2J\mathtt{t}(\cos(p)+\cos(q)-\cos(r)-\cos(s))}$, while conserving total momentum. States at $q = \pm\pi/2$ do not evolve, as $\cos(q)$ vanishes here.

In Fig. 5.4, I plot the evolution of the quasi-momentum states obtained by integrating Eq. 5.7. At $\mathtt{t} = 0$, all momentum states are equally occupied. At short times following the quench, quasi-momentum states explore the band and the low momentum occupation begins to grow. At intermediate times, the momentum distribution develops peak-like features which migrate towards the stationary points $q = \pm\pi/2$. Expanding Eq. 5.7 near $q = \pi/2$, one finds that the slope of the momentum distribution near $\pi/2$ grows as $(\mathtt{t}/J)^{2/3}$.

At long times, the rate of momentum redistribution slows down, and the system settles into a more or less steady state with a relatively flat quasi-momentum profile near $q = 0$, and sharp peaks near $q = \pm\pi/2$. Owing to this spectral feature, in real space only g^i_j (with $d = |i - j|$ odd) are appreciable at long

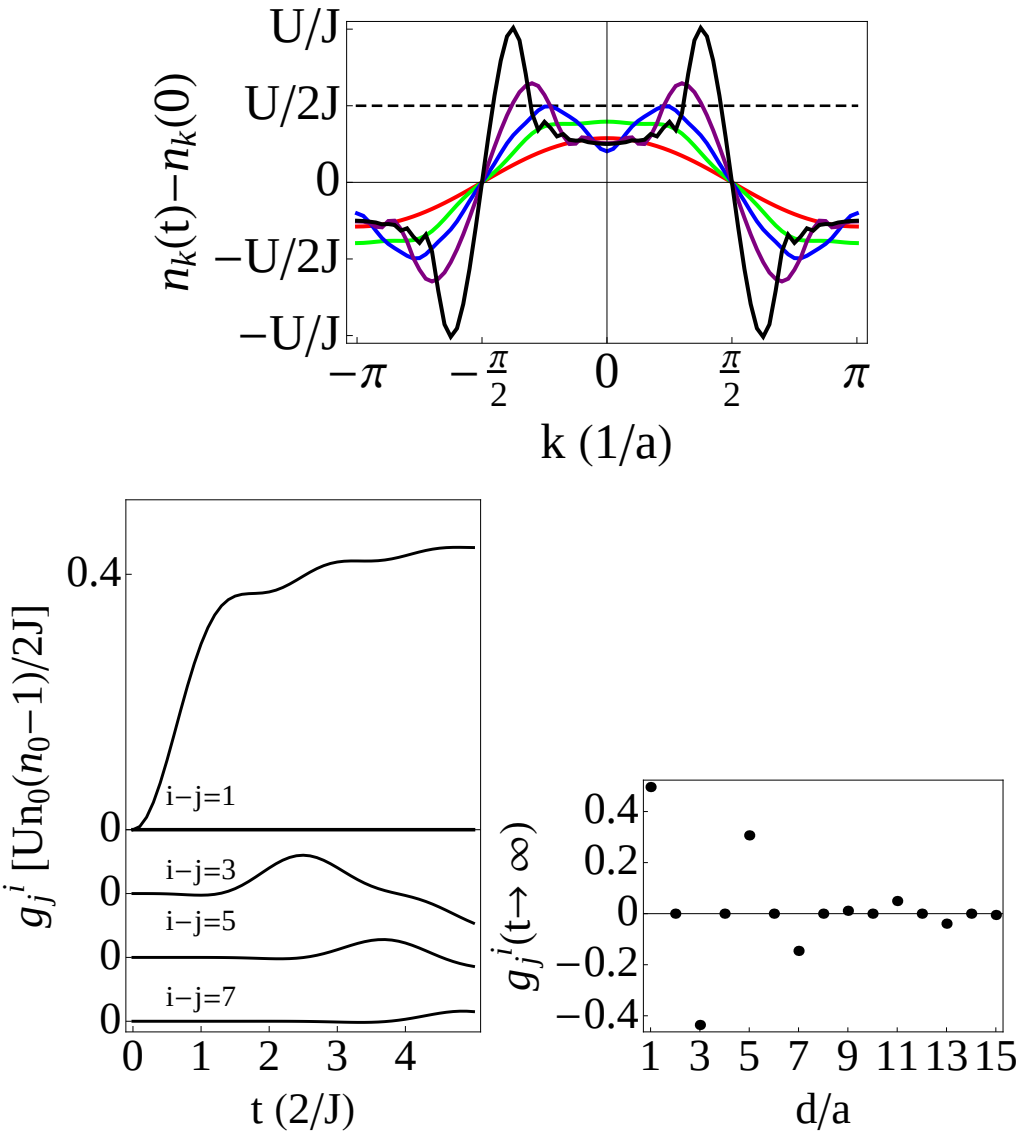

Figure 5.4: **Coherent redistribution of quasi-momentum to linear order in U/J in 1D.** Top: Redistribution of quasi-momentum ($n_k = \langle a_k^\dagger a_k \rangle$) at times $t = 0$ (thick, dashed), $t = 0.5/J$ (red), $2.5/J$ (green), $5/J$ (blue), $12.5/J$ (purple), $25/J$ (black) obtained by integrating Eq. (5.7). At short times, we find a coherent transfer of quasi-momentum from high momentum states to low momentum states. At longer times, I find a pile-up of particles near $k = \pm\pi/2$. Bottom (Left): Spatial evolution of the one-body density matrix $g_j^i(t)$ for different values of $d = i - j$. Short range correlations rapidly saturate while longer range correlations take time to develop. (Right): Correlations $g_j^i - n_0$ measured in units of $Un_0(n_0 - 1)/2J$ in real space as a function of $d = i - j$ at long times $t = 100/J$. Correlations vanish if d is even. Appreciable long range correlations never develop even on long times.

times.

The Fourier transform of the momentum distribution reveals the dynamics of the one-body density matrix, which is plotted in Fig. 5.4. At short times the single-particle correlations spread in a manner similar to the density correlations. Local correlations are rapidly established on a time of order J^{-1}. Long range order, however, requires communication between widely separated sites and generically takes longer to develop.

As correlations can develop at best linearly in time, infinite range order is not found at any finite time. This is evidenced in Fig. 5.4 (bottom-right) where the one-body density matrix is plotted as a function of the separation $d = i - j$ between sites at long times. The envelope of the one-body density matrix (for odd sites) is found to decay *exponentially* indicating an absence of any long range order.

Although the system reached a steady state, with exponentially decaying correlations in real space, the momentum distribution in Fig. 5.4 is distinctly "athermal". I attribute this to the fact that to first order in U/J the evolution conserves the occupation of quasi-momentum at $q = \pm\pi/2$.

It is then natural to ask whether this momentum distribution will survive when particles are allowed to scatter to and from $q = \pm\pi/2$. These effects first enter at order $(U/J)^2$, and are considered below. By substituting the first order result in the two-point function g_{rs}^{pq} (Eq. 5.6) into the expression for the momentum distribution Eq. 5.3, we can calculate the effect of a single "collision" event on the momentum distribution of Fig. 5.4.

The linear approximation developed here breaks down whenever the height

of the peaks near $q = \pm\pi/2$ become comparable to the initial density. At this point, we expect non-linear processes such as collisions between quasi-momentum states.

The full expression for the momentum distribution upon inclusion of the second order terms reads:

$$\partial_{\mathtt{t}} n_q = -i\frac{Un_0(n_0-1)}{2J}\Big[\sum_k J_k^2(\mathtt{t})J_k(-\mathtt{t})\Big(i^{-k}e^{i(kq-\mathtt{t}\cos q)} - i^k e^{-i(kq-\mathtt{t}\cos q)}\Big)\Big] + \tag{5.8}$$
$$\frac{(Un_0)^2(n_0-1)}{J^2}\mathcal{R}\Big[\sum_{k,\delta}\int_0^{\mathtt{t}} d\tau J_\delta^2(\tau)J_{-k}(\mathtt{t})\Big(J_{k-\delta}(\tau-\mathtt{t}) + \frac{n_0-2}{2n_0}J_{-\delta}(\tau)J_k(-\mathtt{t})\Big)\Big[i^k J_{k-\delta}(\tau-\mathtt{t})$$
$$\times e^{-i(kq-\mathtt{t}\cos q)} - i^{k-\delta}J_k(-\mathtt{t})e^{-i((k-\delta)q+(\tau-\mathtt{t})\cos q)}\Big]\Big]$$

where $\mathcal{R}$ denotes the real part of the expression. The details of the calculation are presented in Appendix F.

The first term in the right hand side of Eq. 5.8 is simply the first order result, rewritten.

The second term, proportional to $(U/J)^2$ has two contributions: The term proportional to $n_0^2(n_0-1)$ represents the scattering of two-particles and is the dominant process at this order. In addition, there is a sub-leading contribution (which has an additional factor of J_k in Eq. 5.8) which arises due to scattering of *three* particles.

In Appendix F, I discuss both these terms and their effect on the momentum distribution independently. I find that unlike the first order result which was anti-symmetric about $q = \pm\pi/2$, both the $O(U/J)^2$ terms give rise to a distribution that is symmetric about $q = \pm\pi/2$. The term proportional to

$n_0(n_0-1)(n_0-2)\delta(p+q+r-s-u-v)$ in Eq. E.3 tends to *decrease* the occupation of momentum states near $q=\pi/2$, while terms like $n_0^2(n_0-1)\delta_{ps}\delta_{q+r-u-v}$ in Eq. E.3 tends to *increase* the occupation near $q=\pi/2$. To quadratic order in perturbation theory, this term dominates over the former, ultimately *enhancing* the peak-like features seen at finite momentum. Evolving the system for longer times the momentum occupation develops *symmetric* peaks about $q=\pm\pi/2$. This is rather surprising as naively one may expect the system to "thermalize" due to scattering. However, as shown in Fig. 5.5 for the longest times we were able to simulate, we find that the $(U/J)^2$ term tends to enhance the peak-like feature at finite momentum.

In Fig. 5.5, I plot the momentum distribution upon inclusion of the quadratic terms. I attribute the appearance of peaks at $q=\pi/2$ to the restricted phase space available for scattering in 1D. Near $q=\pi/2$, the dispersion becomes linear and the constraints of momentum and energy conservation relax into a single constraint. One may expect therefore that the bulk of the two particle scattering occurs near these points. Unlike fermions, Bose statistics tends to *enhances* the probability of scattering into states that are already occupied, thus leading to an enhancement of the peaks over time.

I emphasize however that our approach only captures the initial stages of equilibration. A full treatment of thermalization should take multiple scattering processes into account and is beyond the scope of this work. In the Appendix I show that scattering of three particles tends to suppress the occupation near $q=\pi/2$. These processes will become important on times $\mathtt{t}\sim J^2/U^3$, and may eventually drive the system to a thermal distribution.

One can understand the resulting momentum distribution by considering

the energy conserving processes that are allowed. In a 1 dimensional lattice, kinematic constraints severely restrict the available scattering phase space. One available scattering channel is for particles to scatter from $q = 0$ and π into $q = \pi/2$, thereby conserving both energy and momentum. As the density of states is largest at $q = 0$ and $q = \pi$, one expects this process to dominate over the reverse process whereby particles scatter out of $q = \pi/2$ and into $q = 0$ and π. As a result, two-body scattering tends to enhance the occupation at $q = \pm\pi/2$.

The structure near $q = \pm\pi/2$ in Fig. 5.5 is reminiscent of the peaks seen in simulations of expanding 1D interacting bosons by Rigol and Muramatsu [18] and subsequently by Rodriguez *et al.* [19]. My calculation which is valid for times $t \sim J/U^2$ finds a similar suppression in the momentum occupation at $k = 0$. Taking the Fourier transform of the momentum distribution, we find that the one-body density matrix now develops correlations between even sites. However at long distances, correlations still decay exponentially, long range order is not observed. Thus the peaks seen in the momentum distribution in my case *do not* correspond to a quasi-condensate.

Rather, my calculations are similar in spirit to the interaction quench considered by Moeckel and Kehrein in the fermionic Hubbard model [28]. The picture they develop is that the system shows an initial build-up of correlations, reaching a non-thermal steady state on intermediate times, and an eventual approach to equilibrium on much longer timescales. My calculations point to a similar picture for quenches in lattice bosons.

Our calculations, which are exact to $O(U^2)$ reveal that the momentum distribution acquires a distinct non-thermal shape. On the other hand, correlations look "thermal" in real space as they decay exponentially.

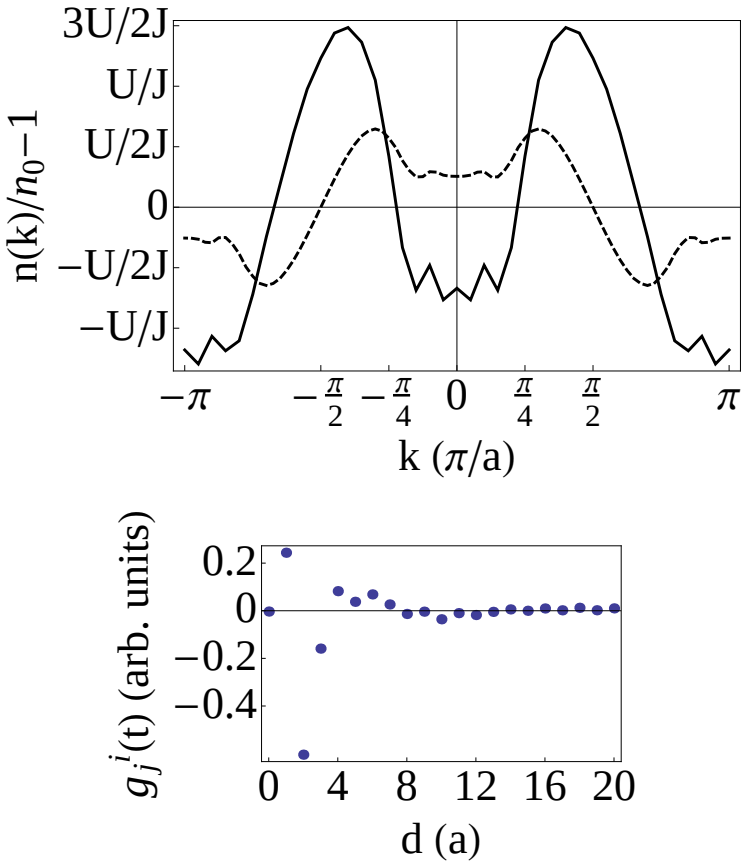

Figure 5.5: **Redistribution of quasi-momentum to $O(U/J)^2$ in 1D.** (Top): Redistribution of quasi-momentum ($n_k = \langle a_k^\dagger a_k \rangle$) at time $\mathtt{t} = 12.5/J$ (thick, solid), compared with the first order result at the same time (dashed). The interaction strength has been chosen to be $Un_0/J = 0.3$ to highlight the features of the second order calculation. On times $\mathtt{t} \sim 10/J$, the occupation of quasi-momentum near $q = \pm\pi/2$ grows in time, suppressing the occupation at zero momentum. My calculations are valid for times $\mathtt{t} \sim J/U^2$. (Bottom): Evolution of the one-body density matrix after time $\mathtt{t} = 10/J$. To quadratic order in the interactions, correlations build up between even sites. The envelope of the correlation function decays exponentially, indicating the absence of quasi-long range order.

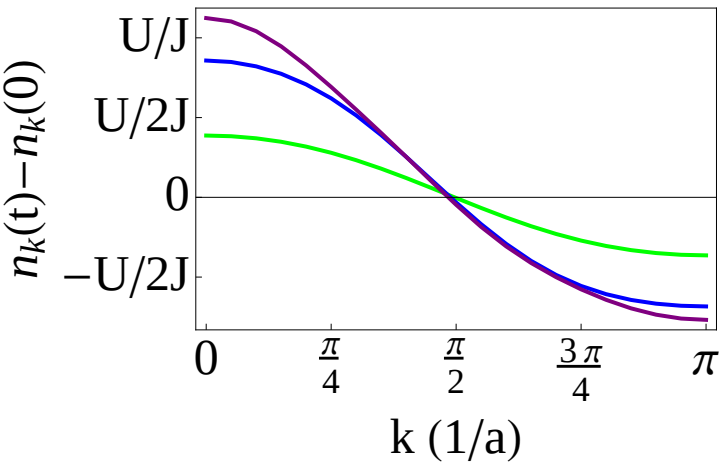

Figure 5.6: **Rapid equilibration of momentum distribution in two-dimensions** Momentum distribution along the $\{\pi, \pi\}$ vector obtained by integrating Eq. (5.3) in two-dimensions assuming an initially uniform distribution. The blue, green and purple curves correspond to times $\mathtt{t} = 0.25/J$, $\mathtt{t} = 0.5/J$ and $\mathtt{t} = 1/J$ respectively. In contrast to the one-dimensional case, the distribution evolves rapidly to a broad peak at $k = 0$, with no further dynamics.

5.5 Two dimensions

I now generalize my results to higher dimensions. Concretely, I consider the case of a two-dimensional square lattice, initially containing n_0 particles per site, and investigate the dynamics following a sudden reduction of the lattice depth to the weakly interacting limit.

Since the "light-cone" effect arises primarily due to the bounded lattice spectrum and not the interactions, one expects it to persist in higher dimensions as well. I now calculate the density-density correlations for a quench to $U = 0$ in 2D. Repeating my 1D arguments in one higher dimensions, one immediately finds the structure factor evolves according to $S(q_x, q_y)(\mathtt{t}) = n_0(n_0 - 1)J_0[4J\ \mathtt{t}\sin(q_x/2)]^2 J_0[4J\ \mathtt{t}\sin(q_y/2)]^2$. As in the one-dimensional case, by tak-

ing the Fourier transform of the above expression one finds that the density-density correlations evolve in a manner identical to the one-dimensional case, with a characteristic velocity that now depends on direction. At long times, correlations decay with a power law $1/\mathtt{t}^2$ (as opposed to the $1/\mathtt{t}$ decay in one-dimension). After a time $\mathtt{t}$, particle-hole correlations spread over a volume $\sim v^2\mathtt{t}^2$ where v is twice the characteristic velocity of an free particle (for example, $v \sim 4\sqrt{2}Ja$ along the $\{\pi, \pi\}$ wave-vector).

In analogy with the 1D calculations, I also calculate the momentum distribution following a quench in 2D, finding dramatic differences. Including interactions perturbatively to order $O(U/J)^2$, we plot in Fig. 5.6, the momentum distribution along $\{\pi, \pi\}$. At long times the distribution is characterized by a broad peak centered around $k = 0$. The presence of a broad peak indicates that only short range correlations are developed, and the absence of any long range order (either true long range order or algebraic).

An important difference between the one and two-dimensional results is the *timescale* for momentum distribution. While the 1D distribution continues to evolve on times $t \sim 50/J$, the 2D momentum distribution reaches a steady state much faster. This is due to the rapid decay of density-density correlations in higher dimensions, which drive the redistribution of quasi-momentum. These findings are consistent with (TEBD) calculations by Sau, Wang and Sarma [21] who consider quenches to much stronger interactions $U \sim 2J$, finding that the final momentum distribution rapidly becomes thermal.

5.6 Summary

By considering the dynamics of lattice bosons following a quench to a weakly interacting final state, I have explored how correlations develop in a many-body system. My analytic work complements the large body of numerical work on this subject by working in a regime where numerics is prohibitive due to the large Hilbert space needed to accurately capture the dynamics.

Surprisingly, much of the behavior seen in the strongly interacting system is already present for weak interactions. For example, I find that correlations develop in a manner similar to those seen in experiments [11]. I emphasize that these features are merely *lattice* effects and should not be attributed to strong interactions. Numerical studies have also found that the light-cone behavior is generic to a wide range of interaction strengths [23, 30]. I have also shown that the these features in the density density correlation function are robust to first order in perturbation theory in the interactions.

In addition, I have studied how quasi-momentum states evolve following the quench. The nature of the one-body density matrix is directly related to understanding whether the system develops long-range order after a quench. Over a decade ago there was a large body of work asking analogous questions with thermal quenches [31]. The picture they developed was one of nucleation and subsequent coarsening. Similar physics is expected in the quantum case [34]. Here I show that for a quench from the insulating phase, long range order is not established after a finite time, and the one-body density matrix decays exponentially in real space. Nonetheless we find a highly non-trivial momentum distribution in 1D, indicating that the dynamics is non-ergodic.

5.7 Future Directions for Theory and Experiment

I conclude this Chapter with a discussion of what in my view constitute important future directions for theory and experiment. On the theoretical side, an important question to understand is the "long-time" behavior of the correlation functions following a quench. A key difference between my calculations and the experimental and numerical findings is the rapid decay of correlations in the latter case. It will be extremely interesting to study whether one can extract properties of the excitation spectrum and quasi-particle decay rates from this long time behavior. A key limitation of state of the art numerical methods is that they are limited to one-dimension or small system sizes in higher dimensions. Improved Mean-field or Boltzmann equation type approaches that take into account some correlations in the initial state may be able to shed light on the dynamics of quasi-momentum in higher dimensions.

Here I have shown that non-trivial dynamics occurs even for quenches to weak interactions. It will be extremely interesting to explore this parameter regime experimentally. In particular the momentum distribution after a quench can be readily obtained by time-of-flight or bandmapping. A major advantage of experiments is that they can be performed in higher dimensions, where theory is largely restricted to mean-field type approaches that typically do not capture correlations fully [35].

An important question for both theoretical and experimental consideration is to understand whether non-integrable systems generically approach equilibrium in a three-step manner: on short times, the system is effectively "collisionless" and supports freely propagating quasi-particles bearing information about

the initial state; on intermediate timescales it approaches a non-thermal but steady state due to interference and dephasing between these quasi-particles and on long times, the system loses memory of its initial state, and ultimately approaches equilibrium driven largely by collisions between low energy degrees of freedom.

I hope that future experiments along these lines will be able to determine the nature of the final state after such a quench and settle questions regarding the emergence of long range order and thermalization in isolated quantum systems.

Acknowledgements.— I would like to thank the organizers and participants of the KITP program entitled *Quantum Dynamics in Far from Equilibrium Thermally Isolated systems* for numerous engaging and stimulating discussions. In addition, I would like to thank Marc Cheneau and David Huse for numerous discussions regarding this work.

BIBLIOGRAPHY

[1] M. Weidemüller, A. Hemmerich, A. Görlitz, T. Esslinger and T. W. Hänsch, Phys. Rev. Lett. **75** 4583 (1995); G. Raithel, G. Birkl , A. Kastberg, W. D. Phillips and S. L. Rolston, Phys. Rev. Lett. **78** 630 (1997);

[2] H. Miyake, G. A. Siviklglou, G. Puentes, D. E. Pritchard, W. Ketterle, and D. M. Weld Phys. Rev. Lett. **107** 175302 (2011).

[3] M. Greiner, I. Bloch, O. Mandel, T. W. Hänsch, and T. Esslinger, Phys. Rev. Lett. **87** 160405 (2001).

[4] D. McKay, M. White and B. DeMarco, Phys. Rev. A **79**, 063605 (2009).

[5] W. S. Bakr, A. Peng, M. E. Tai, R. Ma, J. Simon, J. I. Gillen, S. Folling, L. Pollet and M. Greiner, Science **329** 547 (2010).

[6] C-L. Hung C-L. Hung, X. Zhang, L-C. Ha, S-K. Tung, N. Gemelke and C. Chin, New Journal of Physics, **13** 075019 (2011).

[7] J. F. Sherson, C. Weitenberg, M. Endres, M. Cheneau, I. Bloch and S. Kuhr, Nature **467** 68 (2010).

[8] E. Altman, E. Demler and M. D. Lukin, Phys. Rev. A **70** 013603 (2004).

[9] S. Fölling, F. Gerbier, A. Widera, O. Mandel, T. Gericke and I. Bloch, Nature **434** 481-484 (2005).

[10] F. Gerbier, A. Widera, S. Folling, O. Mandel, T. Gericke and I. Bloch Phys. Rev. Lett. **95** 050404 (2005).

[11] M. Cheneau, P. Barmettler, D. Poletti, M. Endres, P. Schaub, T. Fukuhara, C. Gross, I. Bloch, C. Kollath and S. Kuhr, Nature **481** 484 (2012).

[12] M. Greiner, O. Mandel, T. W. Hänsch and I. Bloch, Nature **419** 51 (2002).

[13] A. Polkovnikov, S. Sachdev, S. M. Girvin, Phys. Rev. A **66** 053607 (2002).

[14] U. R. Fischer, R. Schutzhold, M. Uhlmann, Phys. Rev. A **77** 043615 (2008).

[15] M. Snoek, Euro Phys. Lett. **95** 30006 (2011).

[16] S. Trotzky, Y-A. Chen, A. Flesch, I. P. McCulloch, U. Schollwock, J. Eisert, and I. Bloch Nature Physics **8** 325 (2012).

[17] A. Flesch, M. Cramer, I.P. McCulloch, U. Schollwöck, and J .Eisert Phys. Rev. A **78** 033608 (2008).

[18] M. Rigol and A. Muramatsu, Phys. Rev. Lett. **93** 230404 (2004).

[19] K. Rodriguez, S. R. Manmana, M. Rigol, R. M. Noack and A. Muramatsu, New J. Phys. **8** 169 (2006).

[20] P. Barmettler, M. Punk, V. Gritsev, E. Demler and E. Altman New J. Phys **12**, 055017 (2010).

[21] J. D. Sau, B. Wang and S. Das Sarma, Phys. Rev. A **85** 013644 (2012).

[22] A. M. Läuchli, and C. Kollath, J. Stat. Mech. P05018 (2008).

[23] P. Barmettler, D. Poletti, M. Cheneau and C. Kollath, Phys. Rev. A **85** 053625 (2012).

[24] P. Calabrese and J. Cardy, Phys. Rev. Lett., **96** 136801 (2006).

[25] T. Kinoshita, T. Wenger and D. Weiss, Nature **440** 900 (2006).

[26] C. Kollath, A. Laeuchli and E. Altman, Phys. Rev. Lett. **98** 180601 (2007).

[27] M. Cramer, C. M. Dawson, J. Eisert and T. J. Osborne, Phys. Rev. Lett. **100** 030602 (2008).

[28] M. Moeckel and S. Kehrein Phys. Rev. Lett. **100** 175702 (2008).

[29] D. Poletti, J-S Bernier, A. Georges and C. Kollath, Phys. Rev. Lett. **109** 045302 (2012).

[30] S. Manmana, S. Wessel, R. M. Noack and A. Muramatsu, Phys. Rev. B **79** 155104 (2009).

[31] H. T. C Stoof, Phys. Rev. Lett. **66** 3148 (1991); Phys. Rev. A **45** 8398 (1992); D. S. Hall, M. R. M Matthews, J. R. Ensher, C. E. Wieman, and E. A. Cornell, Phys. Rev. Lett. **81** 1539 (1998); P. Ao and S. T. Chui, J. Phys. B **33** 535 (2000); M. J. Bijlsma, E. Zaremba and H. T. C. Stoof Phys. Rev. A **62** 063609 (2000).

[32] M. Greiner, O. Mandel, T. Esslinger, T. W. Hänsch, and I. Bloch, Nature, **415** 39 (2002).

[33] M. P. A. Fisher, P. B. Weichman, G. Grinstein and D. S. Fisher Phys .Rev. B **40** 546 (1989).

[34] R. Barnett, A. Polkovnikov and M. Vengalattore, Phys. Rev. A **84** 023606 (2011).

[35] S. S. Natu, D. C. McKay, B. DeMarco and E. J. Mueller, Physical Review A **85** 061601 (R) (2012).

CHAPTER 6

LOCAL VERSUS GLOBAL EQUILIBRATION NEAR THE BOSONIC MOTT-SUPERFLUID TRANSITION

This chapter is adapted from "Local versus global equilibration near the bosonic Mott-superfluid transition", with Dr. Kaden R. A. Hazzard and Erich Mueller. The work is published in Physical Review Letters ***106*** *125301 (2011). In this chapter I continue to understand what one learns from probing local and global fluctuations following a quench. In this case, I will approach the problem using a Gutzwiller mean-field approach, first discussed in Chapter 3*

6.1 Introduction

In this Chapter I continue to explore the timescales for dynamics in interacting bosonic systems by considering bosons in an optical lattice, described in Chapter 3. In particular I consider the timescales for population dynamics near the superfluid to Mott insulating transition. A new aspect in this chapter is that I consider the role of the trap in influencing the timescale for "global" dynamics in this system. I show that spatial inhomogeneites dramatically influence the timescale for redistribution of particles, leading to non-equilibrium, metastable distributions at long times. This is of practical interest to present day cold atom experiments and cooling protocols.

Understanding and controlling the equilibration of cold atom systems is one of the most important current challenges in the field. As isolated systems, the relaxation mechanisms are intrinsic and fundamental [1, 2, 3, 4, 5]. While probing non-equilibrium phenomena in condensed matter systems requires ultra fast

(~ fs) lasers, cold atoms are readily driven out of equilibium, and their subsequent dynamics can be studied on ms timescales. This makes them well suited for quantifying concepts of non-equilibrium dynamics [6, 7, 8, 9, 10, 11]. Moreover, controlling the equilibration of cold atoms is key to the next generation of experiments: for example one needs fast equilibration for condensed matter emulators [12]. Motivated by recent experiments [13, 14, 15], I conduct numerical simulations of the response of a gas of bosons to a change in the intensity of an applied optical lattice.

Despite being performed under similar conditions, *three* recent experiments [13, 14, 15] find relaxation rates for two-dimensional lattice bosons that differ by two orders of magnitude. Here I show that these discrepancies can be explained by a separation of timescales for local equilibration and global transport. I illustrate this result by numerical simulations within a time-dependent Gutzwiller mean-field theory. I further explore the parameters, such as system size and trap geometry, which influence these timescales.

The separation of timescales for local and global equilibrium is unsurprising, and emerges in most interacting systems and materials. For example, in the air around us, local equilibrium is achieved on the collision time (~ns), but global equilibrium is limited by transport coefficients and is relatively slow. Typically one expects the slow variables to be those that are conserved (such as density and energy density) and those which correspond to broken symmetries (such as the phase of the superfluid order parameter). Although we do not do so here, integrating out the fast degrees of freedom leaves "hydrodynamic" equations for the slow degrees of freedom. The form of these hydrodynamic equations are strongly constrained by symmetries, allowing phenomenological descrip-

tions [16].

A practical consequence of this separation of timescales is that adiabaticity is much easier to maintain if one changes parameters in such a way that very little mass transport is necessary – a principle which is widely used in cold atom experiments.

6.2 Model

Bosonic atoms trapped by interfering laser beams are well described by the Bose Hubbard Hamiltonian [17] introduced in Chapter 3

$$\mathcal{H} = -J \sum_{\langle ij \rangle} (a_i^\dagger a_j + h.c) + \sum_i \left(\frac{U}{2} n_i (n_i - 1) - \mu^i n_i \right) \tag{6.1}$$

where a and $a^\dagger$ are bosonic annihilation and creation operators, J is the tunneling, and U is on-site interaction. I denote $\mu^i = \mu - V_{ex}(i)$, where μ is the chemical potential and $V_{ex}(i)$ is the external potential at site i [18]. The first sum is over all nearest neighbor sites in the plane. In Figure 6.1, we show U and J as a function of lattice depth V_R for ^{87}Rb in a $d = 680$nm lattice generated by light of wavelength $\lambda = 1360$nm. For deep lattices, $U = \sqrt{8/\pi}(ka_s)E_R \sqrt{V_R/E_R}(V_{Rz}/E_R)^{1/4}$ and $J = (4/\sqrt{\pi})(E_R V_R^3)^{1/4} \exp\left(-2\sqrt{V_R/E_R}\right)$, where $E_R = k^2/2m$ is the lattice recoil energy in terms of the light wave-vector $k = 2\pi/\lambda$ for light with wavelength λ, V_R, V_{Rz} are the radial and axial lattice depths, a_s is the scattering length [19]. Different two-dimensional experiments use different strengths of axial confinement (V_{Rz}). Since U only depends on $V_{Rz}^{1/4}$, I will make the simplest choice, $V_{Rz} = V_R$. None of my conclusions are qualitatively affected by this assumption.

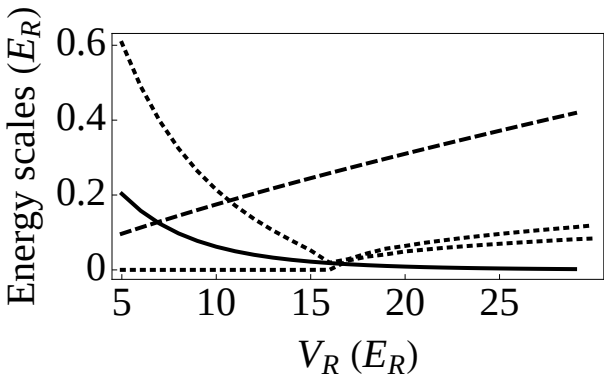

Figure 6.1: **Energy scales as a function of lattice depth**: Microscopic parameters in the $2D$ Bose-Hubbard Hamiltonian (Eq.6.1): $4J$ (solid), and U (dashed) as a function of lattice depth [18] for ^{87}Rb in a $d = 680$ nm lattice. The dotted curves are the two lowest $k = 0$ excitations from linearizing Eq. 6.3 at unity filling. In the superfluid state, the Goldstone mode has zero energy. In the Mott state, these modes represent the particle/hole excitations.

I calculate dynamics using a time dependent Gutzwiller ansatz [17] (See Chapter 3), which approximates the wavefunction by $\Psi = \bigotimes_i \sum_m c_m^{(i)}(t)|m\rangle_i$ where $|m\rangle_i$ is the m-particle Fock state on site i, and the coefficients $c_m^{(i)}(t)$ are generally space and time dependent. In a homogenous system [10], the excitation spectrum predicted by this theory agrees well with other techniques [20]. Navez and Schützhold [21] have been studying systematic improvements of this method. The time-dependent Gutzwiller is sufficiently sophisticated to yield the separation of timescales which we wish to elucidate. Recent time-dependent density matrix renormalization group calculations of the 1D Bose-Hubbard model find similar results [22] to ours.

This mean-field ansatz reduces Eq. 6.1 to a sum of single site Hamiltonians

$$\mathcal{H}_i = -4t(\langle\alpha_i\rangle^* a_i + \langle\alpha_i\rangle a_i^\dagger) + 4t|\langle\alpha_i\rangle|^2 + \frac{U}{2}n_i(n_i-1) - [\mu - V(i)]n_i \qquad (6.2)$$

at each site i. Truncating the basis at each site to a maximum M particles, $\mathcal{H}_i$

is an $(M+1)\times(M+1)$ matrix at each site, and depends on the other sites only through $\langle\alpha_i\rangle = (1/4)\sum_{\langle j\rangle}\langle a_j\rangle$, where $\left\langle a_j\right\rangle = \sum_m \sqrt{m+1}c_{m+1}^{(j)}c_m^{(j)}$, and the sum over j includes all four nearest neighbor sites.

Schrödinger's equation $i\partial_t\psi = \mathcal{H}\psi$ for Ψ yields a set of differential equations for the c_m^i:

$$i\partial_t c_m^i(t) = -4J(t)(\langle\alpha_i\rangle^* \sqrt{m+1}c_{m+1}^i + \langle\alpha_i\rangle \sqrt{m}c_{m-1}^i) + \left(\frac{U(t)}{2}m(m-1) - \mu^i m + 4J(t)|\langle\alpha_i\rangle|^2\right)c_m^i \tag{6.3}$$

The tunnelings and on-site interactions are dynamically tuned by changing the lattice depth in time (t). I study population dynamics across the superfluid-insulator transition by ramping the lattice linearly in time using the protocol $V(t) = V_\mathrm{i} + (V_\mathrm{f} - V_\mathrm{i})(t/\tau_\mathrm{r})$, where V_i and V_f are the initial and final lattice depths, and τ_r is the ramp time. The ramp protocol generically varies from experiment to experiment, but none of my qualitative results are dependent on this choice. In addition, I consider a time independent radially symmetric harmonic trap, $V_\mathrm{ex} = \frac{1}{2}m\omega^2(x^2+y^2)$.

I approximate the ground state by finding the stationary solution to Eq. 6.3, $c_m^i(t) = e^{-i\epsilon t}c_m^i$, where ϵ can be identified with the energy per site. As in Chapter 3, I then use an iterative algorithm, starting with a trial α_i, then find c_m^i by solving the eigenvalue problem in Eq. 6.3. I calculate a new α_i and repeat until the subsequent change in α_i is sufficiently small. To calculate time dynamics, I use a split-step method [23] and sequential site updates [24]. This approach conserves both total particle number and energy (for time-independent Hamiltonians) to within 1 percent.

The resulting dynamics describe the behavior of a single quantum state,

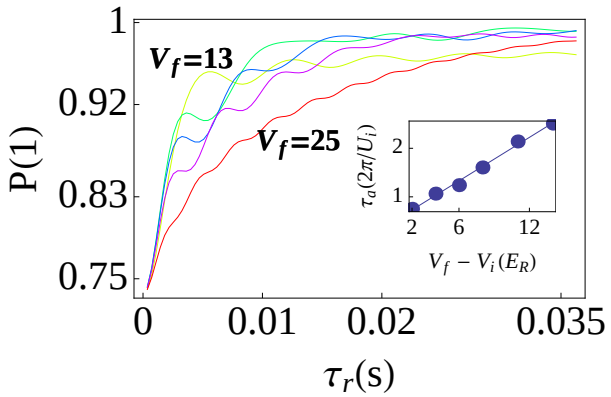

Figure 6.2: **Population dynamics at unity density** $n = 1$ (Top): Probability of having one particle per site at the end of a lattice ramp from $V_\mathrm{i} = 11E_R$ lattice to (top to bottom) $V_\mathrm{f} = 13$(yellow), 15(green), 17(blue), 19(purple) and 25(red) in units of E_R after different lattice ramp times $\tau_\mathrm{r} = 0.1/U_\mathrm{i} \sim 0.3$ms to $10/U_\mathrm{i}$. Inset: Fitting these curves to simple exponentials yields a fast timescale for lattice equilibration of $\tau_\mathrm{a} \sim \frac{2\pi}{U_\mathrm{i}}$. The best fit line is shown as a guide to the eye. Cf. Fig. (3) of [14].

rather than a density matrix. An important question to ask is whether the mean-field theory above is capable of describing *equilibration* which one generally assumes requires collisions. The Gutzwiller equations derived here are highly nonlinear and contain a large number of degrees of freedom. This structure is rich enough that under appropriate conditions time dynamics leads to thermalization, with (on average) energy equally distributed among all modes.

6.3 Homogeneous system results: Local equilibration

I consider several different scenarios in order to fully explore the response this system to a lattice ramp. To start with, I analyze a homogeneous system: this investigation yields the timescale for local equilibration. This timescale sets the fundamental limit for how fast equilibration can take place in the absence of

global mass transport. Similar to the Harvard experiments [14], I find that local equilibrium can be maintained even under relatively rapid quenches through the superfluid-Mott boundary.

In an isolated homogeneous system, ramping the depth of an optical lattice does not lead to bulk mass transport. Instead, all of the temporal dynamics simply involve the evolution of number fluctuations and correlations. Thus equilibration is governed by local physics and Eq. 6.3 reduces to the single site problem. I numerically integrate this nonlinear set of ordinary differential equations, taking J and U functions of time, corresponding to a linear ramp of the lattice from depth V_{i} to V_{f}. We vary V_{i}, V_{f}, and the ramp time τ_{r}. I take all parameters to correspond to ^{87}Rb atoms, and take $n = 1$ particles per site.

At unity filling, near the Mott transition, it suffices truncate the basis to at most 2 particles per site. In this truncated basis, the probability of having a single particle per site $P(1)$ is identical to the probability of having an odd number of particles per site, which is the experimental observable in the Harvard experiments [14].

Both of the gapped $q = 0$ single-particle excitations (see Fig. 6.1 and Ref. [20]), and the continuum of two-phonon excitations contribute to the non-adiabatic evolution. All of these modes are captured in a time-dependent Gutzwiller framework [10]. One expects that the number of excitations goes to zero as the ramp rate vanishes. The experiments at the moment are not sensitive enough to determine precisely how each of these excitations independently influences the population dynamics. When the gapped excitations of energy Δ dominate the dissipation, then the ramp becomes adiabatic when $\frac{1}{\Delta^2} d\Delta/dt \ll 1$ [25].

In Fig. 6.2, I show that the timescale for local equilibration is very short. Starting with a superfluid at $V_{\rm i} = 11E_R$, I consider ramp to different lattice depths. I plot the time evolution of the probability that a single particle sits at a given site as we vary the the ramp time $\tau_{\rm r}$ from $0.1\hbar/U_{\rm i}$ to $10\hbar/U_{\rm i}$, where $U_{\rm i} = \hbar/3$ms. This scheme is identical to that considered by the Harvard experiments [14]. Fitting these curves to simple exponentials yields a characteristic timescale $\tau_{\rm a}$, which, as shown in the inset, is comparable to $U_{\rm i}^{-1}$.

6.4 Inhomogeneous dynamics

Next I explore the requirements for maintaining global equilibrium. I show that equilibration times are much longer in systems requiring large amounts of particle transport. This situation is exacerbated by the presence of large Mott domains, as in the Chicago experiments [13].

I now consider an inhomogenous system by imposing a harmonic external potential on top of the lattice. The protocol for lattice ramps is same as before, starting with a superfluid at 11 recoil lattice depth. The central chemical potential is chosen such that the central density is close to unity, justifying the truncated basis ($M = 2$) used here. Throughout I define time in units of $2\pi/U_{\rm i}$ where $U_{\rm i}$ is the on-site interaction at $V_{\rm i} = 11E_R$ equal to $\sim 2\pi \times 300$Hz. I use a trapping frequencies $\omega = 25$Hz, which corresponds to a shallow trap.

In Fig. 6.3, I plot the density profile after a lattice ramp from $V_{\rm i} = 11E_R$ to $V_{\rm f} = 16E_R$ in a time $t = 120 \times 2\pi/U_{\rm i}$ for a system 30×30 sites containing 500 particles. As shown already, this ramp is sufficiently slow to be locally adiabatic. The parameters are chosen such that at later times a large Mott region separates the

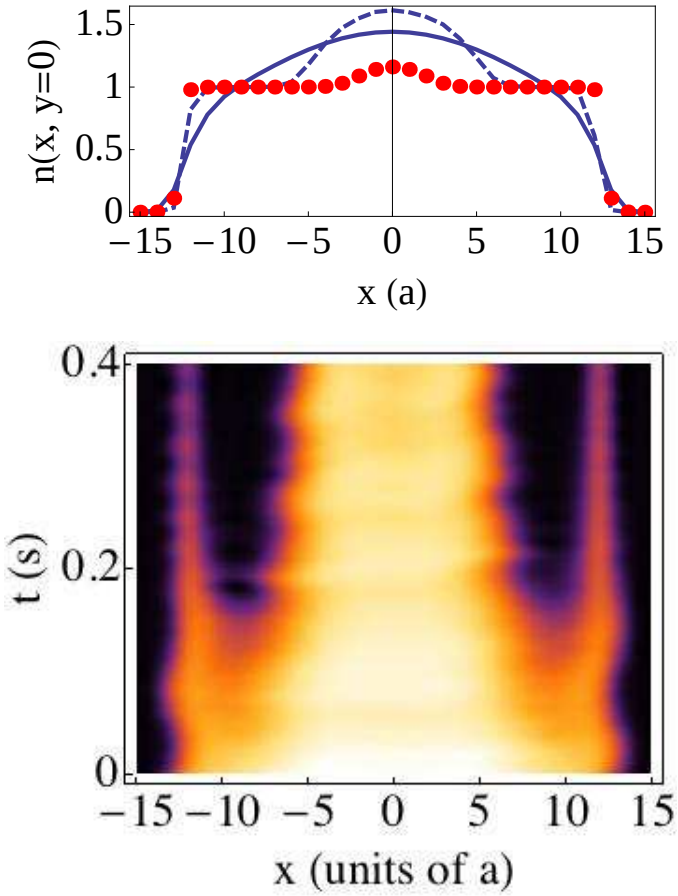

Figure 6.3: **Slow transport across Mott region** (Top) Evolution of an initial superfluid state (solid) at $V_i = 11E_R$ and $N = 500$ in a 25Hz radial trapping potential. Final density profile (dashed) after a ramp $\tau_r = 120 \times 2\pi/U_i \sim 400$ ms, is very different from the equilibrium state (dotted) at $V_f = 16E_R$. (Bottom) Density plot showing the time evolution of the coherences ($C_i \equiv -\langle a_i \rangle \sum_j \langle a_j^* \rangle$), a growing Mott region in the wings which cuts off transport in the intervening superfluid producing a non-equilibrium final state at late times. Brighter colors correspond to higher coherence.

central superfluid from the superfluid at the edge. In the Chicago experiment, [13], this Mott domain was $\sim$ 50 sites wide while in our simulations it is $\sim$ 8 sites.

As in the experiment, I find that after this ramp the density profile of the final

state (dashed line) is very different from the equilibrium state at V_f(dotted red), implying a relaxation time much longer the ramp time of 400ms. Indeed, further simulations show that it is longer than the experimental timescale of seconds. In the remainder of this Chapter I describe the cause of the slow equilibration, and conduct a number of additional simulations to illustrate how equilbration times depend on the various experimental parameters.

The major bottleneck for equilibration in Fig. 6.3 is mass transport across the Mott region. The Mott insulator is characterized by a gap to all excitations, as shown in Fig. 6.3 of order $\sim U$. Since particle transport is governed by hopping $J \ll U$, transport is strongly suppressed accross the Mott region.

To illustrate the spatial location of the Mott insulator, in Fig. 6.3(bottom) I plot the coherences $C_i \equiv -\langle a_i \rangle \sum_j \langle a_j^* \rangle$ as a function of time, where i, j denote nearest neighbor pairs. Mott regions ($C = 0$) show up as dark regions in the density plot. The Mott plateau widens over time, isolating the central superfluid. The peak atomic density in the initial lattice exceeds that of the equilibrium state at the final lattice depth. However the Mott region prevents mass flow from the center to the edge. The exponential suppression of transport through the Mott region was studied by Vishveshwara and Lannert [26].

6.5 Separation of Timescales for Global and Local equilibration

The numerical simulation in Fig. 6.3 is an excellent illustration of a situation where the timescale for global and local equilibration can be drastically differ-

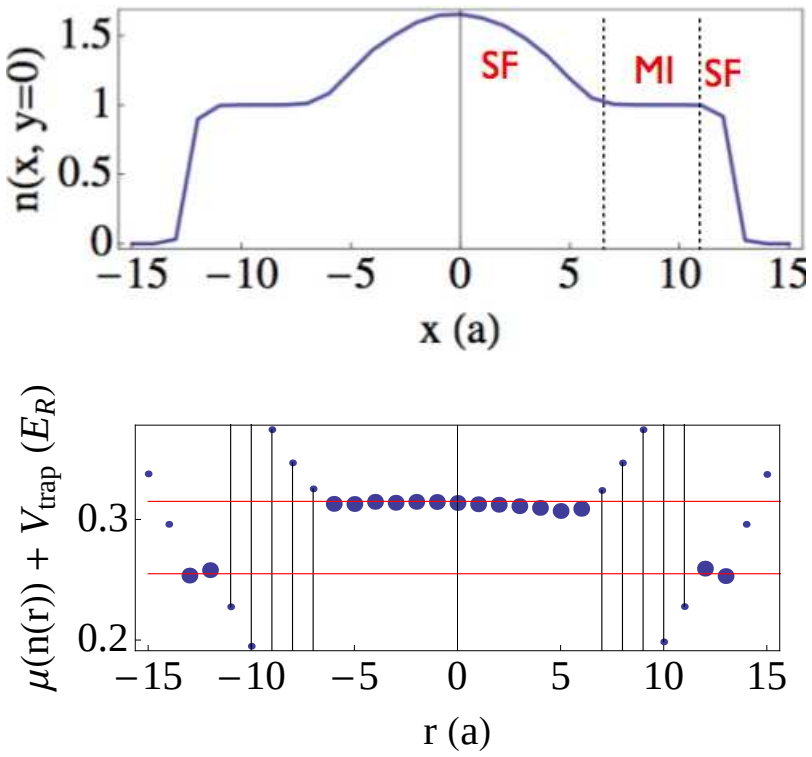

Figure 6.4: **Local versus Global equilibration** (Top) Shown is the final density profile (same as the dotted curve in Fig. 6.3 (top) for a ramp from $V_i = 11E_R$ to $V_f = 16E_R$ over a ramp time $\tau_r = 120 \times 2\pi/U_i \sim 400$ ms. The superfluid and Mott regions are clearly marked. (Bottom) Resulting equation of state for this profile showing local equilibration within the superfluid regions but absence of *global* equilibration after the quench.

ent even in small systems. To illustrate this, in Fig. 6.4 I plot the Gutzwiller equation of state ($\mu(\mathbf{r})$) corresponding to the *final* density profile following the ramp considered in Fig. 6.3. The density profile is plotted for comparison. If the system is in local equilibrium, the local density approximation (LDA) implies that $\mu(r) + V(r) = \mu_0$, a constant. Indeed as shown in the figure, this quantity is roughly constant within the two superfluid regions. However the two superfluid regions have *different* values of μ_0 even at long times, indicating the absence of global equilibration. This is due to the presence of the intervening Mott shell, indicated by the vertical lines.

6.6 Fast equilibration without transport

I conclude by showing that rapid *global* equilibration can be achieved if the trap parameters are chosen in a way as to minimize transport between intervening Mott shells. My results in this section are consistent with the Munich experiments [15]. The parameters are chosen to mimic the systems considered by Sherson *et al.* [15], which attained *global* equilibrium on timescales comparable to 100ms. Figure 6.5 shows the time-evolution of an initial state at $V_{\mathrm{i}} = 11$ at $N = 800$ in 2.5Hz trap, and a central chemical potential of $\mu = 1.4U$. I find that after an evolution of $\tau_{\mathrm{r}} = 25 \times 2\pi/U_{\mathrm{i}}$, the final profile (dashed) is close to the equilibrium $T = 0$ Gutzwiller prediction (dotted).

Despite the fact that the $n = 1$ Mott region is of similar size as Fig. 6.3, I find faster equilibration times in this system. The difference is that here parameters are chosen such that the total number of particles in the center is the same in the initial and final states. Thus no transport is needed across the Mott region.

6.7 Summary

My work in this chapter was motivated by three experiments. The Chicago experiments [13] have an extremely wide Mott region ($\sim$ 50 sites) inhibiting transport. I showed by smaller scale calculations that once the Mott shell is a significant fraction of the system size, the dynamics slow dramatically, leading to extremely long equilibration times observed in the experiment.

The Harvard experiments [14] have good evidence of local equilibrium on short timescales. I investigated this timescale by studying a homogenous sys-

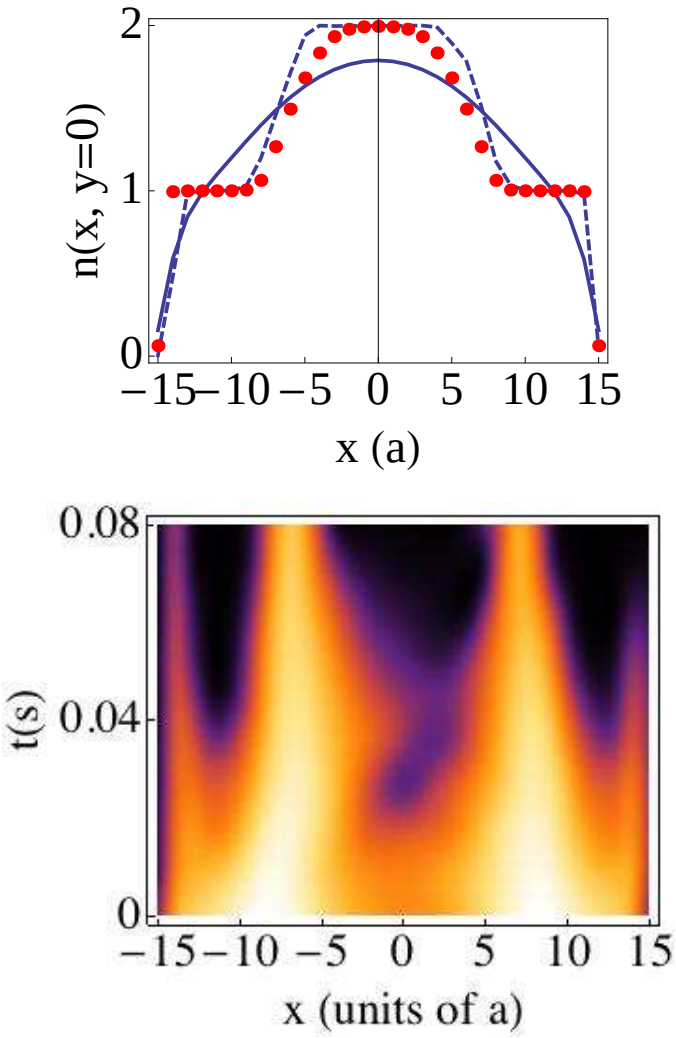

Figure 6.5: **Time-evolution at higher density**(Left): Evolution of an initial superfluid state for $V_{\rm i} = 11E_R$ and $N = 800$ (solid) in a 25Hz radial trapping potential in a linear ramp with $\tau_{\rm r} = 25{\times}2\pi/U_{\rm i} =$ 80ms. The dotted profile is the $T = 0$ equilibrium Gutzwiller profile at $V_0 = 16E_R$ for the same parameters. The final density profile (dashed) agrees with the $T = 0$ equilibrium Gutzwiller profile. (Right) Time evolution of the spatial coherence distribution, showing the formation of an $n = 1$ and $n = 2$ Mott plateaus. Lighter colors imply larger coherences. Cf. Fig.(2) in [15].

tem. One insight into the timescale for equilibration is that the lowest energy $k = 0$ single particle excitation has a gap $\sim U$. This energy scale appears to set the timescale for adiabaticity.

The Munich experiments [15] achieve equilibrium profiles after very short 75ms ($\sim J$) ramps. For the parameters I consider, my simulations reproduce this result. I attribute the difference between the Chicago and Munich observations to the greater amount of transport accross Mott regions required to reach equilibrium for the Chicago parameters.

The lesson for experiments is that by carefully choosing parameters, one can drastically reduce the adiabaticity timescales.

BIBLIOGRAPHY

[1] T. Kinoshita, T. Wenger and D. Weiss Nature **440** 900 (2006).

[2] L. E. Sadler, J. M. Higbie, S. R. Leslie, M. Vengalattore and D. M. Stamper-Kurn Nature **443** 312 (2006).

[3] S. Hofferberth, I. Lesanovsky, B. Fischer, T. Schumm and J. Schmiedmayer, Nature **449** 324-327 (2007).

[4] C. N. Weiler, T. W. Neely, D. R. Scherer, A. S. Bradley, M. J. Davis and B. P. Anderson Nature **455** 948 (2008).

[5] X.Du, L.Luo, B.Clancy, and J.E. Thomas, Phys. Rev. Lett. **101** 150401 (2008).

[6] M. Rigol, V. Dunjko and M. Olshanii Nature **452** 854 (2008).

[7] K. Sengupta, S. Powell and S. Sachdev, Phys. Rev. A **69** 053616 (2004).

[8] W. H. Zurek, U. Dorner, and P. Zoller, Phys. Rev. Lett. **95** 105701 (2005).

[9] A. Polkovnikov and V. Gritsev Nature Physics **4** 477 (2008).

[10] K. V. Krutitsky and P. Navez, Phys. Rev. A **84** 033602 (2011).

[11] V. Oganesyan, A. Pal and D. A. Huse, Phys. Rev. B **80** 115104 (2009).

[12] I. Bloch, J. Dalibard, and W. Zwerger, Rev. Mod. Phys. **80** 885 (2008).

[13] C-L. Hung, X. Zhang, N. Gemelke and C. Chin Phys. Rev. Lett. **104** 160403 (2010).

[14] W. S. Bakr, A. Peng, M. E. Tai, R. Ma, J. Simon, J. I. Gillen, S. Folling, L. Pollet and M. Greiner, Science **329** 547 (2010).

[15] J. F. Sherson, C .Weitenberg, M. Endres, M. Cheneau, I. Bloch and S. Kuhr Nature **467** 68 (2010).

[16] L. D. Landau, Phys. Z. Sowjetunion **2**, 46 (1932); C. Zener, Proc. R. Soc. Lond. A **137**, 696 (1932).

[17] M. Fisher, P. B. Weichman, G. Grinstein and D. S. Fisher, Phys. Rev. B **40** 546-570 (1989).

[18] D. Jaksch, C. Bruder, J. I. Cirac, C. W. Gardiner and P. Zoller, Phys. Rev. Lett. **81** 3108, (1998).

[19] W. Zwerger, J. Opt. B: Quantum Semiclass. **5** S9 (2003).

[20] C. Menotti and N. Trivedi, Phys. Rev. B **77** 235120 (2008).

[21] P. Navez, and R. Schutzhold, Phys. Rev. A **82** 063603 (2010).

[22] J. S. Bernier, G. Roux and C. Kollath, Phys. Rev. Lett. **106** 200601 (2011).

[23] W. H. Press, S. A. Teukolsky, W. T Vetterling and B. P. Flannery, *Numerical Recipes 3rd Edition: The Art of Scientific Computing* Cambridge University Press (2007).

[24] J. Wensdorfer, M. Snoek and W. Hofstetter, Phys. Rev. A **81** 043620 (2010).

[25] L. D. Landau and L. M. Lifshitz, *Quantum Mechanics Non-Relativistic Theory, Third Edition: Volume 3* Butterworth-Heinemann (1981).

[26] S. Vishveshwara and C. Lannert, Phys. Rev. A **78** 053620 (2008).

CHAPTER 7

EVOLUTION OF CONDENSATE FRACTION DURING RAPID LATTICE RAMPS

This Chapter was adapted from "Evolution of the condensate fraction during rapid lattice ramps", a collaboration with experimentalists David McKay and Prof. Brian DeMarco from the University of Illinois, at Urbana Champaign. The work is published in Physical Review A ***85*** *061601 (R) (2012). In this Chapter, i discuss the implications of understanding the timescales for local dynamics, discussed in the previous Chapter*

7.1 Introduction

A routine technique used to probe ultra-cold gases is to simply shut off all the lasers and observe the atoms in time-of-flight. By shutting off the light fields slowly or quickly compared to relevant microscopic scales in the atomic Hamiltonian, one gains access to different quantities. For example, by turning off the lattice over an appropriately chosen timescale, one can reconstruct the initial quasi-momentum distribution of the atoms from the time-of-flight images. This procedure is known as *bandmapping*. Here we use experiments and numerical simulations to investigate the accuracy of bandmapping as a probe of the momentum distribution of an interacting gas of atoms. We find that interactions lead to non-adiabiatic transfer of atoms between different momentum states, rendering bandmapping *unreliable*.

7.2 Lattice turn off experiment

Consider a non-interacting gas of atoms loaded into a cubic optical lattice with lattice spacing d. The Hamiltonian of the system in the lowest band of the optical lattice is given by:

$$\mathcal{H} = -t \sum_{\langle ij \rangle} (a_i^\dagger a_j + h.c) - \sum_i \mu_i a_i^\dagger a_i \tag{7.1}$$

where t denotes the tunneling energy, $\mu_i = \mu - V_{ex}(i)$ is the spatially dependent chemical potential and $V_{ex}(i) = \frac{1}{2} m\omega^2 i^2$ is the external harmonic confinement.

As discussed in Chapter 1 , in the absence of a trapping potential, the single particle eigenstates are given by Bloch wave-functions $\phi_{l,q} = u_{q,l} e^{iq.x}$, where q is the quasi-momentum, l denotes the band index and $u_{n,l}$ is a function with the periodicity of the lattice. One constructs the Wannier basis by taking a Fourier transform $w_{l,R} = \int dq e^{iq.R} \phi_{l,q}$. Even for shallow lattice depths, the Wannier states have nearly unity overlap with the local harmonic oscillator ground state.

For atoms loaded onto the lowest band of the optical lattice, the single-particle eigenstates in the presence of a parabolic confining potential can be expressed as a linear combination of the Wannier functions in the lowest band. For a shallow lattice, $t \gg \omega_{trap}$, the low energy eigenstates are approximately harmonic oscillator eigenstates separated by an energy $E = \hbar\omega_{trap} \sqrt{m/m^*}$ where the effective mass $m^* = \hbar^2/(2d^2 t)$. The precise eigenstates and eigen energies can be found in Refs. [1, 2].

Imagine an experiment where the lattice is suddenly switched off and the atoms are subsequently imaged following time of flight. There are three important timescales to consider for non-interacting atoms in a lattice potential. The hopping term in Eq. 7.1 is diagonal in momentum space. However as parti-

cles move around in the trapping potential, their potential energy is converted to kinetic and vice versa, leading to momentum redistribution on a timescale $\tau_{trap} = 1/\nu$ where $\nu = \omega/2\pi$. Finally there is the bandgap E_{bg} which leads to transfer of atoms between different bands on a timescale $\tau_{band} = h/E_{bg}$. Typically $\tau_{band} \ll \tau_{trap}$.

One can thus imagine turning off the lattice potential is three different ways: a) sudden turn off – where the lattice potential is turned off fast compared to τ_{band}, h/t and τ_{trap}, b) slow compared to τ_{band} but fast compared to τ_{trap} and finally (c) slow compared to τ_{trap} . In Fig. 7.2, I plot characteristic pictures resulting from each of these quenches.

If the lattice potential is turned off suddenly, the Bloch states simply get *projected* onto free particle states with momentum $p = \hbar(q+nk_{lat})$, where $k_{lat} = 2\pi/d$ is the reciprocal lattice vector in a cubic lattice, and n is an integer. This is because any Bloch state with quasi-momentum q can be expressed as a superposition of plane wave states with momenta $q + nk$. For atoms occupying a single Bloch state, such as Bose-Einstein condensate, the resulting time-of-flight images will show interference maxima.

A more useful procedure is to use (*b*) where the lattice is turned off slowly compared to the inverse band-gap but still fast compared to τ_{trap}. In this case, quasi-momentum is preserved and the Bloch state in the n-th band is adiabatically mapped onto a free-particle state in the n-th Brillouin zone. The resulting momentum distribution can be obtained from time-of-flight images. This procedure is known as *bandmapping*, and it allows one to probe the momentum distribution in the lattice [3]. Bandmapping has been used to measure condensate fraction [4], map Brillouin zone boundaries [5, 6], determine temperatures

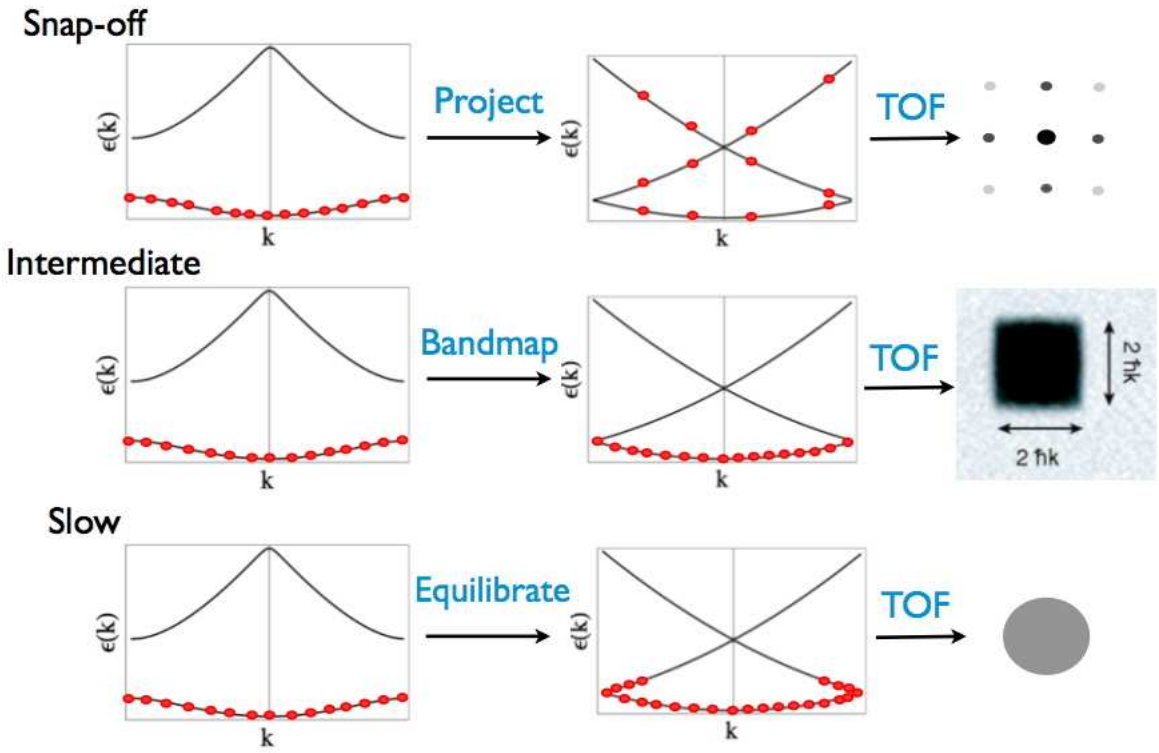

Figure 7.1: **Schematic of Lattice turn-off experiments in a non-interacting system** (Top): Following a sudden quench quasi-momentum states are projected onto free particle states producing an interference pattern following time of flight. (Center) Turning the lattice off adiabatially compared to the band spacing maps quasi-momentum to momentum. Image reproduced from Ref. [3]. (c) When the lattice is turned off adiabatically compared to the trap, atoms simply follow the harmonic oscillator ground state, and information about the initial momentum distribution is lost.

[1], and probe phase transitions [6, 7, 8].

In protocol (c) the lattice potential is turned off slowly compared to both τ_{band} and τ_{trap}, the atoms will adiabatically follow the harmonic oscillator ground state and all information about the initial momentum distribution will be lost.

In typical experiments $\tau_{band} \lesssim 0.1$ ms and $\tau_{trap} \gtrsim 10$ ms, making it easy to

satisfy the conditions for bandmapping. Typical ramp times for bandmapping experiments are $\tau \sim 1$ms.

Complications arise for an interacting gas. Interactions lead to a coherent redistribution of quasi-momentum occupations [9, 10, 11]. Furthermore, collisions scatter atoms between different quasi-momenta while conserving total quasi-momentum. The on-site interaction energy between two atoms U determines the relevant dynamical timescale h/U; in most experiments, $h/U \lesssim 1$ ms. We show that the additional criterion, $\tau \ll h/U$, disrupts the separation of timescales that makes bandmapping successful in noninteracting systems.

Using a combination of experiment and numerical simulations, we investigate the impact of interactions on bandmapping for atoms confined in a lattice in the strongly correlated regime. We quantify the redistribution of quasi-momentum during lattice ramps for a Bose-Einstein condensate of atoms in a 3D cubic optical lattice. The fraction of atoms in the condensate is determined after linearly ramping from lattice depth V_i (with $10E_R < V_i < 14E_R$, spanning the superfluid and Mott-insulator regimes) to a fixed final depth $V_f = 4E_R$. Here $E_R = (h/\lambda)^2/2m$ is the recoil energy, λ is the laser wavelength, and m is the atomic mass.

Here we focus on the redistribution of quasi-momentum within the ground band alone. We choose a final lattice depth of $V_f = 4E_R$ to minimize the transfer of atoms to higher bands to enable comparison with numerical simulations on the single-band Bose Hubbard model. As we show below, even for ramps terminating at $V_f = 4E_R$, there is considerable quasi-momentum redistribution. Within our statistical uncertainty, we find no difference in the measured relaxation time between ramps terminating at $V_f = 4E_R$ and $V_f = 0$. Provided the

interaction strength is smaller than the band spacing throughout the ramp, interaction driven inter-band transitions are suppressed and band populations are thus preserved [1]. Our results apply to interacting gases in general, including fermionic systems and mixtures.

7.3 Experimental Method

Our experimental setup is described in detail in Ref. [1], and we refer the reader to the the Supplementary Materials attached to the published version of the Chapter for a detailed description of the procedure used to analyze the images [12]. In summary, we create a condensate composed of ^{87}Rb atoms in the $|F = 1, m_F = -1\rangle$ state in a harmonic trap with (geometric) mean trap frequency $\bar{\nu}_0 = 35.78(6)$ Hz. We cool the gas until the condensate fraction exceeds 80%.

We superimpose a cubic optical lattice with a $d = \lambda/2 = 406$ nm lattice spacing on the atoms by slowly turning on three pairs of retro-reflected laser beams. The laser intensity determines the potential depth V. Through Kapitza-Dirac diffraction, we calibrate V to within 1%, but drift in the calibration results in a 6% systematic uncertainty. The Gaussian envelope of the lattice beams adds to the harmonic confinement, and the overall (geometric) mean trap frequency with the lattice on is $\bar{\nu} \approx \sqrt{\bar{\nu}_0^2 + \frac{8V_i}{(2\pi)^2 m w^2}}$, where $w = (120 \pm 10)\,\mu$m is the measured $1/e^2$ radius of the lattice laser beams.

Ten milliseconds after loading the lattice, we linearly ramp V from V_i to $V_f = 4\ E_R$ in time τ. The lattice and trapping potentials are then removed in 10 ns and 0.2 ms, respectively, and the column density is imaged after the gas expands for 20 ms. We extend the dynamic range of our measurement by imag-

ing only a controlled fraction of atoms that are transferred to the $F = 2$ hyperfine state. The number of condensate atoms N_c is measured using multimodal fits to "low optical density" images for which only a small number of atoms are transferred. We supplement these with "high optical density" images, for which all atoms are transferred and imaged. In these images, the broad non-condensate component is resolvable, but the condensate peaks are saturated (see Fig. 7.2). The number of non-condensate atoms is determined by fitting the broad background with the condensed peaks masked and extrapolating the non-condensate component into the masked regions. The total number of particles N varied from $(103 \pm 5) \times 10^3$ to $(72 \pm 2) \times 10^3$ for $V_i = 10\ E_R$ to $14\ E_R$, and the condensate fraction ranged from 0.3 to 0.05.

7.4 Experimental Results

For each V_i we measure the post-ramp condensate fraction as a function of τ. A typical data set is shown in Fig. 7.2 for $V_i = 10\ E_R$. The data points follow an exponential, as illustrated by the red curve. The fitted time constants τ_{rel} are shown in Fig. 7.3 as a function of the initial condensate fraction (bottom axis) along with the corresponding V_i (top axis). The relaxation time is relatively weakly dependent on V_i, only changing by a factor of two as the superfluid-Mott insulator transition is crossed, and throughout is consistent with the simple empirical rule $\tau_{\text{rel}} \propto 1/U$.

The insets to Fig. 7.2 shows the high optical density images for (a) short and (b) moderate ramps. Even for ramp times as short as 1ms, the quasi-momentum distribution changes dramatically, as the condensate fraction grows by a factor

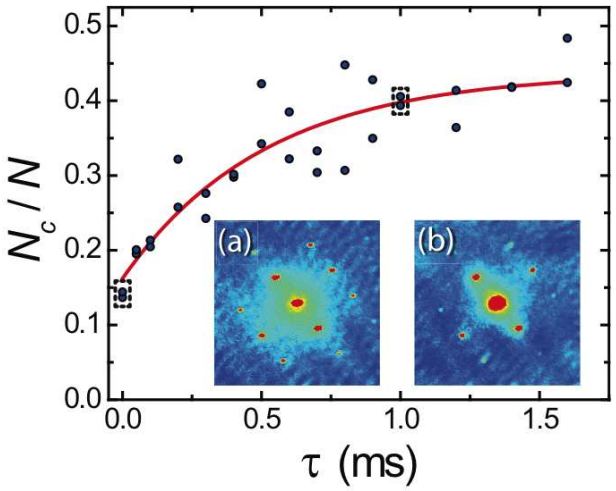

Figure 7.2: Condensate fraction measured after bandmapping from V_i = 10 E_R. The insets show high optical density images where the background is resolved, but the Bragg peaks are saturated. The images are shown in false color, with red (blue) indicating regions of high (low) column density. The field of view is $813 \times 813\ \mu$m. (a) τ = 10 ns; (b) τ = 1 ms.

of 2. This transfer of atoms from the non-condensate to the condensate represents a redistribution of atoms from high to low quasimomentum states. Most bandmapping experiments use $\sim$ 1 ms for τ, and therefore *do not* measure the initial condensate fraction. Shorter ramps are not a solution to this problem, as they lead to significant non-adiabatic transfer of atoms to higher energy states [**?**].

7.5 Theoretical Modeling

We use the 3D Bose Hubbard Hamiltonian introduced in Chapter 3 to model our system:

$$\mathcal{H} = -t \sum_{\langle ij \rangle} \left(a_i^\dagger a_j + h.c. \right) + \sum_i \left[\frac{U}{2} n_i (n_i - 1) - \mu_i n_i \right] \tag{7.2}$$

where a_i and $a_i^\dagger$ are bosonic annihilation and creation operators at lattice site i, and $\mu_i = \mu - V_{\rm ex}(i)$, where μ is the chemical potential and $V_{\rm ex}(i)$ is the external potential at site i. For the physics discussed here, the role of the trap is to provide spatial inhomogeneity, which leads to a spatially varying chemical potential and co-existing phases. The first sum in Eq. 1 is over all nearest neighbor sites. As discussed in Chapter 3, we calculate U using the exact Wannier functions in the lowest band, and extract the tunneling t from Mathieu characteristics.

We calculate dynamics using a time dependent Gutzwiller ansatz which was described in detail in Chapter 3. The wave-function becomes $\Psi = \bigotimes_i \sum_m c_m^{(i)}(\mathtt{t})|m\rangle_i$ where $|m\rangle_i$ is the m-particle Fock state on site i, and the coefficients $c_m^{(i)}(\mathtt{t})$ are space (i) and time ($\mathtt{t}$) dependent. (Note the typographic distinction between the tunneling t, time $\mathtt{t}$, and ramp time τ.) This approximation leads to a simplistic quasi-momentum distribution, dividing atoms into zero momentum ($k = 0$) condensed and $k \neq 0$ non-condensed states. The total number of condensed atoms N_c is given by $N_c = \sum_i |\langle a_i \rangle|^2$, where $\langle a_i \rangle = \sum_m \sqrt{m+1} c_{m+1}^{(i)} c_m^{(i)}$.

As in the experiment, the potential depth is ramped $V(\mathtt{t}) = V_i + (V_f - V_i)(\mathtt{t}/\tau)$, where V_i and $V_f = 4\ E_R$ are the initial and final lattice depths, and τ is the ramp time. The Hubbard parameters t and U are time-dependent because of this ramp. In the simulations we include a spherically symmetric external harmonic trapping potential V_{ex}, matched to the (lattice-depth-dependent) experimental value $\overline{\nu}$.

We make direct comparison with the experimental data by studying $N \sim 75,000$ ^{87}Rb atoms on a $55 \times 55 \times 55$ lattice with lattice spacing 406 nm. For our initial state we use a local density approximation obtained by solving the

homogenous, single-site problem. To account for the overestimation of the condensate fraction in mean-field theory, we use two different initial states to model the data. *Initial state* 1 is the mean-field ground state obtained by using the physical lattice depth V_i in the simulation. This state has a larger condensate fraction than the experimental initial state. *Initial state* 2 is obtained by finding the lattice depth at which the condensate fraction predicted by the theory matches the measured condensate fraction at V_i.

Time evolution, from either of these initial states, is calculated using a split-step approach with sequential site updates. We ramp the lattice down from V_i to $4E_R$ in a time τ ranging from 0 to 1.5 ms, and calculate the condensate fraction at the end of each ramp. We then fit the resulting data to an exponential curve to extract a characteristic relaxation time τ_{rel}.

The ramp time is shorter than the typical tunneling time h/t, therefore we do not expect any transport to occur in the system. On these short times, each site evolves approximately *independently* under the mean-field from its neighbors, which is determined by the initial state. This is analogous to a spin precessing under a local "magnetic field" arising from the exchange interaction with its neighbors. The precession is slower for smaller magnetic fields. Similarly, as initial state 1 has a larger local condensate fraction compared to initial state 2, we expect a shorter relaxation time for initial state 1 compared to initial state 2.

7.6 Comparison of Theory and Experiment

In Fig. 7.3 we compare two theoretical curves with the experimental data.

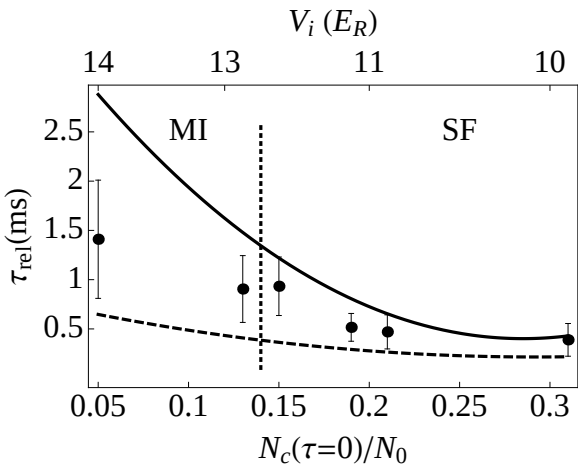

Figure 7.3: Relaxation time (τ_{rel}) for the condensate fraction for ramps from V_i to $V_f = 4E_R$ for variable ramp times τ. The range of V_i spans the superfluid (SF) and Mott insulator (MI) regimes (demarcated by the vertical dotted line). The experimental data is bounded by zero temperature Gutzwiller mean-field simulations using two different initial states (see text). The solid black line shows the relaxation time assuming initial state 2, while the dashed line shows the relaxation time assuming initial state 1. The error bars represent the uncertainty in the relaxation time from a fit to data such as that shown in Fig. 7.2

The bottom line is obtained from initial state 1, and the top line is obtained from initial state 2. Initial state 1 yields a *higher* condensate fraction compared to the experimental system at any given initial lattice depth. It relaxes to equilibrium faster, hence providing a *lower* bound on the characteristic relaxation time τ_{rel}.

Initial state 2 treats the atoms as if they were in a deeper lattice than the physical system. As a result, initial state 2 has slower dynamics and thus provides an *upper* bound on the characteristic relaxation time.

For $V_i \lesssim 13\ E_R$ both theoretical protocols yield similar results. Here the entire system is superfluid, and mean-field theory is accurate. Throughout this

regime $\tau_{\text{rel}} \sim 0.5$ms. As the superfluid-Mott transition is approached, the relaxation time increases by a factor of ~ 2, indicative of slower dynamics in the insulating state. The simulation using initial state 2 (top curve) captures this physics, showing a significant increase in relaxation time; initial state 2 contains a Mott-insulator shell. The growth of the relaxation rate from initial state 1 is more gradual, as the mean-field Mott-insulator transition occurs for larger values of V_i as compared to the experiment.

Our simulations used zero temperature initial states — finite temperature would modify the connection between condensate fraction and lattice depth, effectively raising the relaxation rate obtained from initial state 1.

7.7 Qualitative understanding of the timescale

Bandmapping timescales are too short for significant transport in the lattice to occur, and thus the observed physics is purely local. In order to gain a microscopic understanding for the $\sim ms$ timescale for quasi-momentum redistribution, we consider a homogeneous system with $V_{ex} = 0$. The experimentally observed timescale at a given lattice depth can be obtained by reintroducing the trap in terms of the local density approximation and averaging the results of different homogeneous systems.

Following the procedure outlined in Chapter 3 we linearize about the Gutzwiller ground state at a given lattice depth and obtain the excitation spectrum $\omega(k)$ for the lattice gas in the shallow and deep lattice limits. As shown in Fig. 7.4 (left), in the superfluid phase near the Mott-superfluid boundary, we find two modes: a low energy gapless phonon mode, with energy $\epsilon_{ph} \propto t$ and

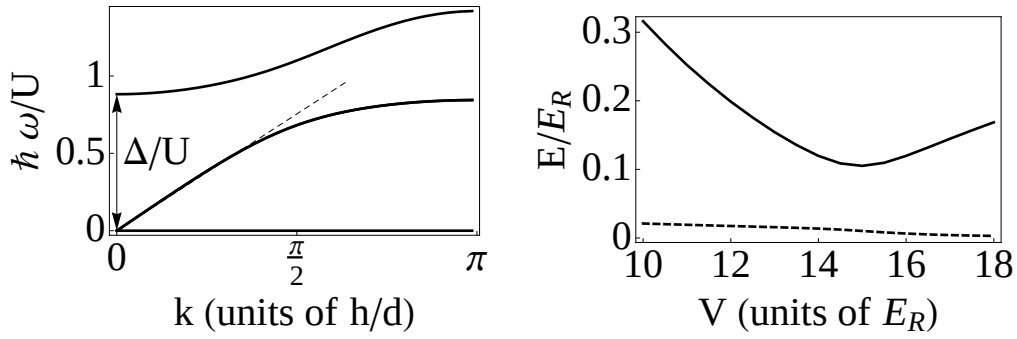

Figure 7.4: **Relevant energy scales in deep lattices** (Left): *Typical excitation spectrum of a superfluid near the Mott-insulator transition* ($V = 13E_R$). Two modes are present: a gapless phonon mode with a linear Bogoliubov (dashed) dispersion at low k, and a gapped particle-hole mode with quadratic dispersion. The gap $\Delta \sim U$, sets the diabaticity timescale for bandmapping. (Right): Energy scale of the phonon (ϵ_{ph} at $k = 0.2/d$) (dashed) and gap Δ at $n = 0.9$ as a function of lattice depth.

a gapped particle-hole like excitation, with a gap Δ. The typical energy scales corresponding to these modes is shown on the right for the experimental lattice depths. The ramp protocol used in bandmapping does not change the overall density, *i.e.* phonons are not excited. Therefore the relevant excitations are the gapped modes: ramps longer than h/Δ will be adiabatic.

We obtain a quantitative estimate for Δ by truncating the Fock basis to 2 particles per site and diagonalizing the resulting 3×3 Hamiltonian. The eigenvalues become particularly simple when $\mu \approx U/2$, for which we find that $\Delta = \frac{1}{4}(U + \sqrt{48z^2\langle a\rangle^2 t^2 + U^2})$, where z is the co-ordination number ($z = 6$ for a cubic lattice). In deep lattices, $\Delta \sim U \sim 0.1E_R$, and $h/\Delta \sim$ms (see Fig. 7.4).

7.8 Summary

We find that previous assumptions that dynamics are frozen during bandmapping are incorrect for interacting systems. Rather, we observe that considerable momentum redistribution occurs for typical bandmapping times, driven by interactions. This renders bandmapping unreliable for measuring quasi-momentum distributions in interacting systems. This problem could be circumvented by turning off interactions prior to bandmapping using a Feshbach resonance. As long as the interactions remain weaker than the band spacing throughout the ramp, bandmapping remains an accurate probe for measuring band populations.

BIBLIOGRAPHY

[1] D. McKay, M. White and B. DeMarco, Phys. Rev. A **79**, 063605 (2009).

[2] A.M. Rey, G. Pupillo, C. W. Clark, and C.J. Williams. Phys. Rev. A **72**, 033616 (2005).

[3] M. Greiner, I. Bloch, O. Mandel, T. W. Hansch and T. Esslinger Phys. Rev. Lett. **87**, 160405 (2001).

[4] M. Pasienski, D. C. McKay, M. White and B. DeMarco Nature Physics **6**, 677 (2010).

[5] T. Rom, T. Best, D. van Oosten, U. Schneider, S. Folling, B. Paredes and I. Bloch Nature (London) **444**, 733 (2006); T. Müller, S F.ölling, A Widera and I. Bloch, Phys. Rev. Lett. **99** 200405 (2007).

[6] U. Schneider, L. Hackermuller, S. Will, T. Best, I. Bloch, T. A. Costi, R. W. Helmes, D. Rasch and A. Rosch Science **322**, 5907 (2008).

[7] I.B. Spielman, W. D. Phillips and J. V. Porto, Phys. Rev. Lett. **100**, 120402 (2008).

[8] M. White, M. Pasienski, D. McKay, S. Q. Zhou, D. Ceperley, and B. DeMarco, Phys. Rev. Lett. **102**, 055301 (2009).

[9] S. S. Natu and E. J. Mueller arXiv: 1201.6674 (2012);

[10] P. Barmettler, D. Poletti, M. Cheneau and C. Kollath, Phys. Rev. A **85** 053625 (2012).

[11] M. Rigol and A. Muramatsu, Phys. Rev. Lett. **93** 230404 (2004).

[12] S. S Natu, D. C McKay, B. DeMarco and E. J .Mueller, Phys. Rev. A **85** 061601 (R) (2012).

APPENDIX A

BASIC SCATTERING THEORY

In this appendix I will briefly remind the reader of the basic ideas in scattering theory that are used in Chapter 1 to understand how ultra-cold gases interact. I refer the reader to the PhD thesis of Erich J. Mueller for an excellent discussion of scattering theory [1].

Consider the scattering of two particles of mass m interacting with a spherically symmetric interaction $V(r)$, which decays as to zero in a manner such that $rV(r) \to 0$ as $r \to \infty$. The center of mass wave-function of the particle is described by a plane wave, while the relative wave-function can be expressed as a sum of an incoming plane wave and a scattered wave [2]

$$\psi(\mathbf{r}) = e^{ikz} + \psi_{sc} \tag{A.1}$$

where ψ_{sc} is the scattered wave.

While the detailed form of ψ_{sc} depends on the nature of the potential, its asymptotic form can be deduced by noting that the potential falls off as $r \to \infty$ and so ψ_{sc} must obey the free particle Schrodinger equation at large distances *i.e*

$$(\nabla_r^2 + k^2)\psi_{sc} = 0 \qquad r \to \infty \tag{A.2}$$

or

$$\psi_{sc} \sim f(\theta, k)\frac{e^{ikr}}{r} \qquad r \to \infty \tag{A.3}$$

where $f(\theta)$ is the scattering amplitude.

To see this consider the solution to the free particle problem $V(r) = 0$:

$$\psi_{sc} = \sum_l \Big(A_l j_l(kr) + B_l n_l(kr)\Big)Y_l(\theta) \tag{A.4}$$

where Y_l are the spherical harmonics, and j_l and n_l are the Bessel and Neumann functions which behave as

$$j_l(kr) \to \sin(kr - l\pi/2)/(kr) \tag{A.5}$$
$$n_l(kr) \to -\cos(kr - l\pi/2)/(kr)$$

Forcing the outgoing wave at $r \to$ to be right going fixed $A_l/B_l = -i$.

This expansion yields the definition of the scattering amplitude $f(\theta)$

$$f(\theta) = \sum_l (-i)^l(-B_l)P_l(\theta) \tag{A.6}$$

where we have replaced the Y_l with Legendre polynomials $P_l(\theta) =$

The physical significance of B_l is the followin: angular momentum is conserved, thus each l state scatters independently. Thus the B_l is a measure of the scattering in a given angular momentum channel. For $V = 0$, expanding the incoming plane wave in terms of spherical harmonics one finds $B_l = (2l + 1)/k$.

How does the picture change in the presence of a potential? The amazing thing is that although the short range details of the potential may be extremely complicated, the asymptotics of the wave-function are remarkably simple, provided the potential decays smoothly to zero as assumed. One thus has that at large distances, the scattered wave still satisfies basically the free particle Schrodinger equation, with the only caveat that one must now add a phase shift δ_l to the asymptotic solutions Eq. A.5.

This implies that the only change to the scattering amplitude in the presence of a potential is:

$$f(\theta) = \sum_l i^l \frac{(2l + 1)e^{i\delta_l}}{k} P_l(\theta) \tag{A.7}$$

Therefore the scattering problem is reduced to a problem of finding the correct phase shifts.

The scattering cross-section σ is obtained by integrating the differential cross-section over all solid angles. Since the differential cross-section is the amplitude of scattering at a given angle one has that

$$\begin{aligned} d\sigma/d\Omega &= |f(\theta)|^2 && \text{distinguishable particles} \\ d\sigma/d\Omega &= |f(\theta) + f(\pi-\theta)|^2 && \text{identical bosons} \\ d\sigma/d\Omega &= |f(\theta) - f(\pi-\theta)|^2 && \text{identical fermions} \end{aligned} \tag{A.8}$$

Therefore one finds

$$\sigma = 2\pi \int d\theta |f(\theta)|^2 = \frac{4\pi}{k^2} \sum_0^\infty (2l+1)\sin^2(\delta_l) \tag{A.9}$$

where the orthogonality of the Legendre polynomials has been used.

How does one find the phase shifts for a given potential? In order to do this, one must connect the scattering amplitude to the potential. To do so, one observes that the wave-function ψ obeys the integral equation

$$\psi_k(\mathbf{r}) = e^{ikr} + \frac{2m}{\hbar^2} \int G^0(\mathbf{r},\mathbf{r}')V(\mathbf{r}')\psi_k(\mathbf{r}')dr' \tag{A.10}$$

where the free particle Green's function $G^{(0)}(\mathbf{r},\mathbf{r}') \sim 1/(4\pi)e^{i\mathbf{k}\cdot|\mathbf{r}-\mathbf{r}'|}/|\mathbf{r}-\mathbf{r}'|$. Note that Eq. A.10 is identical to the T-matrix approach described in Chapter 1. The T-matrix is simply a more formal way of expressing the above relation.

Now taking the long distance limit, and expanding the term $e^{i\mathbf{k}\cdot|\mathbf{r}-\mathbf{r}'|}/|\mathbf{r}-\mathbf{r}'|$ in the limit $r \to \infty$, and comparing the result with Eq. A.3 one finds that

$$f(k) = \frac{4\pi m}{\hbar^2} \int V(\mathbf{r}')\psi_k(\mathbf{r}')dr' \tag{A.11}$$

To get some physical intuition for f, consider the Born approximation where one replaces ψ_k with its free value e^{ikr}. One thus sees that the scattering amplitude within the Born approximation is nothing but the Fourier transform of the potential. In general one can expand the potential $V(r)$ into a sum of partial waves and obtain $f(\theta, q)$ and hence the corresponding phase shifts.

In general one finds that for a potential decaying as r^{-n}, the partial waves scale as $\delta_l \sim k^{2l+1}$ for small k and $l < (n-3)/2$ [3]. Therefore, higher partial wave contributions vanish extremely rapidly at small $k \ll k_c$ where the cutoff in momentum is set by the range of the potential $k_c = 2\pi/r_0$. For the van der Waals potential, the natural cutoff is set by the range of the potential $r_0 \sim 100a_0$. This sets an energy scale of $E_r = \hbar^2 k_c^2/2m$ ~mK. Thus for typical cold atom temperatures of $T \lesssim \mu$K, there is no scattering in higher partial wave channels and the dominant contribution to scattering comes from the s-wave channel, justifying the s-wave approximation made throughout the Chapter.

In the s-wave limit, one finds that within the Born approximation, Eq. A.11 yields $f(\theta) = a$, a constant. Therefore one finds that the total scattering cross-section for identical bosons is $8\pi a^2$ while that for identical fermions is 0. Therefore identical fermions *do not* interact in the s-wave channel.

At large r, one thus approximates the wave-function as

$$\psi = A\Big(1 - \frac{a}{r}\Big) \tag{A.12}$$

where the normalization A which depends on the details of the interaction potential.

BIBLIOGRAPHY

[1] Erich J. Mueller, PhD Thesis, University of Illinois, Urbana Champaign (2001).

[2] R. Shankar *Principles of Quantum Mechanics* (Plenum Press, New York 1980).

[3] C.J.Pethick and H.Smith, *Bose-Einstein Condensation in Dilute Gases* (Cambridge University Press, 2002).

APPENDIX B

COLLISIONLESS BOLTZMANN EQUATION

B.0.1 The Basic Setup

Here I derive a collisionless Boltzmann equation for a harmonically trapped two component Fermi gas, within a Hartree-Fock mean-field theory. Our system consists of the two component Fermi gas, ^{6}Li, trapped in the lowest two hyperfine levels, henceforth denoted by $\uparrow$ and $\downarrow$. I introduce the fermionic creation and annihilation operators $\Psi_s^\dagger(r,t)$ and $\Psi_s(r,t)$ for a fermion of spin $\sigma \in (\uparrow,\downarrow)$. The Hamiltonian for the system is given by

$$\hat{H}(t) = \sum_{\sigma=\uparrow,\downarrow} \int d\mathbf{r}\, \Psi_\sigma^\dagger(\mathbf{r},t)\left(-\frac{1}{2m}\nabla_{\mathbf{r}}^2 + U_\sigma(\mathbf{r})\right)\Psi_\sigma(\mathbf{r},t) + \tag{B.1}$$
$$\int d\mathbf{r}_1 \int d\mathbf{r}_2 \Psi_\uparrow^\dagger(\mathbf{r}_1,t)\Psi_\downarrow^\dagger(\mathbf{r}_2,t)V_{int,\uparrow,\downarrow}(\mathbf{r}_1-\mathbf{r}_2)\Psi_\downarrow(\mathbf{r}_2,t)\Psi_\uparrow(\mathbf{r}_1,t),$$

where $U_s(r)$ is the spin dependent trapping potential felt by the atoms. In addition, atoms with different S_z, interact with a contact potential $V_{int,\uparrow,\downarrow}$ of the form $\frac{4\pi a}{m}\delta^3(r_1 - r_2)$, where a is the scattering length, which can be positive or negative. We define $g = \frac{4\pi a}{m}$. The applied magnetic field is tuned such that the scattering length is near the zero crossing. Interactions between atoms with the same S_z are forbidden by the Pauli principle. I set $\hbar = 1$ throughout and we work in a Larmor frame rotating at the hyperfine frequency of the $\downarrow \rightarrow \uparrow$ transition for a uniform gas.

The dynamics of the system is governed by the Heisenberg equation of mo-

tion $\imath\frac{\partial}{\partial t}\hat{O}(\mathbf{r},t) = [\hat{O}(\mathbf{r},t), \hat{H}(t)]$. We have four Heisenberg equations of motion

$$\imath\frac{\partial\Psi_\sigma(\mathbf{r},t)}{\partial t} = \left(-\frac{1}{2m}\nabla^2_{\mathbf{r}} + U_\sigma(\mathbf{r})\right)\Psi_s(\mathbf{r},t) + g\Psi^\dagger_{\sigma'}(\mathbf{r},t)\Psi_{\sigma'}(\mathbf{r},t)\Psi_\sigma(\mathbf{r},t), \tag{B.2}$$

$$\imath\frac{\partial\Psi^\dagger_\sigma(\mathbf{r},t)}{\partial t} = -\left(-\frac{1}{2m}\nabla^2_{\mathbf{r}} + U_\sigma(\mathbf{r})\right)\Psi^\dagger_\sigma(\mathbf{r},t) - g\Psi^\dagger_\sigma(\mathbf{r},t)\Psi^\dagger_{\sigma'}(\mathbf{r},t)\Psi_{s'}(\mathbf{r},t),$$

where $s \neq s^{'}$. In the form above, it is clear that the equations of motion for the creation operators are simply complex conjugates of those for the corresponding annihilation operators.

B.0.2 The Boltzmann equation

Next, I express the density matrix in terms of a Wigner function, which is the quantum analog of the classical distribution function. In the final form, I will obtain the Landau-Vlasov equations for these Wigner functions. I introduce the following notation

$$f_{\sigma,\sigma'}(\mathbf{p},\mathbf{R},t) = \int d\mathbf{r}\exp(-\imath\mathbf{p}\cdot\mathbf{r})\langle\Psi^\dagger_\sigma(\mathbf{R}-\frac{\mathbf{r}}{2},t)\Psi_{\sigma'}(\mathbf{R}+\frac{\mathbf{r}}{2},t)\rangle, \tag{B.3}$$

where $f_{\sigma,\sigma'}$ is the Wigner function expressed as a function of the momentum ($\mathbf{p}$), center of mass coordinate ($\mathbf{R}$) and time. The integration variable is the relative coordinate $\mathbf{r} = \mathbf{r}_2 - \mathbf{r}_1$, where $\mathbf{r}_1$ and $\mathbf{r}_2$ denote the positions where an σ spin is created, and $\sigma^{'}$ spin is annihilated respectively. It is clear then that the average up-spin density at any point in space-time, $s_\uparrow(\mathbf{R},t) = \langle\Psi^\dagger_\uparrow(\mathbf{R},t)\Psi_\uparrow(\mathbf{R},t)\rangle = \int\frac{d\mathbf{p}}{(2\pi)^3}f_{\uparrow,\uparrow}(\mathbf{p},\mathbf{R},t)$, and analogously for the down spins. This definition is valid when the wavelength associated with variations in the potential is much larger than any microscopic length in the problem. Furthermore, the scattering lengths are tuned near zero, the interactions are short range, validating the Boltzmann description of transport.

As in Chapter 2, I define $s_\pm = \langle \Psi^\dagger_{\uparrow/\downarrow}(\mathbf{R},t)\Psi_{\downarrow/\uparrow}(\mathbf{R},t)\rangle = \int \frac{d\mathbf{p}}{(2\pi)^3} f_{\uparrow/\downarrow,\downarrow/\uparrow}(\mathbf{p},\mathbf{R},t)$. Higher moments of the Wigner functions give the spin current and the energy. It is useful to define $\mathbf{j}_{\uparrow/\downarrow}(\mathbf{R},t) = \int \frac{d\mathbf{p}}{(2\pi)^3}\frac{\mathbf{p}}{m} f_{\uparrow/\downarrow,\uparrow/\downarrow}(\mathbf{p},\mathbf{R},t)$ and $\mathbf{j}_\pm(\mathbf{R},t) = \int \frac{d\mathbf{p}}{(2\pi)^3}\frac{\mathbf{p}}{m} f_{\uparrow/\downarrow,\downarrow/\uparrow}(\mathbf{p},\mathbf{R},t)$. The off-diagonal components of the spin density matrix correspond to the spin raising and lowering operators in quantum mechanics. In terms of s_x and s_y, these are defined as $s_\pm = s_x \pm \imath s_y$. One can define j_x and j_y analogously. Finally, we define a total spin density as $s = s_\uparrow + s_\downarrow$, a z spin density $s_z = \frac{s_\uparrow - s_\downarrow}{2}$, and a z spin current $\mathbf{j}_z = \frac{\mathbf{j}_\uparrow - \mathbf{j}_\downarrow}{2}$.

I will also write down dynamical equations for the x-, y-, and z- spin densities and currents. Obtaining the Vlasov equations is now straightforward within a Hartree-Fock mean field description. Taking time derivatives of $\langle \Psi^\dagger_\sigma(\mathbf{r}_1,t)\Psi_{\sigma'}(\mathbf{r}_2,t)\rangle$, and using Eq. B.2 we get

$$\left(\frac{\partial}{\partial t} + \frac{\mathbf{p}}{m}\cdot\nabla_\mathbf{R} - \nabla_\mathbf{R} U_{\sigma,eff}(\mathbf{R})\cdot\nabla_\mathbf{p}\right) f_{\sigma,\sigma}(\mathbf{p},\mathbf{R},t) = -\imath g(s_\pm(\mathbf{R}) f_{\sigma',\sigma}(\mathbf{p},\mathbf{R},t) - s_\mp(\mathbf{R}) f_{\sigma,\sigma'}(\mathbf{p},\mathbf{R},t)) - \frac{g}{2}\left(\nabla_\mathbf{R} s_\pm\cdot\nabla_\mathbf{p} f_{\sigma',\sigma}(\mathbf{p},\mathbf{R},t) + \nabla_\mathbf{R} s_\mp\cdot\nabla_\mathbf{p} f_{\sigma,\sigma'}(\mathbf{p},\mathbf{R},t)\right). \tag{B.4}$$

where $\sigma \neq \sigma'$ and the effective potential $U_{\sigma,eff}(\mathbf{R}) = U_\sigma(\mathbf{R}) + g s_{\sigma'}(\mathbf{R},t)$. The density matrix is Hermitian. This implies that $f_{\downarrow,\uparrow} = f^*_{\uparrow,\downarrow}$, and so it suffices to write down only one of the equations.

$$\begin{aligned}\left(\frac{\partial}{\partial t} + \frac{p}{m}\cdot\nabla_\mathbf{R} - \frac{1}{2}\nabla_\mathbf{R}(U_{\uparrow,eff}(\mathbf{R}) + U_{\downarrow,eff}(\mathbf{R}))\cdot\nabla_\mathbf{p}\right) f_{\uparrow,\downarrow}(\mathbf{p},\mathbf{R},t) &= \\ -\imath(U_{\downarrow,eff}(\mathbf{R}) - U_{\uparrow,eff}(\mathbf{R})) f_{\uparrow,\downarrow}(\mathbf{p},\mathbf{R},t) - \imath g s_\pm(\mathbf{R})(f_{\downarrow,\downarrow}(\mathbf{p},\mathbf{R},t) - f_{\uparrow,\uparrow}(\mathbf{p},\mathbf{R},t)) \\ -\frac{g}{2}\nabla_\mathbf{R} s_\pm(\mathbf{R})\cdot(\nabla_\mathbf{p} f_{\downarrow,\downarrow}(\mathbf{p},\mathbf{R},t) + \nabla_\mathbf{p} f_{\uparrow,\uparrow}(\mathbf{p},\mathbf{R},t)).\end{aligned} \tag{B.5}$$

These equations can be expressed compactly in matrix notation as follows:

we define the Wigner matrix as

$$\overleftrightarrow{\mathbf{F}} = \begin{pmatrix} f_{\uparrow\uparrow}(\mathbf{p},\mathbf{R},t) & f_{\uparrow\downarrow}(\mathbf{p},\mathbf{R},t) \\ f_{\downarrow\uparrow}(\mathbf{p},\mathbf{R},t) & f_{\downarrow\downarrow}(\mathbf{p},\mathbf{R},t) \end{pmatrix} \tag{B.6}$$

Then Eqs. B.4 and B.5 become

$$\frac{\partial}{\partial t}\overleftrightarrow{\mathbf{F}} + \frac{\mathbf{p}}{m}\cdot\nabla_{\mathbf{R}}\overleftrightarrow{\mathbf{F}} = \imath[\overleftrightarrow{\mathbf{V}}, \overleftrightarrow{\mathbf{F}}] + \frac{1}{2}\{\nabla_{\mathbf{R}}\overleftrightarrow{\mathbf{V}}, \nabla_{\mathbf{p}}\overleftrightarrow{\mathbf{F}}\}, \tag{B.7}$$

where the potential matrix is

$$\overleftrightarrow{\mathbf{V}} = \begin{pmatrix} U_{\uparrow}^{eff} & -gs_{+} \\ -gs_{-} & U_{\downarrow}^{eff} \end{pmatrix} \tag{B.8}$$

The spin segregation effect comes about due to the fact that the up and down spin atoms feel slightly different potentials. It is customary to define the z-direction as longitudinal and the $x-y$ plane as transverse. Suppose we start with an atom spin polarized in the transverse direction. If there is an external field in the z-direction, it will cause the atom's spin to precess in the x-y plane. Now consider two such atoms, experiencing slightly different longitudinal magnetic fields. Their spins will precess differently, so even if they started out in the same quantum state, they will no longer remain in the same state after a short time. Once they are in different states, they can interact. Since the interaction preserves the total spin of the atoms, which is also in the transverse direction, their spins will now precess about the total spin, thereby generating a longitudinal spin component, even if there was none to start with.

The conservation of particles and total magnetization implies that the total density and s_z obey the usual continuity equation. However the spin densities in the x- and y- directions also obey a continuity equation with a source term, which comes from the fact that the magnetic field is different for $\uparrow$ and $\downarrow$.

B.0.3 Equations of Motion for Moments of the Wigner function

The equations obeyed by the densities and the currents can be obtained by taking various moments of the Vlasov equation. The zeroth moment gives

$$\begin{aligned} \frac{\partial}{\partial t} s_z + \nabla_{\mathbf{R}} \cdot \mathbf{j}_z &= 0 \\ \frac{\partial}{\partial t} s_x + \nabla_{\mathbf{R}} \cdot \mathbf{j}_x &= (U_\downarrow(\mathbf{R}) - U_\uparrow(\mathbf{R})) s_y \\ \frac{\partial}{\partial t} s_y + \nabla_{\mathbf{R}} \cdot \mathbf{j}_y &= (U_\uparrow(\mathbf{R}) - U_\downarrow(\mathbf{R})) s_x \end{aligned} \tag{B.9}$$

where we must bear in mind that the potential is not the 'effective potential', rather the bare potential without the mean field term.

Taking the first moment gives the analogous equation for the spin current. We make the vector form the spin current explicit by introducing a superscript $\nu \in (1, 2, 3)$ to represent spatial indices. This is not to be confused with the *x*-,*y* and *z* labels of the spin.

$$\begin{aligned} \frac{\partial}{\partial t} j_z^\nu + \nabla_{\mathbf{R}}^\mu \left(T_{\mu,\uparrow}^\nu - T_{\mu,\downarrow}^\nu \right) + \frac{1}{2m} \left(\nabla_{\mathbf{R}}^\nu U_{eff,\uparrow} s_\uparrow(\mathbf{R}) - \nabla_{\mathbf{R}}^\nu U_{eff,\downarrow} s_\downarrow(\mathbf{R}) \right) &= -2g(s \times j)_z^\nu \\ \frac{\partial}{\partial t} j_x^\nu + \frac{1}{m} \nabla_{\mathbf{R}}^\mu \left(T_{\mu,\uparrow,\downarrow}^\nu + T_{\mu,\downarrow,\uparrow}^\nu \right) + \nabla_{\mathbf{R}}^\nu (U_{eff,\uparrow} + U_{eff,\downarrow}) s_x &= \\ (U_\downarrow - U_\uparrow) j_y^\nu - 2g(s \times j)_x^\nu + \frac{1}{2m} g \, s \nabla_{\mathbf{R}}^\nu s_x & \\ \frac{\partial}{\partial t} j_y^\nu - \imath \nabla_{\mathbf{R}}^\mu (T_{\mu,\uparrow,\downarrow}^\nu - T_{\mu,\downarrow,\uparrow}^\nu) + \frac{1}{2m} \nabla_{\mathbf{R}}^\nu (U_{eff,\uparrow} + U_{eff,\downarrow}) s_y & \\ -(U_\downarrow - U_\uparrow) j_x^\nu - 2g(s \times j)_y^\nu + \frac{1}{2m} g \, s \nabla_{\mathbf{R}}^\nu s_y & \end{aligned}$$

where I have defined the stress tensor $T_{\mu,\sigma,\sigma'}^\nu(\mathbf{R}, t) = \int d\mathbf{p} \frac{p^\nu p_\mu}{2m} f_{\sigma,\sigma'}(\mathbf{p}, \mathbf{R}, t)$ and $T_{\mu,\sigma}^\nu(\mathbf{R}, t) = T_{\mu,\sigma,\sigma}^\nu(\mathbf{R}, t)$. Note that the equations for j_x and j_y can be further simplified by observing that the $T_{\mu,\uparrow,\downarrow}^\nu + T_{\mu,\downarrow,\uparrow}^\nu = 2\,\Re(T_{\mu,\uparrow,\downarrow}^\nu)$ and $T_{\mu,\uparrow,\downarrow}^\nu - T_{\mu,\downarrow,\uparrow}^\nu = 2\,\Im(T_{\mu,\uparrow,\downarrow}^\nu)$, once again from the Hermiticity of the spin density matrix.

APPENDIX C

KADANOFF-BAYM APPROACH TO THE BOLTZMANN EQUATION

In this Appendix I derive the Boltzmann equation using the Green's function equations of motion approach developed by Kadanoff and Baym [1]. I extend my results from the previous Appendix, by going beyond a Hartree-Fock mean field description. In particular, I expand the potential to second order in the interaction strength, which adds a collision term to the Boltzmann equation.

I begin by introducing the non-equilibrium Green's functions and write down the equations of motion for the single particle Green's functions in terms of the two particle Green's function. By introducing the self-energy, I then develop a diagrammatic perturbation theory using the ladder approximation, that is valid for short-range interactions [2]. It is these second order terms in the ladder approximation give rise to the collision integral. Using the prescription in [1] to obtain the Wigner functions from the Green's functions and obtain the resulting Boltzmann equation. Once we derive the collision integral, I consider two limits: highly non-degenerate gas, and degenerate gas. In each of these limits, we can apply a sequence of approximations that simplify the collision term. Finally we obtain a collision integral for a cloud whose dynamics is restricted to one-dimension, which is the weak direction of harmonic confinement, the axial direction.

C.0.4 Non-equilibrium Green's functions

I define the spin dependent single particle temperature Green's function $G_{\sigma,\sigma'}(\mathbf{r},\tau,\mathbf{r}',\tau') = -\mathrm{Tr}\{\hat{\rho}T_\tau[\Psi_\sigma(\mathbf{r},\tau)\Psi^\dagger_{\sigma'}(\mathbf{r}',\tau')]\}$, [2] where I have introduced "imag-

inary time" $\tau = \imath t$ which ranges from 0 to $\imath\beta$ and T is the time ordering operator, which orders the operators in [ ] according to the rule: earlier time acts first, or the operator acting at a later time is on the left, with the condition that an odd permutation of fermionic operators introduces a − sign. The operator $\hat{\rho}$ is a statistical weight of the usual form $\frac{1}{\mathrm{Tr}(\exp(-\beta\hat{H}))}\exp(-\beta\hat{H}) = \frac{1}{Z}\exp(-\beta\hat{H})$, where Z is the partition function from statistical mechanics. The physical interpretation of the Tr operator in the definition of G is that it is a sum over states in the Hilbert space weighted by a Boltzmann factor. It is implicitly assumed that the Ψ's are expressed in the interaction picture.

In imaginary time, the Heisenberg equation of motion takes the form $-\frac{\partial}{\partial t}\hat{O}(\mathbf{r},\tau) = [\hat{O}(\mathbf{r},\tau), \hat{H}(\tau)]$, and so from Eq. B.1 we obtain the following equations of motion for the single particle Green's functions:

$$\left(-\frac{\partial}{\partial\tau} + \frac{\nabla^2_{\mathbf{r}}}{2m} - U_\sigma(\mathbf{r},\tau)\right) G_{\sigma,\sigma'}(\mathbf{r},\tau,\mathbf{r}',\tau') - g\, G_{\sigma,\alpha,\sigma',\alpha}(\mathbf{r},\tau,\mathbf{r},\tau;\mathbf{r}',\tau',\mathbf{r},\tau^+) = \delta(\mathbf{r}-\mathbf{r}')\delta(\tau-\tau')\delta_{\sigma,\sigma'}, \quad \text{(C.1)}$$

and the adjoint equation of motion

$$\left(\frac{\partial}{\partial\tau'} + \frac{\nabla^2_{\mathbf{r}'}}{2m} - U_{\sigma'}(\mathbf{r}',\tau')\right) G_{\sigma,\sigma'}(\mathbf{r},\tau,\mathbf{r}',\tau') - g\, G_{\sigma,\alpha,\sigma',\alpha}(\mathbf{r},\tau,\mathbf{r}',\tau'^-;\mathbf{r}',\tau',\mathbf{r}',\tau') = \delta(\mathbf{r}-\mathbf{r}')\delta(\tau-\tau')\delta_{\sigma,\sigma'}, \quad \text{(C.2)}$$

where we have defined $\tau^\pm$ as a time infinitesimally later/earlier than τ. In Eqs. (C.1,C.2) we have introduced the two-particle Green's function $G_{\sigma,\alpha,\sigma',\beta}(\mathbf{r},\tau,\mathbf{r}'',\tau'';\mathbf{r}',\tau',\mathbf{r}''',\tau''') = \mathrm{Tr}\{\hat{\rho}T_\tau[\Psi_\sigma(\mathbf{r},\tau)\Psi_\alpha(\mathbf{r}'',\tau'')\Psi^\dagger_\beta(\mathbf{r}''',\tau''')\Psi^\dagger_{\sigma'}(\mathbf{r}',\tau')]\}$.

The spin indices in the above equations work as follows: if $\sigma = \sigma'$, then $\alpha \neq \sigma$, if $\sigma \neq \sigma'$ then in Eq. C.1, $\alpha = \sigma'$ and in Eq. C.2, $\alpha = \sigma$. This will become

clear when we consider particular cases below. In order to make more progress, we use Dyson's equation to express the two particle Green's functions in terms of the self-energy [2]. Doing so, Eqs. (C.1,C.2) become

$$\left(-\frac{\partial}{\partial\tau}+\frac{\nabla^2_{\mathbf{r}}}{2m}-U_\sigma(\mathbf{r},\tau)\right)G_{\sigma,\sigma'}(\mathbf{r},\tau,\mathbf{r}',\tau')-\sum_\mu\int d\bar{\mathbf{r}}d\bar{\tau}\Sigma_{\sigma,\mu}(\mathbf{r},\tau,\bar{\mathbf{r}},\bar{\tau}^+)G_{\mu,\sigma'}(\bar{\mathbf{r}},\bar{\tau},\mathbf{r}',\tau')= \tag{C.3}$$
$$\delta(\mathbf{r}-\mathbf{r}')\delta(\tau-\tau')\delta_{\sigma,\sigma'}$$
$$\left(\frac{\partial}{\partial\tau}+\frac{\nabla^2_{\mathbf{r}'}}{2m}-U_{\sigma'}(\mathbf{r}',\tau')\right)G_{\sigma,\sigma'}(\mathbf{r},\tau,\mathbf{r}',\tau')-\sum_\mu\int d\bar{\mathbf{r}}d\bar{\tau}G_{\sigma,\mu}(\mathbf{r},\tau,\bar{\mathbf{r}},\bar{\tau})\Sigma_{\mu,\sigma'}(\bar{\mathbf{r}},\bar{\tau}^-,\mathbf{r}',\tau')=$$
$$\delta(\mathbf{r}-\mathbf{r}')\delta(\tau-\tau')\delta_{\sigma,\sigma'}$$

where Σ denotes the self energy, which will be the main object of study. Below we develop a series of approximations to the self energy and derive the collisionless and collisional Boltzman equation. Eq. C.3 becomes the principal equation upon which we base the the calculations to follow. The time integrals in this equation range from 0 to β.

C.0.5 Hartree-Fock Analysis revisited

In this section we show that upon expanding the self energy to lowest order in the interactions, Eq. C.3 reduces to the familiar collisionless Boltzmann equation of the previous section. For this purpose we write $\Sigma = \Sigma^{HF} + \Sigma^C$, where Σ^{HF} and Σ^C are the Hartree-Fock and collision self energies respectively. We limit ourselves to considering $G_{\uparrow,\uparrow}$ and $G_{\uparrow,\downarrow}$, and the other equations follow by switching the roles of the spin indices.

The simplest approximation to the self energy is where one writes:

$$\Sigma^{HF}_{\sigma,\sigma'}(\mathbf{r},\tau,\mathbf{r}',\tau') = \delta(\mathbf{r}-\mathbf{r}')\delta(\tau-\tau')g \int d\bar{\mathbf{r}}d\bar{\tau}\delta(\mathbf{r}'-\bar{\mathbf{r}})\delta(\tau'-\bar{\tau})\delta_{\sigma,\sigma'}\delta_{\mu,\mu'} \times \qquad \text{(C.4)}$$
$$G_{\mu,\mu'}(\bar{\mathbf{r}},\bar{\tau},\bar{\mathbf{r}},\bar{\tau}^{+}) - \delta(\mathbf{r}-\mathbf{r}')\delta(\tau-\tau')g\,\delta_{\sigma,\mu'}\delta_{\mu,\sigma'}G_{\mu',\mu}(\mathbf{r}',\tau',\mathbf{r}',\tau'^{+})$$

where we note that the form of the interaction potential enforces $\sigma \neq \mu$ and $\sigma' \neq \mu'$. The first term on the right hand side is the direct contribution while the second is the exchange term. For a spinless bosonic system, both terms would have the same sign, giving rise to a factor of 2 in the Hartree-Fock self energy. By contrast, for a spinless Fermi gas, one would get 0, indicating that identical fermions interacting with *s*-wave interactions do not scatter.

From Eq. C.4 and the constraints, one obtains the following relationships

$$\Sigma^{HF}_{\uparrow,\uparrow}(\mathbf{r},\tau,\mathbf{r}',\tau') = \delta(\mathbf{1}-\mathbf{1}')gG_{\downarrow,\downarrow}(\mathbf{r},\tau,\mathbf{r}',\tau') \qquad \text{(C.5)}$$
$$\Sigma^{HF}_{\uparrow,\downarrow}(\mathbf{r},\tau,\mathbf{r}',\tau') = -\delta(\mathbf{1}-\mathbf{1}')gG_{\uparrow,\downarrow}(\mathbf{r},\tau,\mathbf{r}',\tau').$$

where we have used the notation $\delta(\mathbf{1}-\mathbf{1}') = \delta(\mathbf{r}-\mathbf{r}')\delta(\tau-\tau')$. Thus only the Hartree term contributes to $\Sigma_{\uparrow\uparrow}$, while only the exchange term contributes to $\Sigma_{\uparrow\downarrow}$. For a bosonic system, the self energy would also contain self interaction terms that are absent here due to the Pauli exclusion principle. The spin Green's functions are related to the densities as

$$G_{\downarrow,\downarrow}(\mathbf{r},\tau,(\mathbf{r},\tau) = s_{\downarrow}(\mathbf{r},\tau) \qquad \text{(C.6)}$$
$$G_{\uparrow,\downarrow}(\mathbf{r},\tau,(\mathbf{r},\tau) = s_{+}(\mathbf{r},\tau)$$

Spin-up Boltzmann equation

Evaluating the integrals on the RHS of Eq. C.3 by substituting Eq. C.5 yields for $\tau < \tau^{'}$,

$$\left(-\frac{\partial}{\partial\tau} + \frac{\nabla_{\mathbf{r}}^2}{2m} - U_{\uparrow}(\mathbf{r},\tau)\right) G^{<}_{\uparrow,\uparrow}(\mathbf{1},\mathbf{1}^{'}) = g\left(G_{\downarrow,\downarrow}(\mathbf{1},\mathbf{1}^{+})G_{\uparrow,\uparrow}(\mathbf{1},\mathbf{1}^{'}) - G_{\uparrow,\downarrow}(\mathbf{1},\mathbf{1}^{+})G_{\downarrow,\uparrow}(\mathbf{1},\mathbf{1}^{'})\right) \tag{C.7}$$

$$\left(\frac{\partial}{\partial\tau} + \frac{\nabla_{\mathbf{r}^{'}}^2}{2m} - U_{\uparrow}(\mathbf{r}^{'},\tau^{'})\right) G^{<}_{\uparrow,\uparrow}(\mathbf{1},\mathbf{1}^{'}) = g\left(G_{\uparrow,\uparrow}(\mathbf{1},\mathbf{1}^{'})G_{\downarrow,\downarrow}(\mathbf{1}^{'},\mathbf{1}^{'^{+}}) - G_{\uparrow,\downarrow}(\mathbf{1},\mathbf{1}^{'})G_{\downarrow,\uparrow}(\mathbf{1}^{'^{+}},\mathbf{1}^{'})\right) \tag{C.8}$$

where for $\tau < \tau^{'}$, the lesser Green's function $G^{<}$ is defined as $G(\mathbf{1},\mathbf{1}^{'}) = G^{<}(\mathbf{1},\mathbf{1}^{'})$ when $\tau < \tau^{'}$ and $G^{>}$ is analogously defined. The periodicity of imaginary time implies the relation

$$G^{<}(\omega) = e^{-\beta\omega}G^{>}(\omega) \tag{C.9}$$

where $\beta = 1/k_B T$

We introduce the following notation: $T = \frac{\tau+\tau^{'}}{2}$, $\overline{\tau} = \tau - \tau^{'}$, $\mathbf{R} = \frac{\mathbf{r}+\mathbf{r}^{'}}{2}$ and $\overline{\mathbf{r}} = \mathbf{r} - \mathbf{r}^{'}$, where R, T and $\overline{\mathbf{r}}$ and $\overline{\tau}$ refer to the center of mass and relative space-time coordinates respectively. Subtracting Eq. C.8 from Eq. C.7, and expressing all the coordinates in terms of these new variables, we get

$$\begin{aligned}\left(-\frac{\partial}{\partial T} + \frac{\nabla_{\mathbf{R}}\cdot\nabla_{\overline{\mathbf{r}}}}{m} - \nabla_{\mathbf{R}}U_{\uparrow}(\mathbf{R},T)\cdot\overline{\mathbf{r}}\right) G^{<}_{\uparrow,\uparrow}(\overline{\mathbf{r}},\overline{\tau},\mathbf{R},T) = \\ g\left(G^{<}_{\uparrow,\uparrow}(\overline{\mathbf{r}},\overline{\tau},\mathbf{R},T)\,\nabla_{\mathbf{R}}s_{\downarrow}(\mathbf{R},T)\cdot\overline{\mathbf{r}}\right. \\ -G^{<}_{\downarrow,\uparrow}(\overline{\mathbf{r}},\overline{\tau},\mathbf{R},T)\left(s_{+}(\mathbf{R},T) + \nabla_{\mathbf{R}}s_{+}(\mathbf{R},T)\cdot\frac{\overline{\mathbf{r}}}{2}\right) + \\ \left. G^{<}_{\uparrow,\downarrow}(\overline{\mathbf{r}},\overline{\tau},\mathbf{R},T)\left(s_{-}(\mathbf{R},T) - \nabla_{\mathbf{R}}s_{-}(\mathbf{R},T)\cdot\frac{\overline{\mathbf{r}}}{2}\right)\right)\end{aligned} \tag{C.10}$$

where we have made frequent use of Eq. C.6. Note that the first term on the

RHS of Eq. C.10 can be combined with the potential term to give an effective potential.

The Wigner functions are given by

$$f(\mathbf{p}, \mathbf{R}, t) = \int d\omega G^{<}(\mathbf{p}, \omega; \mathbf{R}, \mathbf{T}) \tag{C.11}$$

where

$$G(\mathbf{p}, \omega; \mathbf{R}, \mathbf{T}) = \int d\mathbf{r} d\mathbf{t}\, e^{i(\mathbf{p}\cdot\mathbf{r} - \omega t)} G(\mathbf{r}, t; \mathbf{R}, T) \tag{C.12}$$

Formally we write $G^{<}(\bar{\mathbf{p}}, \omega, \mathbf{R}, T) = A(\mathbf{p}, \omega, \mathbf{R}, T) f(\mathbf{p}, R, T)$ where we define A to be the spectral function given by $A = G^{>} + G^{<}$. For a non-interacting gas, this relation implies that $A = \delta(\omega - E(\mathbf{p}, R, T))$ where E is the energy. Subsequently, we get that $G^{>}(\bar{\mathbf{p}}, \omega, \mathbf{R}, T) = A(\mathbf{p}, \omega, \mathbf{R}, T)(1 - f(\mathbf{p}, R, T))$. For a Bose systems, we would have $G^{>} = A(1 + f)$.

Physically the spectral function contains all the information about the quasi-particle and it's dispersion. The assumption that the spectral density is a delta function implies that the quasi-particles have infinite lifetime. This is valid for a non-interacting system or for a Landau Fermi liquid at $T = 0$. Throughout, we will make this approximation in our calculations.

Notice that the Wigner function is simply a generalization of the well known Bose and Fermi functions denoting the occupation of a mode with energy E. Assuminat the Hamiltonian is both translationally invariant and independent of time, the Green's functions are functions only of $\mathbf{r}$ and t, hence $G^{>}(\mathbf{p}, \omega) = A(\mathbf{p}, \omega) f(\mathbf{p})$, which implies that $f(\mathbf{p}) = (e^{E(p)} + 1)^{-1}$ where we have used the fact that $A(\mathbf{p}, \omega) = \delta(\omega - E(\mathbf{p}))$.

Multiplying throughout by $\exp(-\imath \mathbf{p}\cdot\bar{\mathbf{r}})$, setting $\bar{\tau} = 0$, and integrating over $\bar{\mathbf{r}}$

we get

$$\left(\frac{\partial}{\partial T}+\frac{\mathbf{p}}{m}\nabla_{\mathbf{R}}-U_{eff,\uparrow}(\mathbf{R},t)\cdot\nabla_{\mathbf{p}}\right)f_{\uparrow,\uparrow}(\mathbf{p},\mathbf{R},t)=\imath g\left(s_{+}(\mathbf{R},t)f_{\downarrow,\uparrow}(\mathbf{p},\mathbf{R},t)-\right. \tag{C.13}$$
$$\left.s_{-}(\mathbf{R},t)f_{\uparrow,\downarrow}(\mathbf{p},\mathbf{R},T)\right)-\frac{g}{2}\left(\nabla_{\mathbf{R}}s_{+}(\mathbf{R},t)\cdot\nabla_{\mathbf{p}}f_{\downarrow,\uparrow}(\mathbf{p},\mathbf{R},t)+\nabla_{\mathbf{R}}s_{-}(\mathbf{R},t)\cdot\nabla_{\mathbf{p}}f_{\uparrow,\downarrow}(\mathbf{p},\mathbf{R},t)\right)$$

where we have analytically continued to real time $T=\imath T$. This is equivalent to the Boltzmann equation for $f_{\uparrow,\uparrow}$ (Eq. B.4).

Up-Down Boltzmann equation

Following the same procedure outlined above, Eq. C.3 can be written as

$$\left(-\frac{\partial}{\partial\tau}+\frac{\nabla_{\mathbf{r}}^{2}}{2m}-U_{\uparrow}(\mathbf{r},\tau)\right)G_{\uparrow,\downarrow}^{<}(\mathbf{1},\mathbf{1}')=g\left(G_{\downarrow,\downarrow}(\mathbf{1},\mathbf{1}^{+})G_{\uparrow,\downarrow}(\mathbf{1},\mathbf{1}')-\right. \tag{C.14}$$
$$\left.G_{\uparrow,\downarrow}(\mathbf{1},\mathbf{1}^{+})G_{\downarrow,\downarrow}(\mathbf{1},\mathbf{1}')\right)$$
$$\left(\frac{\partial}{\partial\tau}+\frac{\nabla_{\mathbf{r}'}^{2}}{2m}-U_{\downarrow}(\mathbf{r}',\tau')\right)G_{\uparrow,\downarrow}^{<}(\mathbf{1},\mathbf{1}')=-g\left(G_{\uparrow,\uparrow}(\mathbf{1},\mathbf{1}')G_{\uparrow,\downarrow}(\mathbf{1}',\mathbf{1}'^{+})-\right. \tag{C.15}$$
$$\left.G_{\uparrow,\downarrow}(\mathbf{1},\mathbf{1}')G_{\uparrow,\uparrow}(\mathbf{1}'^{+},\mathbf{1}')\right)$$

In terms of the center of mass and relative coordinates introduced above, difference between Eq. C.14 and Eq. C.15 is

$$\left(-\frac{\partial}{\partial T}+\frac{\nabla_{\mathbf{R}}\cdot\nabla_{\bar{\mathbf{r}}}}{m}-\frac{1}{2}\nabla_{\mathbf{R}}(U_{\uparrow}(\mathbf{R},T)+U_{\downarrow}(\mathbf{R},T))\cdot\bar{\mathbf{r}}-(U_{\uparrow}(\mathbf{R},T)-U_{\downarrow}(\mathbf{R},T))\right)\times \tag{C.16}$$
$$G_{\uparrow,\downarrow}^{<}(\bar{\mathbf{r}},\bar{\tau},\mathbf{R},T)=g\left\{G_{\uparrow,\downarrow}^{<}\left(\bar{\mathbf{r}},\bar{\tau},\mathbf{R},T\right)(s_{\downarrow}(\mathbf{R},T)+\nabla_{\mathbf{R}}s_{\downarrow}(\mathbf{R},T)\cdot\frac{\bar{\mathbf{r}}}{2}-\right.$$
$$\left.s_{\uparrow}(\mathbf{R},T)+\nabla_{\mathbf{R}}s_{\uparrow}(\mathbf{R},T)\cdot\frac{\bar{\mathbf{r}}}{2}\right)$$
$$-G_{\downarrow,\downarrow}^{<}(\bar{\mathbf{r}},\bar{\tau},\mathbf{R},T)\left(s_{+}(\mathbf{R},T)+\nabla_{\mathbf{R}}s_{+}(\mathbf{R},T)\cdot\frac{\bar{\mathbf{r}}}{2}\right)+G_{\uparrow,\uparrow}^{<}(\bar{\mathbf{r}},\bar{\tau},\mathbf{R},T)\left(s_{+}(\mathbf{R},T)-\nabla_{\mathbf{R}}s_{+}(\mathbf{R},T)\cdot\frac{\bar{\mathbf{r}}}{2}\right)\Bigg\}$$

As before, the first term on the RHS of Eq. C.16 may be combined with the potentials to yield an effective potential. Taking the Fourier transform of this equation with $\bar{\mathbf{r}}$, one gets:

$$\left(\frac{\partial}{\partial T}+\frac{\mathbf{p}\cdot\nabla_{\mathbf{R}}}{m}-\frac{1}{2}\nabla_{\mathbf{R}}(U_{eff,\uparrow}(\mathbf{R},T)+U_{eff,\downarrow}(\mathbf{R},T))\cdot\nabla_{\mathbf{p}}+\imath(U_{eff,\uparrow}(\mathbf{R},T)-U_{eff,\downarrow}(\mathbf{R},T))\right)\times \tag{C.17}$$

$$f_{\uparrow,\downarrow}(\mathbf{p},\mathbf{R},T)=\imath g\left\{s_{+}(\mathbf{R},T)\left(f_{\downarrow,\downarrow}(\mathbf{p},\mathbf{R},T)-f_{\uparrow,\uparrow}(\mathbf{p},\mathbf{R},T)\right)-\right.$$

$$\left.\frac{1}{2}\nabla_{\mathbf{R}}s_{+}(\mathbf{R},T)\cdot\nabla_{\mathbf{p}}\left(f_{\uparrow,\uparrow}(\mathbf{p},\mathbf{R},T)+f_{\downarrow,\downarrow}(\mathbf{p},\mathbf{R},T)\right)\right\}$$

which is equivalent to Eq. B.5.

C.0.6 Collision Analysis

The Hartree-Fock equations just obtained represent the direct and exchange contributions to the "forward" scattering amplitude. Physically it represents the impact of adding a particle to the system, and removing it at a later time and returning the system to the same state as it was when it started. But since the added particle doesn't collide with any other particles during this time, the lifetime of a single particle state is infinite. What allows a system that has been excited to return to thermal equilibrium, is the possibility for a particle to collide with other particles and exchange momentum. We would like to understand the physics behind these collisions within the simplest framework, namely the Born approximation. Once again we find two kinds of contributions - a direct and an exchange contribution.

The collisional part of the self energy is given by [1]

$$\Sigma^C_{\sigma,\sigma'}(\mathbf{1},\mathbf{1}') = -g^2 \int d\bar{\mathbf{1}} d\bar{\mathbf{1}}' G_{\lambda,\lambda'}(\mathbf{1},\mathbf{1}')\delta_{\sigma,\lambda}\delta_{\mu_1,\bar{\mu_1}} G_{\mu_1,\mu_2}(\bar{\mathbf{1}},\bar{\mathbf{1}}') G_{\bar{\mu_2},\bar{\mu_1}}(\bar{\mathbf{1}}',\bar{\mathbf{1}}) \times \qquad \text{(C.18)}$$
$$\delta_{\sigma',\lambda},\delta_{\bar{\mu_2},\bar{\mu_2}}\delta(\mathbf{1}-\bar{\mathbf{1}})\delta(\mathbf{1}'-\bar{\mathbf{1}}')$$
$$+g^2 \int d\bar{\mathbf{1}} d\bar{\mathbf{1}}' G_{\lambda,\lambda'}(\mathbf{1},\mathbf{1}')\delta_{\sigma,\lambda}\delta_{\mu_1,\bar{\mu_1}} G_{\mu_1,\mu_2}(\bar{\mathbf{1}},\bar{\mathbf{1}}') G_{\bar{\mu_2},\bar{\mu_1}}(\mathbf{1}',\bar{\mathbf{1}})\delta_{\sigma',\mu_2}\delta_{\bar{\mu_2},\lambda},\delta(\mathbf{1}-\bar{\mathbf{1}})\delta(\mathbf{1}'-\bar{\mathbf{1}}')$$

where the form of the interaction potential forces the constraint $\bar{\mu_1} \neq \sigma$ and $\bar{\mu_2} \neq \sigma'$. The particular form of the collisional self energy for $\sigma, \sigma' \in (\uparrow, \downarrow)$:

$$\Sigma^C_{\uparrow,\uparrow}(\mathbf{1},\mathbf{1}') = -g^2(G_{\uparrow,\uparrow}(\mathbf{1},\mathbf{1}')G_{\downarrow,\downarrow}(\mathbf{1},\mathbf{1}')G_{\downarrow,\downarrow}(\mathbf{1}',\mathbf{1}) \qquad \text{(C.19)}$$
$$-G_{\uparrow,\downarrow}(\mathbf{1},\mathbf{1}')G_{\downarrow,\uparrow}(\mathbf{1},\mathbf{1}')G_{\downarrow,\downarrow}(\mathbf{1}',\mathbf{1}))$$
$$\Sigma^C_{\uparrow,\downarrow}(\mathbf{1},\mathbf{1}') = -g^2(G_{\uparrow,\downarrow}(\mathbf{1},\mathbf{1}')G_{\downarrow,\uparrow}(\mathbf{1},\mathbf{1}')G_{\uparrow,\downarrow}(\mathbf{1}',\mathbf{1})$$
$$-G_{\uparrow,\uparrow}(\mathbf{1},\mathbf{1}')G_{\downarrow,\downarrow}(\mathbf{1},\mathbf{1}')G_{\uparrow,\downarrow}(\mathbf{1}',\mathbf{1}))$$

and $\Sigma^C_{\downarrow,\downarrow}$ and $\Sigma^C_{\downarrow,\uparrow}$ can be obtained by interchange of $\uparrow$ and $\downarrow$. We have retained the $-$ sign in front of these definitions because the real time self energies are simply the negatives of the imaginary time self energies, for this case. Once again there is a relative $-$ signs between the direct and exchange contributions to the collisions, which would be a + sign for a Bose gas.

Noting the form of the right hand side of Eq.C.3, we can simplify our notation. We define the matrix of Green's functions and the self energy

$$\overleftrightarrow{\mathbf{G}} = \begin{pmatrix} G_{\uparrow\uparrow}(\mathbf{1},\mathbf{1}') & G_{\uparrow\downarrow}(\mathbf{1},\mathbf{1}') \\ G_{\downarrow\uparrow}(\mathbf{1},\mathbf{1}') & G_{\downarrow\downarrow}(\mathbf{1},\mathbf{1}') \end{pmatrix} \qquad \text{(C.20)}$$
$$\overleftrightarrow{\Sigma^C} = \begin{pmatrix} \Sigma^C_{\uparrow\uparrow}(\mathbf{1},\mathbf{1}') & \Sigma^C_{\uparrow\downarrow}(\mathbf{1},\mathbf{1}') \\ \Sigma^C_{\downarrow\uparrow}(\mathbf{1},\mathbf{1}') & \Sigma^C_{\downarrow\downarrow}(\mathbf{1},\mathbf{1}') \end{pmatrix}$$

and Eq. C.3 becomes

$$\left(-\frac{\partial}{\partial\tau}+\frac{\nabla_{\mathbf{r}}^2}{2m}-\overleftrightarrow{U}(\mathbf{1})\right)\overleftrightarrow{G}(\mathbf{1},\mathbf{1}')-\int d\bar{\mathbf{1}}\overleftrightarrow{\Sigma}(\mathbf{1},\bar{\mathbf{1}}^{+})\overleftrightarrow{G}(\bar{\mathbf{1}},\mathbf{1}')=0 \tag{C.21}$$
$$\left(\frac{\partial}{\partial\tau}+\frac{\nabla_{\mathbf{r}'}^2}{2m}-\overleftrightarrow{U}_{adj}(\mathbf{1}')\right)\overleftrightarrow{G}(\mathbf{1},\mathbf{1}')-\int d\bar{\mathbf{1}}\overleftrightarrow{G}(\mathbf{1},\bar{\mathbf{1}})\overleftrightarrow{\Sigma}(\bar{\mathbf{1}},\mathbf{1}')=0$$

where we have assumed that $\tau < \tau'$ and the definition of $\overleftrightarrow{U}$ is clear by inspection. The subscript *adj* refers to the adjoint. These equations have the same form as Eq. 8.16 in [1], except in matrix form.

Defining the center of mass and relative coordinates ($\mathbf{R}$, T; $\mathbf{r}$, t) as in the previous subsection, we obtain the matrix equivalent of the fourier transform of the *real time* equation of motion for the lesser Green's function matrix in terms of the self energies (see Ch.9 of [1])

$$\left(\frac{\imath\partial}{\partial T}+\frac{\imath\nabla_{\mathbf{R}}\cdot\mathbf{p}}{m}-\frac{\imath}{2}\nabla_{\mathbf{R}}(\overleftrightarrow{U}(\mathbf{R},T)+\overleftrightarrow{U}_{adj}(\mathbf{R},T))\cdot\nabla_{\mathbf{p}}-(\overleftrightarrow{U}(\mathbf{R},T)-\overleftrightarrow{U}_{adj}(\mathbf{R},T))\right)\times \tag{C.22}$$
$$\overleftrightarrow{G}^{<}(\mathbf{p},\omega;\mathbf{R},T)=\imath\Big(\left\{\overleftrightarrow{G}^{<}(\mathbf{p},\omega;\mathbf{R},T),\overleftrightarrow{\Sigma}^{>}(\mathbf{p},\omega;\mathbf{R},T)\right\}-$$
$$\left\{\overleftrightarrow{G}^{>}(\mathbf{p},\omega;\mathbf{R},T),\overleftrightarrow{\Sigma}^{<}(\mathbf{p},\omega;\mathbf{R},T)\right\}\Big)$$

where the prefactor $\imath$ arises because we analytically continued the left and right hand sides of this equation to real time.

Notice the difference between this equation and Eq. 9.7(a) in [1], is the anti-commutator arising from the matrix nature of the self energies and Green's functions. A formal derivation of this is also found in Ref. [3].

Physically, $\Sigma^{>}$ is interpreted in momentum-energy space as the effect of collisions on a particle with momentum $\mathbf{p}$ and energy ω that is added to the system, and $\Sigma^{<}$ is the likelihood to scatter into a state of momentum $\mathbf{p}$ and energy ω.

Converting the Green's functions to Wigner functions:

$$\left(\frac{\partial}{\partial T}+\frac{\mathbf{p}\cdot\nabla_{\mathbf{R}}}{m}-\frac{1}{2}\nabla_{\mathbf{R}}(\overleftrightarrow{U}(\mathbf{R},T)+\overleftrightarrow{U}_{adj}(\mathbf{R},T))\cdot\nabla_{\mathbf{p}}-(\overleftrightarrow{U}(\mathbf{R},T)-\overleftrightarrow{U}_{adj}(\mathbf{R},T))\right)\times \quad \text{(C.23)}$$
$$\overleftrightarrow{f}(\mathbf{p},\mathbf{R},T)=\left(\left\{\overleftrightarrow{f}(\mathbf{p},\mathbf{R},T),\overleftrightarrow{\Sigma}^{>}(\mathbf{p},\omega;\mathbf{R},T)\right\}-\left\{(\overleftrightarrow{I}-\overleftrightarrow{f})(\mathbf{p},\mathbf{R},T),\overleftrightarrow{\Sigma}^{<}(\mathbf{p},\omega;\mathbf{R},T)\right\}\right)$$

where $\overleftrightarrow{I}$ is the unit matrix. We used the fact that $G^{<}(\mathbf{p},\omega,R,T) = A(\omega,\mathbf{p},R,T)\times f(\mathbf{p},R,T)$ and $G^{>} = A(1-f)$, where the spectral function $A(\omega,\mathbf{p},R,T)=2\pi\delta(\omega-E(\mathbf{p},R,T))$.

All that remains to be done is to Fourier transform the self energies in order to get the final expression for the collision integral.

From Eq. C.19, we can express the collision self energy matrix in real time as $\overleftrightarrow{\Sigma}^{C}(\mathbf{1},\mathbf{1}')=g^2\det(\overleftrightarrow{G})(\mathbf{1},\mathbf{1}')\overleftrightarrow{G}_{adj}(\mathbf{1}',\mathbf{1})$, which implies that

$$\overleftrightarrow{\Sigma}^{<C}(\mathbf{1},\mathbf{1}')=g^2\det(\overleftrightarrow{G}^{<})(\mathbf{1},\mathbf{1}')\overleftrightarrow{G}^{>}_{adj}(\mathbf{1}',\mathbf{1}) \quad \text{(C.24)}$$
$$\overleftrightarrow{\Sigma}^{>C}(\mathbf{1},\mathbf{1}')=g^2\det(\overleftrightarrow{G}^{>})(\mathbf{1},\mathbf{1}')\overleftrightarrow{G}^{<}_{adj}(\mathbf{1}',\mathbf{1})$$

Fourier transforming the self energies we get:

$$\left(\frac{\partial}{\partial T}+\frac{\mathbf{p}\cdot\nabla_{\mathbf{R}}}{m}-\frac{1}{2}\nabla_{\mathbf{R}}\left(\overleftrightarrow{U}(\mathbf{R},T)+\overleftrightarrow{U}_{adj}(\mathbf{R},T)\right)\cdot\nabla_{\mathbf{p}}- \quad \text{(C.25)}$$
$$\left(\overleftrightarrow{U}(\mathbf{R},T)-\overleftrightarrow{U}_{adj}(\mathbf{R},T)\right)\overleftrightarrow{f}(\mathbf{p},\mathbf{R},T)=-g^2\left[\int\frac{d\mathbf{p}_1d\mathbf{p}_2d\mathbf{p}_3}{(2\pi)^5}\delta(\mathbf{p}_1+\mathbf{p}_2-\mathbf{p}_3-\mathbf{p})\times\right.$$
$$\delta(\omega_1+\omega_2-\omega_3-\omega)\left(\left\{\overleftrightarrow{f}(\mathbf{p},\mathbf{R},T),\det(\overleftrightarrow{I}-\overleftrightarrow{f})(\mathbf{p}_1,\mathbf{p}_2,\mathbf{R},T)\overleftrightarrow{f}_{adj}(\mathbf{p}_3,\mathbf{R},T)\right\}-\right.$$
$$\left.\left.\left\{(\overleftrightarrow{I}-\overleftrightarrow{f})(\mathbf{p},\mathbf{R},T),\det(\overleftrightarrow{f}(\mathbf{p}_1,\mathbf{p}_2,\mathbf{R},T))(\overleftrightarrow{I}-\overleftrightarrow{f})_{adj}(\mathbf{p}_3,\mathbf{R},T)\right\}\right)\right\}\right]$$

where the ω s are the energies in the Hartree approximation given by $\frac{p^2}{2m}+U_{eff}$. Notice that since an interaction always involves two ↑s and two ↓s, the U_{eff}

terms in the delta function always cancel, implying kinetic energy conservation or an elastic collision. If we neglect the spin structure, our equations reduce to the collision integral derived in [1].

It can be shown by explicit calculation in the non-degenerate limit, that this equation is exactly identical to Eq.2.6 of Ref. [3], after correcting the crucial typo in the last term of Eq. 2.6. This is exactly the limit we consider below. In order to numerically integrate this collision term, we construct approximation to the collision integral. The approximation we make in the following section is: the dynamics is quasi one-dimensional.

High temperature limit

Integrating the collision integral is generally a hard task, even numerically as it involves integrating over 3 momenta. However a limit where the integration becomes particularly simple is in the high temperature limit. The first simplification to Eq. C.25 is that one can ignore the Pauli blocking terms in the collision integral. The product of 4 f factors thus reduces to a product of 2 to lowest order.

Next we assume that the transverse directions are decoupled from the longitudinal directions and write the distribution functions as $f(\mathbf{p}, \mathbf{R}, T) = f(\mathbf{p}_\perp, \mathbf{R}_\perp) f(\mathbf{p}_\parallel, \mathbf{R}_\parallel, T) = \exp(-\beta(\frac{p_\perp^2}{2m} + U(R_\perp))) f(\mathbf{p}_\parallel, \mathbf{R}_\parallel, T)$. This is a good approximation for quasi 1D systems such as the one considered in Chapter 2 because of the tight transverse confinement.

Since the collision integral is only an integral in momentum, we ignore the radial dependence of the distribution function in the following calculations.

Furthermore since we are interested in one dimensional dynamics, we integrate both sides of Eq. C.25 over $p_{\perp}$.

Denoting the right hand side of Eq. C.25 by I_{coll}, the collision integral becomes

$$I_{coll} = \frac{g^2 m^2}{\beta}\frac{1}{2}\Bigg(\int \frac{dp_1 dp_2}{(2\pi)^3}\Big\{\overleftrightarrow{f}(p), \overleftrightarrow{f}_{adj}(p_1)\Big\}K(p_2, p, p_1) - 2\int \frac{dp_1 dp_2}{(2\pi)^3}\Big\{\overleftrightarrow{f}(p_1), \overleftrightarrow{f}_{adj}(p_2)\Big\}K(p, p_1, p_2)\Bigg) \tag{C.26}$$

where the kernel $K(p, p_1, p_2)$ is given by

$$\begin{cases} \frac{1}{2}\left(\frac{1}{2} + \frac{3\pi}{8}\right)\exp\left(\frac{-\beta F(p,p_1,p_2)}{m}\right) F(p, p_1, p_2) > 0 \\ \frac{1}{2}\left(\frac{1}{2} + \exp\left(\frac{-\beta F(p,p_1,p_2)}{m}\right)\frac{\pi}{8}\right. \\ \left.\left(3 + \mathrm{Erf}^2\left[\sqrt{\frac{-\beta F(p,p_1,p_2)}{m}}\right] - 4\,\mathrm{Erf}\left[\sqrt{\frac{-\beta F(p,p_1,p_2)}{m}}\right]\right)\right) \\ F(p, p_1, p_2) < 0 \end{cases}$$

where $F(p, p_1, p_2) = \left(p - \frac{p_1+p_2}{2}\right)^2 - \left(\frac{p_1-p_2}{2}\right)^2$.

BIBLIOGRAPHY

[1] L.P.Kadanoff and G. Baym, *Quantum Statistical Mechanics* W.A.Benjamin Inc. New York (1962).

[2] A.L.Fetter and J.D.Walecka, *Quantum Theory of Many-Particle Systems* Dover, NewYork, (2003).

[3] J.W. Jeon and W.J. Mullin, J.Phys (France) **49** 1988 1691-1706.

APPENDIX D

EFFECTIVE ACTION FOR THE BOSE HUBBARD MODEL

In this Appendix I work out the details of the derivation of the effective action for the Bose Hubbard model (Eq. 3.25 and Eq. 10.21 in [1]) near the superfluid-Mott critical point. My approach will follow that of [2], getting results identical to those obtained by [3] using a complementary approach.

The partition function Z_B for the Bose Hubbard model is given by

$$\mathcal{Z} = \int \mathcal{D}\psi_i \mathcal{D}\psi_i^\dagger \exp(-\mathcal{S}) \tag{D.1}$$

where the action $\mathcal{S}$ is defined in imaginary time τ as

$$\mathcal{S} = \int_0^\beta d\tau \sum_i \psi_i^\dagger \Big(\partial_\tau - \mu_i + \frac{U}{2}\psi_i^\dagger \psi_i\Big)\psi_i - J \sum_{\langle ij \rangle} \Big(\psi_i^\dagger \psi_j + h.c\Big) \tag{D.2}$$

where $\beta = 1/T$, ψ denotes the bosonic annihilation operator and μ_i denotes the chemical potential at site i. Here J denotes nearest neighbor hopping and U denotes the on-site repulsion.

In order to make progress, I decouple the hopping term by introducing an auxillary field ψ_{Bi} and using the formula

$$\int \mathcal{D}x_i \mathcal{D}x_i^* e^{-x_i w^{-1} x_j + x_i^* h_i + x_i h_i^*} = Det[w]^{-1} e^{-h_i w_{ij} h_j} \tag{D.3}$$

to get:

$$\mathcal{Z} = \int \mathcal{D}\psi_i \mathcal{D}\psi_i^\dagger \mathcal{D}\psi_{Bi} \mathcal{D}\psi_{Bi}^* \exp(-\mathcal{S}') \tag{D.4}$$

$$\mathcal{S}' = \int_0^\beta d\tau \sum_i \psi_i^\dagger \Big(\partial_\tau - \mu_i + \frac{U}{2}\psi_i^\dagger \psi_i\Big)\psi_i - \psi_i^\dagger \psi_{Bi} - \psi_{Bi}^* \psi_i + \sum_{ij} \Big(\psi_{Bi}^* J_{ij}^{-1} \psi_{Bj}\Big) \tag{D.5}$$

where I have defined a generalized hopping matrix J_{ij} which is equal to J if i, j are nearest neighbors but zero otherwise.

A cumulant expansion in powers of ψ_B yields the effective low energy theory. Formally I write:

$$e^{-\mathcal{S}_{eff}} = e^{-\sum_{ij}(\psi^*_{Bi}J^{-1}_{ij}\psi_{Bj})} \times \int \mathcal{D}\psi_i \mathcal{D}\psi^\dagger_i e^{-\mathcal{S}^{(0)}} e^{\sum_i \int_0^\beta d\tau \psi^\dagger_i \psi_{Bi} + \psi^*_{Bi}\psi_i} \tag{D.6}$$

where S^0 is the bare action in the absence of tunneling which is a sum of site-wise decoupled Hamiltonians. As a result, one can obtain closed form expressions for all the Green's functions to all orders

Before considering the averages, note that the first term is readily diagonalized in momentum space. Introducing a quasi-momentum q, we get

$$I = \sum_{ij}(\psi^*_{Bi}J^{-1}_{ij}\psi_{Bj}) = \sum_q J^{-1}(q)|\psi_q|^2 \tag{D.7}$$

where $\psi(q) = \sum_r e^{iq\cdot r}\psi(r)$(D.8)is the Fourier transform of the boson field, and

$$J(q) = 2J\sum_{j=1}^{d}\cos(q_j a) \tag{D.9}$$

is the Fourier transform of the hopping operator on a hypercubic lattice with spacing a.

As we are interested in long wave-length behavior, we may expand the hopping term for small q to give $J^{-1}(q) \approx 1/zJ(1 + a^2q^2/z)$ where $z = 2d$ is the co-ordination number. The final expression in Fourier space becomes $\sum_q 1/zJ(1 + a^2q^2/z)|\psi(q)|^2$, which may be Fourier transformed back to

$$I = 1/zJ\sum_i |\psi_i|^2 + 1/J(a/z)^2\sum_i |\nabla_i\psi_i|^2 \tag{D.10}$$

Next, consider the second term in the action. To proceed I expand out the exponential term, writing the averages as Green's functions in the Mott insulating state. To calculate the terms that enter to quadratic order in the auxillary field,

note the following averages:

$$\langle \psi_i(\tau) \rangle = \langle \psi_i^\dagger(\tau) \rangle = 0 \tag{D.11}$$

$$\langle \psi_i(\tau)\psi_j(\tau') \rangle = \langle \psi_i^\dagger(\tau)\psi_j^\dagger(\tau') \rangle = 0$$

$$\langle \psi_i^\dagger(\tau)\psi_j(\tau') \rangle = 0 \text{ unless } i = j$$

The expectation value of the operators can be obtained by introducing a time-ordering operator

$$\langle \psi_i^\dagger(\tau)\psi_i(\tau') \rangle = \langle T_\tau[\psi_i^\dagger(\tau)\psi_i(\tau')] \rangle_{S^0} = \Theta(\tau - \tau')\langle \psi_i^\dagger(\tau)\psi_i(\tau') \rangle + \Theta(\tau' - \tau)\langle \psi_i(\tau')\psi_i^\dagger(\tau) \rangle \tag{D.12}$$

where Θ is the Heaviside theta function.

Next note that in the Heisenberg picture, the time-evolution of an operator is given by $\hat{A}(\tau) = e^{H_0\tau}\hat{A}e^{-H_0\tau}$, which we will use in the following result:

The time-correlation function $\langle \psi_i^\dagger(\tau)\psi_i(\tau') \rangle$ may be determined as follows:

$$\langle \psi^\dagger(\tau)\psi_i(\tau') \rangle = \sum_m \Theta(\tau - \tau')\langle g|\psi^\dagger(\tau)|m\rangle\langle m|\psi(\tau')|g\rangle + \tag{D.13}$$

$$\Theta(\tau' - \tau)\langle g|\psi(\tau')|m\rangle\langle m|\psi^\dagger(\tau)|g\rangle =$$

where g denotes the occupation of the ground state with g particles. Using the above formula for time dependence:

$$\langle \psi^\dagger(\tau)\psi_i(\tau') \rangle = \Theta(\tau - \tau')(g+1)e^{(E_g - E_{g+1})(\tau - \tau')} + \tag{D.14}$$

$$\Theta(\tau' - \tau)ge^{(E_g - E_{g-1})(\tau - \tau')}$$

Now we can calculate the quadratic correction to the effective action. Expanding out the exponential, and noting that terms linear in ψ_B vanish, owing to the vanishing expecation value of ψ in the Mott phase, we consider the

quadratic term. The action reads

$$\mathcal{S}^{(2)}_{eff} = -\frac{1}{2}\sum_{i,j}\int_0^\beta d\tau \int_0^\beta d\tau' \psi_{Bi}(\tau)\psi^*_{Bj}(\tau')\langle\psi^\dagger_i(\tau)\psi_j(\tau')\rangle_{\mathcal{S}^0} \\ +\psi^*_{Bi}\psi_{Bj}(\tau')\langle\psi_i(\tau)(\tau)\psi^\dagger_j(\tau')\rangle_{\mathcal{S}^0} \tag{D.15}$$

Next we write the ψ_B time dependence in terms of Matsubara frequencies $\omega_n = 2\pi n/\beta$ as

$$\psi_B = \frac{1}{\sqrt{\beta}}\sum_n e^{-i\omega_n\tau}\psi^n_B(\tau) \tag{D.16}$$

The time integrals may now be easily done using Eq.2.6 to get:

$$\mathcal{S}^{(2)}_{eff} = -\sum_i\sum_n |\psi^n_{Bi}|^2\Big\{\frac{g+1}{gU-\mu-i\omega_n} - \frac{g}{U(g-1)-\mu-i\omega_n}\Big\} \tag{D.17}$$

where we have used the fact that the energies of the Mott insulating ground state are simply

$$E_g = \frac{U}{2}g(g-1) - \mu g \tag{D.18}$$

to give

$$E_g - E_{g+1} = -gU + \mu < 0 \\ E_g - E_{g-1} = U(g-1) - \mu < 0 \tag{D.19}$$

The Matsubara frequencies may be converted to real energies using $i\omega_n \to \omega$ and a temporal expansion may be performed for small ω. The leading order terms yield the effective action. Fourier transforming back, yields the effective action in the time domain. To zeroth order in ω.

$$\mathcal{S}^{(2)}_{eff}(\omega=0) = \sum_i |\psi_{Bi}|^2\Big[1/zJ - \frac{g+1}{gU-\mu} + \frac{g}{U(g-1)-\mu}\Big] \tag{D.20}$$

The first order term in ω is:

$$\mathcal{S}_{eff\mathcal{O}(1)} = \sum_i \psi^*_{Bi}\partial_\tau\psi_{Bi}\Big[\frac{g+1}{(gU-\mu)^2} - \frac{g}{(U(g-1)-\mu)^2}\Big] \tag{D.21}$$

The second order term gives:

$$\mathcal{S}_{eff O(2)} = \sum_i |\partial_\tau \psi_{Bi}|^2 \Big[\frac{g+1}{(gU-\mu)^3} - \frac{g}{(U(g-1)-\mu)^3} \Big] \tag{D.22}$$

We have thus calculated all the terms to quadratic order in the action for the Bose Hubbard model. Finally, the sum over sites can be replaced y an integral using the rule $\sum_i = \frac{1}{a^d} \int d^d r$. The effective action to quadratic order then has the following generic structure:

$$\mathcal{S}_{eff} = 1/V \int d^{\mathrm{d}}\mathbf{r}\, K_1 \psi_B^* \partial_\tau \psi_B + K_2 |\partial_\tau \psi_B|^2 + K_3 |\partial_i \psi_B|^2 + r\, |\psi_B|^2 + O(4) \tag{D.23}$$

where the co-efficients may be read off from the analysis above.

The leading co-efficient of the fourth order term $u|\psi_B|^4$ can be found in [2] and is repeated below for completeness.

$$u = \frac{g(g-1)(zJ)^2}{[U(g-1)-\mu]^2[U(2g-3)-2\mu]} + \frac{(g+1)(g+2)(zJ)^2}{[\mu-Ug]^2[2\mu-U(2g+1)]} - \left(\frac{g}{U(g-1)-\mu} + \frac{g+1}{\mu-Ug}\right) \times \left(\frac{g(zJ)}{[U(g-1)-\mu]^2} + \frac{(g+1)(zJ)}{[\mu-Ug]^2}\right) \tag{D.24}$$

Analytically continuing to real time $\tau = -it$, and making the action stationary with respect to ψ_B yields the equation of motion, which is the central object of our study.

$$iK_1 \partial_t \psi_B + K_2 \partial_t^2 \psi_B - K_3 \nabla_r^2 \psi_B + r\psi_B + u\psi_B |\psi_B|^2 = 0 \tag{D.25}$$

Thus to recap what we have accomplished, we have derived an effective weak-coupling theory for the order parameter near the critical point, by integrating out the density ψ variables.

BIBLIOGRAPHY

[1] S. Sachdev, *Quantum Phase Transitions*, Cambridge University Press (New York) (1999).

[2] D. van Oosten, P. van der Straten and H. T. C. Stoof, Phys. Rev. A **63** 053601 (2001).

[3] K. Sengupta and N. Dupuis, Phys. Rev. A **71** 033629 (2005).

APPENDIX E

DYNAMICS OF THE TWO-BODY CORRELATION FUNCTION TO $O(U/J)$

Here I discuss the derivation of Eq. 5.6 in Chapter 5. In Appendix , I will use this formula to derive the equations of motion governing the dynamics of the momentum distribution to order $O(U/J)^2$.

I start by Fourier transforming Eq. 5.4 to obtain:

$$\left(i\partial_t - 2J(\cos p + \cos q - \cos r - \cos s)\right)g_{rs}^{pq} = -iU\int dxdydz\Big(g_{zrs}^{xyq}\delta(x+y-z-p) + g_{zrs}^{pxy}\delta(x+y-z-q) - g_{yzs}^{pqx}\delta(y-z-x-r) - g_{yzr}^{pqx}\delta(y-z-x-s)\Big) \quad \text{(E.1)}$$

where the n-body Green's function in real space is given by:

$$g_{j_1\ldots j_n}^{i_1\ldots i_n}(t) = \frac{1}{i^n}\langle a_{i_i}^{\dagger}(t)\ldots a_{i_n}^{\dagger}(t)a_{j_n}(t)\ldots a_{j_1}(t)\rangle \quad \text{(E.2)}$$

Assuming a homogeneous initial state of n_0 bosons per site, I expand the *three* body correlation function as:

$$ig_{suv}^{pqr}(\mathtt{t}=0) = -\Big(n_0(n_0-1)(n_0-2)\delta_{p+q+r-s-u-v} + n_0^2(n_0-1)(\delta_{ps}\delta_{q+r-u-v}+\ldots) + n_0^3(\delta_{ps}\delta_{qu}\delta_{rv}+\ldots)\Big) \quad \text{(E.3)}$$

where the ... indicate all possible terms of that type. For example, for the term proportional to $n_0^2(n_0-1)$, there are 9 such possibilities.

I now assume that the three body correlator evolves as if the system were non-interacting:

$$g_{suv}^{pqr}(\mathtt{t}) = g_{suv}^{pqr}(\mathtt{t}=0)\times e^{-2iJ\mathtt{t}(\cos(p)+\cos(q)+\cos(r)-\cos(s)-\cos(u)-\cos(v))} \quad \text{(E.4)}$$

Combining these expressions and substituting them into Eq. 5.3, one obtains Eq. 5.6.

Although the expression for the three-body correlation function has many terms, the calculation rapidly simplifies. First note that the terms of the form $\delta_{ps}\delta_{qu}\delta_{rv}$ produce no dynamics and give rise to constants that cancel out when substituted into Eq. E.1.

The terms proportional to $n_0(n_0-1)$ have to be considered carefully. The 9 terms that add up to g^{xyq}_{zrs} are: Expanding the terms one finds:

$$g^{xyq}_{zrs}(t=0) = (\delta_{xz}\delta_{yqrs} + \delta_{yz}\delta_{xqrs}) + (\delta_{xr}\delta_{yqzs} + \delta_{xs}\delta_{yqzr} \tag{E.5}$$
$$+\delta_{yr}\delta_{xqzs} + \delta_{ys}\delta_{yqzr}) + \delta_{qz}\delta_{xyrs} + (\delta_{qr}\delta_{xyzs} + \delta_{qs}\delta_{xyzr})$$

where the brackets indicate terms which yield similar forms upon integration. Also the delta-function δ_{abcd} is short-hand for $\delta_{a+b-c-d}$.

By considering each of the brackets separately for the 4 terms in the right hand side of Eq. E.1, one finds that only the term $\delta_{qz}\delta_{xyrs}$ yields a non-zero result. Therefore from terms proportional to $n_0^2(n_0-1)$ we obtain the equation:

$$\Big(i\partial_t - 2J(\cos p + \cos q - \cos r - \cos s)\Big)g^{pq}_{rs} = -iUn_0^2(n_0-1)\delta_{p+q-r-s}\sum_\delta J_\delta(t)^2 \times \tag{E.6}$$
$$\Big(i^{2\delta}e^{it(\cos r+\cos s)}e^{-i\delta(q+p)} - i^{-2\delta}e^{-it(\cos p+\cos q)}e^{i\delta(r+s)}\Big)$$

A similar calculation for the term proportional to $n_0(n_0-1)(n_0-2)$ yields:

$$\Big(i\partial_t - 2J(\cos p + \cos q - \cos r - \cos s)\Big)g^{pq}_{rs} = -iUn_0(n_0-1)(n_0-2)\delta_{p+q-r-s}\sum_\delta J_\delta(-t)^3 \times \tag{E.7}$$
$$\Big(i^\delta(e^{-i\delta p}e^{-it(\cos q-\cos r-\cos s)}e^{-i\delta q}e^{-it(\cos p-\cos r-\cos s)}) -$$
$$i^{-\delta}(e^{i\delta r}e^{-it(\cos p+\cos q-\cos s)} + e^{-i\delta s}e^{-it(\cos p+\cos q-\cos r)})$$

These equations can be solved by first making a transformation to rotating coordinates to eliminate the $2J$ term on the left, integrating the resulting equation and then transforming back. Adding Eq. E.6 and E.7 and performing this operation yields Eq. 5.6.

APPENDIX F

DYNAMICS OF MOMENTUM DISTRIBUTION TO $O(U/J)^2$

The dynamics of the momentum distribution to second order in U/J is now given by plugging in the expression for the two-body correlation function g_{rs}^{pq} into the equation:

$$n_q(\mathrm{t}) - n_q(0) = U \int_0^{\mathrm{t}} dt \int \frac{dp\ dr\ ds}{(2\pi)^3} \left(g_{rs}^{pq} - g_{pq}^{rs}\right) \tag{F.1}$$

One can readily check that the non-interacting expression for g_{rs}^{pq} yields Eq. 5.7.

Substituting Eq. E.6, which represents two-particle scattering into the first term on the right hand side of Eq. F.1 one obtains

$$\int dpdrds\delta_{p+s-r-q} g_{rq}^{ps} = \sum_{k,\delta} \int_0^t d\tau J_\delta^2(\tau) \Big[i^k J_{k-\delta}^2(\tau - t) J_{-k}(t) e^{-i(kq - t\cos q)} - i^{k-\delta} J_k^2(-t) J_{\delta-k}(t-\tau) e^{-i((k-\delta)q + (\tau - t)\cos q)} \Big] \tag{F.2}$$

Similarly, the second term in the RHS of Eq. F.1 produces

$$\int dpdrds\delta_{p+q-r-s} g_{rs}^{pq} = \sum_{k,\delta} \int_0^t d\tau J_\delta^2(\tau) \Big[i^{-k+\delta} J_{k-\delta}(\tau - t) J_{-k}^2(t) e^{i((k-\delta)q + (\tau - t)\cos q)} - i^{-k} J_k(-t) J_{\delta-k}^2(t-\tau) e^{i(kq - t\cos q)} \Big] \tag{F.3}$$

One can readily verify that the RHS of Eq. F.3 is the negative of the complex conjugate of the RHS of Eq. F.2. Hence the final expression is obtained by taking twice the real part of Eq.F.2.

A similar analysis for Eq.E.7, which arises from three-particle scattering yields for $\int dpdrds\delta_{p+s-r-q}g^{ps}_{rq}$:

$$\int dpdrds\delta_{p+s-r-q}g^{ps}_{rq} = \sum_{k,\delta}\int_0^t d\tau J^3_\delta(-\tau)\Big[i^k J_{k-\delta}(\tau-t)J^2_{-k}(t)e^{-i(kq-t\cos q)} - i^{k-\delta}J^3_k(-t)e^{-i((k-\delta)q+(\tau-t)\cos q)}\Big] \tag{F.4}$$

and for $\int dpdrds\delta_{p+q-r-s}g^{pq}_{rs}$:

$$\int dpdrds\delta_{p+q-r-s}g^{pq}_{rs} = \sum_{k,\delta}\int_0^t d\tau J^3_\delta(-\tau)\Big[-i^{-k}J_{k-\delta}(\tau-t)J^2_{-k}(t)e^{i(kq-t\cos q)} - i^{-k+\delta}J^3_k(-t)e^{i((k-\delta)q+(\tau-t)\cos q)}\Big] \tag{F.5}$$

Once again, the RHS of F.5 is the negative of the complex conjugate of the RHS of F.4

Combining Eqs F.2, F.3, F.4 and F.5 with the appropriate signs, yields after some manipulation, the final expression in Eq. 5.8.

Note that the terms Eqs. F.4, F.5, corresponding to three-particle scattering involve an additional factor of J_k, and are suppressed in magnitude compared to the terms in Eqs. F.2, F.3.

Considered separately these terms have very distinct effects. In Fig. F.1 I plot the time evolution of the momentum distribution assuming only the second order terms. Note first that both the second order terms yield a momentum distribution that is *symmetric* about $q = \pi/2$, as opposed to the first order term, shown in Fig. 5.4. Moreover, while the term representing two-particle scattering tends to *enhance* the peak-like feature at finite momentum, the term representing three-particle scattering tends to *enhance* the occupation at finite momentum.

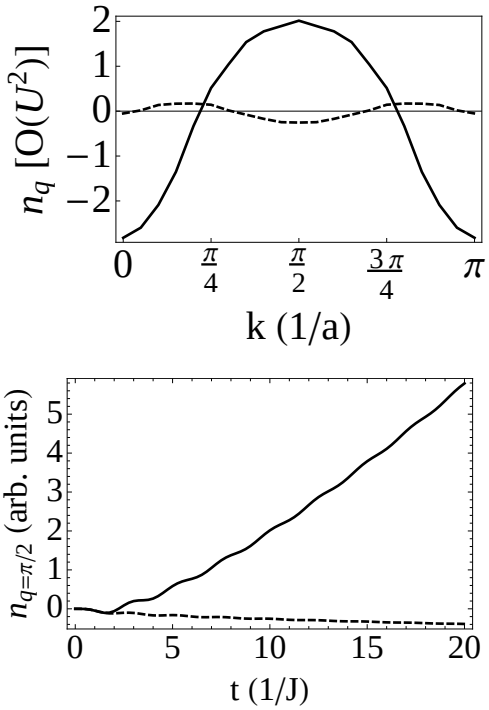

Figure F.1: **Role of Quadratic corrections in the evolution of n_q** Top: Solid line is the contribution to n_q arising only from terms in Eqs. F.2 and F.3, showing an enhancement in the peaks at $\pi/2$. A smaller contribution comes from terms in Eq. F.4 and Eq.F.5 shown by the dashed line. This term favors a suppression of occupation at $\pi/2$. Bottom: The momentum distribution at $\pi/2$ as a function of time, where the solid and dashed curves represent contributions from same terms as in the Top figure